

Cover Page



Universiteit Leiden



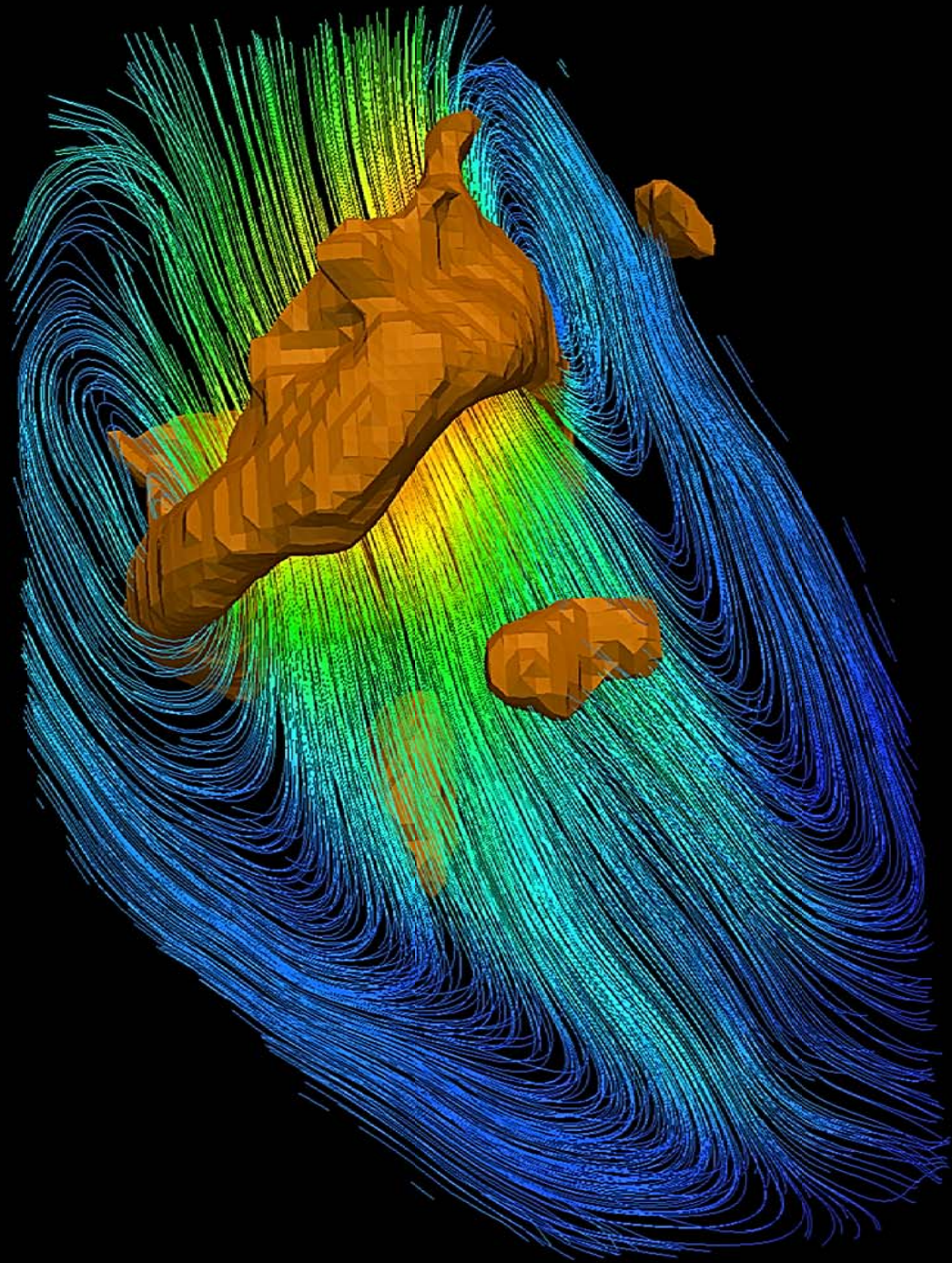
The handle <http://hdl.handle.net/1887/42781> holds various files of this Leiden University dissertation.

Author: Elbaz M.S.M.M.

Title: Three-dimensional in-vivo intra-cardiac vortex flow from 4D Flow MRI : quantification, automatic identification and association with energy loss

Issue Date: 2016-09-06

Three-dimensional in-vivo intra-cardiac
vortex flow from 4D Flow MRI
Quantification, automatic identification and
association with energy loss



Mohammed S.M. Elbaz

Three-dimensional in-vivo intra-cardiac vortex flow from 4D Flow MRI

Quantification, automatic identification and association
with energy loss

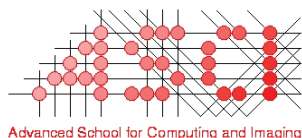
Mohammed S.M. Elbaz

Colophon

About the cover:

For the printed copy of this thesis, move the thesis vertically around the horizontal axis to see the animation. The animated printed cover shows the time evolution of 3D vortex ring (in brown) within left ventricular blood flow of a healthy human heart during early diastolic filling (from the moment of peak inflow to end diastasis) as derived from in-vivo 4D flow MRI velocity field. The structures in brown are 3D vortex cores (based on Λ^2 definition) superimposed on a streamline visualization of a cross-sectional view of LV blood flow color coded from blue to red according to velocity magnitude. Time (t), placed at the bottom of the cover, is the relative time of each phase/frame presented as a fraction of the RR interval starting from the time of peak inflow ($0.43RR$) to the time of the end of diastasis ($0.73RR$). More details can be found in Chapter 2 and online movie 2 referred therein.

Online cover shows the 3D vortex ring core superimposed on streamlines in the left ventricle at the moment of peak early filling. Copyright Mohammed S.M. Elbaz.



This work was carried out in the ASCI graduate school.
ASCI dissertation series number 356

This research is supported by the Dutch Technology Foundation STW, which is part of the Netherlands Organisation for Scientific Research (NWO) and partly funded by the Ministry of Economic Affairs (project number 11626).

Three-dimensional in-vivo intra-cardiac vortex flow from 4D Flow MRI: Quantification, automatic identification and association with energy loss
Ph.D. thesis with a summary in Dutch.

ISBN 978-94-6332-052-8

Thesis layout by Mohammed S.M. Elbaz

Cover designed by Mohammed S. M. Elbaz and Rahil Shahzad

Printed by GVO Drukkers en Vormgevers BV

© 2016 Mohammed S.M. Elbaz, Leiden, the Netherlands

All rights reserved. No part of this publication may be reproduced or transmitted in any form or by any means, electronic or mechanical, including photocopying, recording, or any information storage and retrieval system, without permission in writing from the copyright owner.

Three-dimensional in-vivo intra-cardiac vortex flow from 4D Flow MRI

Quantification, automatic identification and association
with energy loss

Proefschrift

ter verkrijging van

de graad van Doctor aan de Universiteit Leiden,

op gezag van Rector Magnificus Prof. mr. C. J. J. M. Stolker,

volgens besluit van het College voor Promoties

te verdedigen op dinsdag 6 september 2016

klokke 16:15 uur

door

Mohammed Samir Mohammed Mohammed Elbaz

geboren te Dakahliya (Egypte) in 1985

Promotiecommissie

promotor: Prof.dr.ir. B.P.F. Lelieveldt

co-promotor: Dr.ir. R.J. van der Geest

leden promotie commissie: Prof.dr.ir. T. Ebbers
Linköping University, Linköping (Sweden)

Prof.dr. H.J. Lamb

Dr.ir. J. Wentzel
Erasmus Medical Center, Rotterdam

To my parents Hoda and Samir, and my wife Simin

Contents

Chapter 1	Introduction	9
Chapter 2	Vortex flow during early and late left ventricular filling in normal subjects: quantitative characterization using retrospectively-gated 4D flow cardiovascular magnetic resonance and three-dimensional vortex core analysis	21
Chapter 3	Altered left ventricular vortex ring formation by 4-dimensional flow magnetic resonance imaging after repair of atrioventricular septal defects	43
Chapter 4	Assessment of viscous energy loss and the association with 3D vortex ring formation in left ventricular inflow: in vivo evaluation using 4D Flow MRI	63
Chapter 5	Abnormal left atrial flow patterns in patients after atrioventricular septal defect correction and regurgitation: evaluation with 4D Flow Magnetic Resonance Imaging and particle tracing	91
Chapter 6	Automatic extraction of the 3D left ventricular diastolic transmitral vortex ring from 3D whole-heart phase contrast MRI using Laplace-Beltrami signatures	107
Chapter 7	Hierarchical Shape Distributions for Automatic Identification of 3D Diastolic Vortex Rings from 4D Flow MRI	119
Chapter 8	Summary, Discussion and Future Perspectives	131
	Samenvatting en conclusies	139
	List of publications	
	Acknowledgements	
	Curriculum vitae	

Chapter 1

Introduction

1.1. Cardiac Physiology: Background

The heart is a vital organ in the human body that is responsible for pumping blood into the circulatory system through a network of blood vessels. The human heart is decomposed of four chambers (Figure 1.1): left and right atria as well as left and right ventricles. Atria are the upper chambers of the heart and work as reservoir for blood incoming from veins to pass it into the ventricles. Ventricles are the two lower chambers of the heart that are responsible for pumping (ejecting) the blood, incoming from the atria, out of the heart to the body. The left atrium and ventricle are commonly referred to as the left heart whereas right atrium and ventricle are referred to as the right heart. The right heart helps oxygenating the blood: the de-oxygenated blood flows through the right atrium into the right ventricle that pumps blood to the lungs where it gets oxygenated. The left heart pumps this oxygenated blood into the rest of the body: oxygenated blood coming from the lungs flows through the left atrium into the left ventricle (LV) that pumps it to the rest of the body through the aorta.

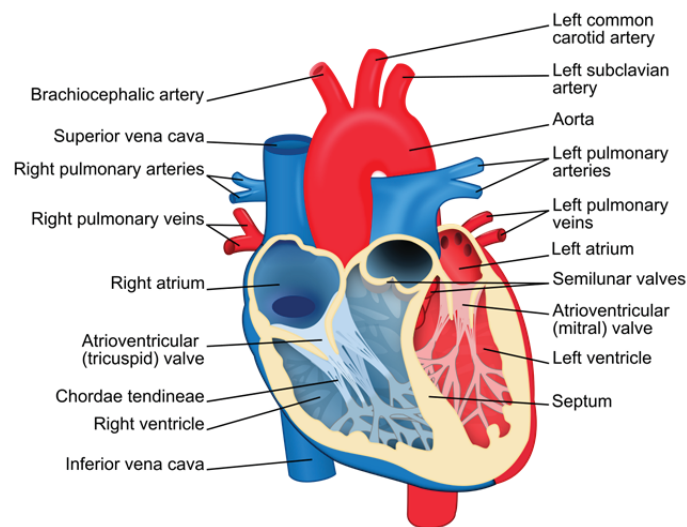


Figure 1.1. Anatomy of the heart (source: <https://commons.wikimedia.org>)

A single cardiac cycle (heart beat) consists of two phases: systole and diastole. The systole, or contraction phase, is the part of the cardiac cycle when left and right ventricles contract to eject blood into the aorta and pulmonary artery, respectively. Unidirectional flow out of the ventricles is ensured by the atrioventricular (mitral and tricuspid) valves that close during systole to prevent backflow into the atria. Diastole is the

part of the cardiac cycle when the ventricles relax and refill with blood following the systole. Diastolic filling consists of two main phases: early filling and late (atrial) filling. Early diastolic filling (E-wave), also known as passive filling, is the phase when the ventricle relaxes and its pressure drops below the pressure in the atrium. As a result, the atrioventricular valves open causing the accumulated blood in the atria to flow into the ventricle in a passive manner. Late diastolic filling (A-wave), also known as atrial or active filling, is the phase when the atria contract and push the atrial blood into the ventricle. The duration from the end of E-wave to the start of A-wave is called diastasis and it is inversely proportional to the heart rate. In normal hearts, the passive early diastolic filling accounts for 70-80% of the total ventricular inflow therefore, minimizing the needed atrial contraction (work).

1.2. Cardiac Vortex ring formation: Historical perspective

A vortex can be defined, intuitively, as the swirling motion of a group of particles around a common axis. In more formal terms, a vortex is considered a flow region with a concentrated vorticity. In three-dimensional space, vorticity is a vector quantity that quantifies the local rotation rate of flow particles along the three principal components of the flow field. Vorticity is a fundamental property of the flow and, in case of incompressible flow, allows a complete reconstruction of the velocity field [1]. In mathematical terms, vorticity is defined as the curl of velocity.

Vortex structures in the flow motion are abundant in nature, ranging from destructing vortices of hurricanes and volcano eruptions to smoke rings and vortices in the wake of a jelly fish swimming motion. Interestingly, vortex flow does not only form in our surrounding environment, but also inside the heart and in every single heartbeat. In the cardiac left ventricle, both in-vitro and in-vivo studies have shown that during diastolic filling, a vortex ring (also known as a toroidal vortex) is naturally formed from the shear layer distal to the mitral valve (MV) [2-6]. In a two-dimensional (2D) cross sectional view, a vortex ring is visualized as a pair of counter rotating vortices (Figure 1.2).

Vortex ring formation in the left ventricle was initially reported from in-vitro experiments using LV models [2, 4], suggesting it as a mechanism to help the full closure of the bicuspid mitral valve. However, given that the in-vivo study of vortex flow requires a flow imaging modality, it was not until the rise of color Doppler velocity mapping when Kim et al. have confirmed the vortex formation in-vivo in a pig's heart using 2D color Doppler recordings [5]. Kim et al. was the first to in-vivo show the presence of vortex flow

in the normal human left ventricle using 3D magnetic resonance (MR) velocity mapping and 2D streamline flow visualization [6]. Kilner et al. have further confirmed the presence of recirculating flow in the LV distal to the MV leaflets from MR velocity mapping. They suggested a role of LV vortex flow formation in efficient redirection of blood inflow towards the aortic outflow tract in an energy efficient manner [3].

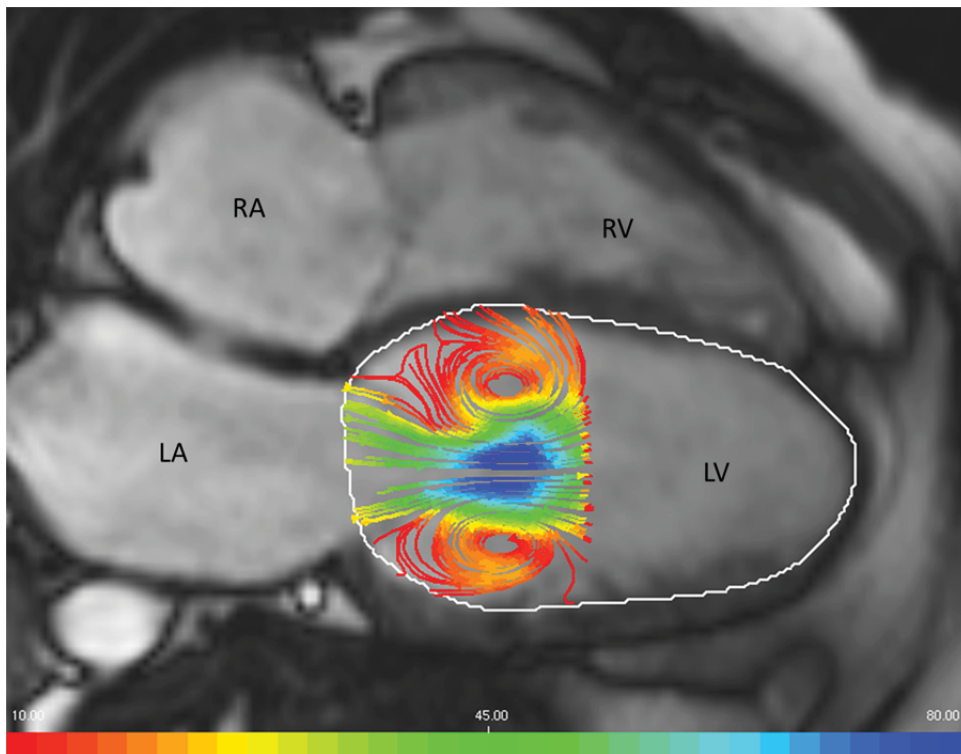


Figure 1.2. 2D view of an early filling vortex ring flow in the left ventricle (LV) visualized as a pair of counter rotating vortices (left) using streamlines (color coded by velocity magnitude from red to blue) and superimposed on a four chamber MR cardiac view. LV endocardial boundary is delineated in white contours. (RV: Right Ventricle, LA: Left Atrium and RA: Right Atrium).

Moving from investigational studies to more quantitative cardiac vortex flow analysis, Gharib et al. have introduced the vortex formation time (VFT) as a global quantitative and dimensionless index that describes the optimal vortex ring formation and progression during early diastolic LV filling [7]. VFT is essentially the length-to-diameter ratio of an ejected fluid column ($VFT=L/D$) with length L through an orifice with diameter

D [8]. In the LV, VFT can be computed as $(VFT = \overline{U(t)}.dt/\overline{D})$ with $\overline{U(t)}$ as time-averaged speed through the opened MV over the early filling period dt and through the average MV inflow diameter \overline{D} . From in-vitro experiments, optimal VFT is found to consistently take place at a specific VFT of ≈ 4 . Optimal VFT in the early LV filling phase of normal human volunteers was found to be consistent with in-vitro experiments (normal VFT range = 3.3-5.5). A significantly different VFT from the optimal range was reported in patients with dilated cardiomyopathy [7], stenotic mitral valves [9, 10], heart failure, elevated LV afterload [11] and even in Alzheimer's disease patients [12]. Therefore VFT has been suggested as a novel index for diastolic dysfunction and cardiac health [7, 13]. Nevertheless, recent studies [14] have reported that VFT happens in the healthy LV much earlier in diastole (VFT \approx 1.6) compared to previously reported optimal VFT (VFT \approx 4) [7], therefore questioning previously suggested relation between VFT and diastolic function and concluded that VFT might not be related to diastolic function [15].

1.3. Progress in vortex flow analysis

In recent years new advancements in in-vivo flow imaging techniques, such as echo Particle Image Velocimetry (echo-PIV) [16, 17] and phase contrast Magnetic Resonance Imaging (PC-MRI) [18, 19] have enabled more in-depth analysis of LV vortex flow. For instance, echo-PIV was used to reconstruct 2D velocity and vorticity fields to quantitatively characterize 2D LV vortex flow in normal subjects and patients with systolic dysfunction [20], prosthetic mitral valve heart failure [21] and patients with apical thrombus formation [22]. Nevertheless, Echo-PIV requires injection of contrast particles (contrast agent) which are then tracked using so-called particle image velocimetry (PIV) to approximate the velocity field. While promising, Echo-PIV is mainly limited to assessment of 2D velocity field and consequently is a 2D analysis.

Recent developments are not limited to flow imaging techniques. Major progress in computational fluid mechanics (CFD) modeling methods has also been made. This has been driven by the significant growth of available computer processing power and the use of in-vivo-derived boundary conditions. Such progress enabled simulation and analysis of cardiac vortex flow in unprecedented detail. Specifically, 3D modeling of LV flow dynamics has revealed the complex 3D nature of the LV flow field [23-25]. Detailed 3D simulations guided by in-vivo MR boundary conditions of diastolic LV vortical flow, revealed the complex dynamics of cardiac vortex ring formation including vortex twisting,

impingement on the wall and following breakup [26, 27]. These studies emphasize the three-dimensional nature of LV vortex ring flow, indicating that proper in-vivo analysis of intra-cardiac vortex flow needs to be three-dimensional and involving the three components of the velocity field.

While CFD simulations provide high spatial and temporal resolution allowing detailed physical analysis, it involves numerous simplifications to the cardiac geometry and dynamics. This can result in a different vortex ring flow dynamics from true human cardiac flow. Hence, in-vivo analysis of 3D intra-cardiac vortex ring flow is important to understand its dynamics, mechanism and physiological properties in the human cardiac (dys)function.

1.4. Four-dimensional Flow Magnetic Resonance Imaging (4D Flow MRI)

4D Flow MRI (also known as three-directional three-dimensional phase contrast MRI) is an emerging in-vivo flow imaging technique that enables the acquisition of all three components of the flow field, over the three spatial dimensions and over the cardiac cycle [18, 19, 28-31]. As opposed to other techniques, e.g. echo-PIV, 4D Flow MRI does not require the use of a contrast agent for flow imaging. Instead, 4D Flow MRI uses the intrinsic magnetic properties of blood flow. That is, the property of the flow velocity being directly related to the phase shift in the MR signal along a magnetic field [19, 31]. The velocity along a specified encoding direction can be detected by applying suitable bipolar gradients, where two acquisitions are performed that are identical in all parameters but with two different velocity-dependent signal phases [18, 19, 29]. The velocity images can then be calculated by subtracting the two resulting phase images. This approach is also known as phase contrast MRI (PC-MRI).

A dynamic flow acquisition over a cardiac cycle involves acquiring the data over multiple ECG-gated cardiac cycles to tackle the slow (up to 20 minutes) MR acquisition relative to the cardiac dynamics. Acquiring velocity encoded data requires to manually predefine the velocity sensitivity encoding parameter (VENC). That is the maximum positive or negative velocity that can be detected without an aliasing error. VENC is mainly defined empirically and based on prior knowledge of the maximum expected velocity in the region of interest. 4D Flow MRI acquires dynamic volumetric velocity data over three velocity encoding directions, requiring long scan times (up to 20 minutes) that can hamper

its clinical use. Therefore, different acceleration techniques have been developed to speed up the scan time [28, 32-34].

The typical output of a reconstructed 4D Flow MRI acquisition is three-dimensional image volumes that encode the three velocity field components (i.e. the two in-plane \mathbf{U} , \mathbf{V} components and the through-plane \mathbf{W} component) (Figure 1.3). The fact that 4D Flow MRI provides the complete velocity field, enables in vivo analysis of LV kinetic energy [35, 36], turbulent flow [37, 38], relative pressure field [39-41] evaluation of different flow components [42] and flow patterns [43] in three-dimensional space as well as their evolution over time.

Töger et al. have used Lagrangian coherent structure (LCS) analysis [44, 45] of 4D Flow MRI to quantify the vortex ring volume in LV diastolic function in healthy human subjects and in patients with dilated cardiomyopathy [46]. While encouraging, LCS provides global vortex flow analysis over a period of time without providing direct information about the instantaneous vortex development. To characterize the details of diastolic vortex ring flow dynamics in the LV and in relation to inflow, 3D instantaneous-based analysis of vortex ring flow evolution over the diastolic LV filling is needed.

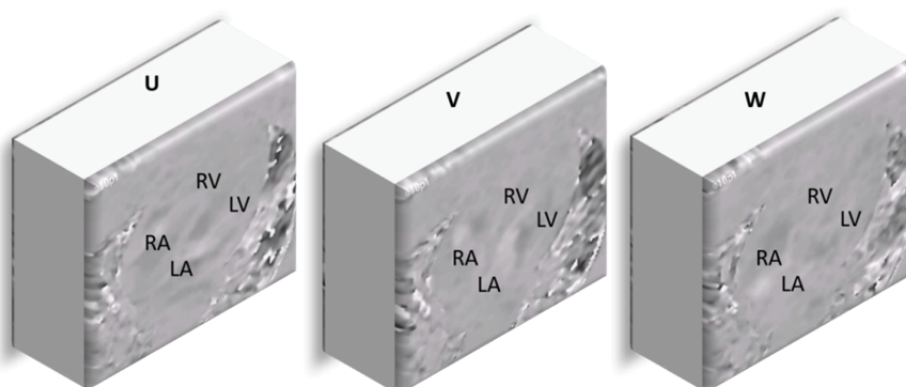


Figure 1.3. Example of reconstructed whole-heart 4D Flow MRI volumes of the three velocity components (the in-plane \mathbf{U} , \mathbf{V} components and the through-plane \mathbf{W} component). Grey-scale values encode the velocity magnitude and direction along the direction of interest.

1.5. Thesis objectives and outline

The aim of this thesis is to develop methods that enable in-vivo analysis of 3D vortex flow patterns in the human heart, particularly through analysis of the 3D velocity field from in-vivo 4D Flow MRI. Accordingly, this thesis has the following four objectives:

1. To characterize and quantify in-vivo 3D cardiac vortex flow to reveal the normal 3D vortex flow formation process in healthy human subjects.
2. To determine the impact of unnatural cardiac morphology in human patients, on 3D cardiac vortex flow formation.
3. To assess consequences of altered 3D cardiac vortex flow on cardiac physiology.
4. To enable objective analysis of in-vivo 3D cardiac vortex flow from 4D Flow MRI.

These objectives are addressed throughout the remaining chapters of this thesis as follows:

Chapter 2 introduces an interactive workflow for instantaneous 3D vortex ring identification in the LV during early and late diastolic filling from in-vivo 4D Flow MRI. Standardized quantitative geometric characterization of 3D diastolic vortex ring flow is proposed providing normal ranges in a cohort of healthy subjects. The association of 3D vortex ring shape with MV inflow shape through mitral annulus and leaflet tips are evaluated.

Chapter 3 investigates the effect of abnormal atrioventricular (mitral) valvular inflow on 3D vortex ring formation in a cohort of congenital heart disease patients who are known to develop abnormal atrioventricular (mitral) valvular inflow and morphology. These are patients who underwent an atrioventricular surgical repair due to a congenital septal defect. Quantitative characterization of 3D vortex ring shape, geometry and position relative to LV, introduced in **chapter 2**, are evaluated and compared to those of healthy subjects. Altered 3D vortex formation in the studied patients is revealed.

Chapter 4 evaluates the consequences of altered vortex ring flow formation on LV physiology through assessment of the association between in-vivo, 4D Flow MRI-derived, viscous energy loss during diastole and inflow 3D vortex ring formation during both early and late filling in both healthy subjects and patients.

Chapter 5 explores 3D systolic left atrial vortex flow in healthy subjects and congenital heart disease patients with various degrees of left atrioventricular valve (LAVV) regurgitation.

Chapter 6 and Chapter 7 address the critical need in clinical practice to ensure objective quantitative results by proposing two novel methods, based on 3D shape signatures, for automatic identification and extraction of 3D vortex ring objects (isosurfaces). The proposed methods are evaluated in healthy subjects (**Chapter 6 and Chapter 7**) and patients (**Chapter 7**) showing quite promising and encouraging results.

Chapter 8 summarizes the results of this thesis, and discusses future perspectives.

1.6. References

1. Kheradvar, A. and G. Pedrizzetti, Vortex formation in the cardiovascular system. 2012, Springer. p. 45-79.
2. Bellhouse, B., Fluid mechanics of a model mitral valve and left ventricle. *Cardiovascular research*, 1972. 6(2): p. 199-210.
3. Kilner, P.J., et al., Asymmetric redirection of flow through the heart. *Nature*, 2000. 404(6779): p. 759-761.
4. Reul, H., N. Talukder, and E. Mu, Fluid mechanics of the natural mitral valve. *Journal of biomechanics*, 1981. 14(5): p. 361-372.
5. Kim, W.Y., et al., Two-dimensional mitral flow velocity profiles in pig models using epicardial Doppler echocardiography. *Journal of the American College of Cardiology*, 1994. 24(2): p. 532-545.
6. Kim, W.Y., et al., Left ventricular blood flow patterns in normal subjects: a quantitative analysis by three-dimensional magnetic resonance velocity mapping. *Journal of the American College of Cardiology*, 1995. 26(1): p. 224-238.
7. Gharib, M., et al., Optimal vortex formation as an index of cardiac health. *Proceedings of the National Academy of Sciences*, 2006. 103(16): p. 6305-6308.
8. Gharib, M., E. Rambod, and K. Shariff, A universal time scale for vortex ring formation. *Journal of Fluid Mechanics*, 1998. 360: p. 121-140.
9. Kheradvar, A. and M. Gharib, Influence of ventricular pressure drop on mitral annulus dynamics through the process of vortex ring formation. *Annals of biomedical engineering*, 2007. 35(12): p. 2050-2064.
10. Kheradvar, A., M. Milano, and M. Gharib, Correlation between vortex ring formation and mitral annulus dynamics during ventricular rapid filling. *ASAIO Journal*, 2007. 53(1): p. 8-16.
11. Jiamsripong, P., et al., Impact of Acute Moderate Elevation in Left Ventricular Afterload on Diastolic Transmitral Flow Efficiency: Analysis by Vortex Formation Time. *Journal of the American Society of Echocardiography*, 2009. 22(4): p. 427-431.
12. Belohlavek, M., et al., Patients With Alzheimer Disease Have Altered Transmitral Flow Echocardiographic Analysis of the Vortex Formation Time. *Journal of Ultrasound in Medicine*, 2009. 28(11): p. 1493-1500.
13. Kheradvar, A., et al., Assessment of transmitral vortex formation in patients with diastolic dysfunction. *Journal of the American Society of Echocardiography*, 2012. 25(2): p. 220-227.
14. Stewart, K.C., et al., Left ventricular vortex formation is unaffected by diastolic impairment. *American Journal of Physiology-Heart and Circulatory Physiology*, 2012. 303(10): p. H1255-H1262.
15. Pasipoularides, A., P.P. Vlachos, and W.C. Little, Vortex formation time is not an index of ventricular function. *Journal of cardiovascular translational research*, 2015. 8(1): p. 54-58.
16. Kim, H., J. Hertzberg, and R. Shandas, Development and validation of echo PIV. *Experiments in fluids*, 2004. 36(3): p. 455-462.
17. Adrian, R.J. and J. Westerweel, Particle image velocimetry. 2011: Cambridge University Press.

18. Pelc, N.J., et al., Phase contrast cine magnetic resonance imaging. *Magnetic resonance quarterly*, 1991. 7(4): p. 229-254.
19. Markl, M., et al., 4D flow MRI. *Journal of Magnetic Resonance Imaging*, 2012. 36(5): p. 1015-1036.
20. Hong, G.R., et al., Characterization and Quantification of Vortex Flow in the Human Left Ventricle by Contrast Echocardiography Using Vector Particle Image Velocimetry. *Jacc-Cardiovascular Imaging*, 2008. 1(6): p. 705-717.
21. Abe, H., et al., Contrast echocardiography for assessing left ventricular vortex strength in heart failure: a prospective cohort study. *European Heart Journal-Cardiovascular Imaging*, 2013. 14(11): p. 1049-1060.
22. Son, J.-W., et al., Abnormal left ventricular vortex flow patterns in association with left ventricular apical thrombus formation in patients with anterior myocardial infarction. *Circulation Journal*, 2012. 76(11): p. 2640-2646.
23. Domenichini, F., G. Pedrizzetti, and B. Baccani, Three-dimensional filling flow into a model left ventricle. *Journal of fluid mechanics*, 2005. 539: p. 179-198.
24. Cheng, Y., H. Oertel, and T. Schenkel, Fluid-structure coupled CFD simulation of the left ventricular flow during filling phase. *Annals of biomedical engineering*, 2005. 33(5): p. 567-576.
25. Nordsletten, D., et al., Fluid–solid coupling for the investigation of diastolic and systolic human left ventricular function. *International Journal for Numerical Methods in Biomedical Engineering*, 2011. 27(7): p. 1017-1039.
26. Le, T.B. and F. Sotiropoulos, On the three-dimensional vortical structure of early diastolic flow in a patient-specific left ventricle. *European Journal of Mechanics-B/Fluids*, 2012. 35: p. 20-24.
27. Schenkel, T., et al., MRI-based CFD analysis of flow in a human left ventricle: methodology and application to a healthy heart. *Annals of biomedical engineering*, 2009. 37(3): p. 503-515.
28. Dumoulin, C., et al., Three-dimensional phase contrast angiography. *Magnetic Resonance in Medicine*, 1989. 9(1): p. 139-149.
29. Bernstein, M.A., A. Shimakawa, and N.J. Pelc, Minimizing TE in moment-nulled or flow-encoded two-and three-dimensional gradient-echo imaging. *Journal of Magnetic Resonance Imaging*, 1992. 2(5): p. 583-588.
30. Gu, T., et al., PC VIPR: a high-speed 3D phase-contrast method for flow quantification and high-resolution angiography. *American journal of neuroradiology*, 2005. 26(4): p. 743-749.
31. Ebbers, T., Flow imaging: cardiac applications of 3D cine phase-contrast MRI. *Current Cardiovascular Imaging Reports*, 2011. 4(2): p. 127-133.
32. Wigström, L., L. Sjöqvist, and B. Wranne, Temporally resolved 3D phase-contrast imaging. *Magnetic resonance in medicine*, 1996. 36(5): p. 800-803.
33. Markl, M., et al., Time-resolved 3D MR velocity mapping at 3T: Improved navigator-gated assessment of vascular anatomy and blood flow. *Journal of magnetic resonance imaging*, 2007. 25(4): p. 824-831.
34. Johnson, K.M. and M. Markl, Improved SNR in phase contrast velocimetry with five-point balanced flow encoding. *Magnetic Resonance in Medicine*, 2010. 63(2): p. 349-355.
35. Carlsson, M., et al., Quantification of left and right ventricular kinetic energy using four-dimensional intracardiac magnetic resonance imaging flow measurements. *American Journal of Physiology-Heart and Circulatory Physiology*, 2012. 302(4): p. H893-H900.
36. Eriksson, J., et al., Quantification of presystolic blood flow organization and energetics in the human left ventricle. *American Journal of Physiology-Heart and Circulatory Physiology*, 2011. 300(6): p. H2135-H2141.
37. Dyverfeldt, P., et al., Assessment of fluctuating velocities in disturbed cardiovascular blood flow: in vivo feasibility of generalized phase-contrast MRI. *Journal of Magnetic Resonance Imaging*, 2008. 28(3): p. 655-663.
38. Dyverfeldt, P., et al., Quantification of intravoxel velocity standard deviation and turbulence intensity by generalizing phase-contrast MRI. *Magnetic resonance in medicine*, 2006. 56(4): p. 850-858.

39. Ebbers, T., et al., Noninvasive measurement of time-varying three-dimensional relative pressure fields within the human heart. *Journal of biomechanical engineering*, 2002. 124(3): p. 288-293.
40. Ebbers, T., et al., Estimation of relative cardiovascular pressures using time-resolved three-dimensional phase contrast MRI. *Magnetic resonance in medicine*, 2001. 45(5): p. 872-879.
41. Ebbers, T. and G. Farnebäck, Improving computation of cardiovascular relative pressure fields from velocity MRI. *Journal of Magnetic Resonance Imaging*, 2009. 30(1): p. 54-61.
42. Eriksson, J., et al., Semi-automatic quantification of 4D left ventricular blood flow. *J Cardiovasc Magn Reson*, 2010. 12(9): p. 12.
43. Markl, M., P.J. Kilner, and T. Ebbers, Comprehensive 4D velocity mapping of the heart and great vessels by cardiovascular magnetic resonance. *J Cardiovasc Magn Reson*, 2011. 13(7): p. 10.1186.
44. Haller, G. and G. Yuan, Lagrangian coherent structures and mixing in two-dimensional turbulence. *Physica D: Nonlinear Phenomena*, 2000. 147(3): p. 352-370.
45. Shadden, S.C., F. Lekien, and J.E. Marsden, Definition and properties of Lagrangian coherent structures from finite-time Lyapunov exponents in two-dimensional aperiodic flows. *Physica D: Nonlinear Phenomena*, 2005. 212(3): p. 271-304.
46. Töger, J., et al., Vortex ring formation in the left ventricle of the heart: analysis by 4D flow MRI and Lagrangian coherent structures. *Annals of biomedical engineering*, 2012. 40(12): p. 2652-2662.

Chapter 2

Vortex flow during early and late left ventricular filling in normal subjects: quantitative characterization using retrospectively-gated 4D flow cardiovascular magnetic resonance and three-dimensional vortex core analysis

This chapter was adapted from:

Elbaz, M. S.*, Calkoen, E. E.*, Westenbergh, J. J., Lelieveldt, B. P., Roest, A. A., & van der Geest, R. J. (2014). **Vortex flow during early and late left ventricular filling in normal subjects: quantitative characterization using retrospectively-gated 4D flow cardiovascular magnetic resonance and three-dimensional vortex core analysis.** *Journal of Cardiovascular Magnetic Resonance*, 16(1), 78.

* Elbaz, M. S. and Calkoen, E. E. contributed equally to this work.

Abstract

Background: LV diastolic vortex formation has been suggested to critically contribute to efficient blood pumping function, while altered vortex formation has been associated with LV pathologies. Therefore, quantitative characterization of vortex flow might provide a novel, objective tool for evaluating LV function. The objectives of this study were 1) to assess feasibility of vortex flow analysis during both early and late diastolic filling *in vivo* in normal subjects using 4D Flow cardiovascular magnetic resonance (CMR) with retrospective cardiac gating and 3D vortex core analysis 2) establish normal quantitative parameters characterizing 3D LV vortex flow during both early and late ventricular filling in normal subjects.

Methods: With full ethical approval, twenty-four healthy volunteers (mean age: 20 ± 10 years) underwent whole-heart 4D Flow CMR. The Lambda2-method was used to extract 3D LV vortex ring cores from the blood flow velocity field during early (E) and late (A) diastolic filling. The 3D location of the center of vortex ring core was characterized using cylindrical cardiac coordinates (Circumferential, Longitudinal (L), Radial(R)). Comparison between E and A filling was done with a paired T-test. The orientation of the vortex ring core was measured and the ring shape was quantified by the circularity index (CI). Finally, the Spearman's correlation between the shapes of mitral inflow pattern and formed vortex ring cores was tested.

Results: Distinct E- and A-vortex ring cores were observed with centers of A-vortex rings significantly closer to the mitral valve annulus (E-vortex $L=0.19 \pm 0.04$ versus A-vortex $L=0.15 \pm 0.05$; $p=0.0001$), closer to the ventricle's long-axis (E-vortex: $R=0.27 \pm 0.07$, A-vortex: $R=0.20 \pm 0.09$, $p=0.048$) and more elliptical in shape (E-vortex: $CI=0.79 \pm 0.09$, A-vortex: $CI=0.57 \pm 0.06$; $p<0.001$) compared to E-vortex. The circumferential location and orientation relative to LV long-axis for both E- and A-vortex ring cores were similar. Good to strong correlation was found between vortex shape and mitral inflow shape through both the annulus ($r=0.66$) and leaflet tips ($r=0.83$).

Conclusions: Quantitative characterization and comparison of 3D vortex rings in LV inflow during both early and late diastolic phases is feasible in normal subjects using retrospectively-gated 4D Flow CMR, with distinct differences between early and late diastolic vortex rings.

2.1. Introduction

Vortex formation within the left ventricular (LV) blood flow has been suggested to critically contribute to efficient blood pumping function [1]. A vortex can be described as a group of fluid particles with a swirling motion around a common axis. Among different types of vortices, vortex rings (also known as toroidal vortex) are abundant in nature because of their compactness and stability [1-3].

In the LV, in healthy subjects, both *in vivo* and *in vitro* studies have reported vortex ring formation during early diastolic filling, originating at the distal tip of the mitral valve (MV) leaflets [1, 4-11]. In a three dimensional (3D) view, this vortex ring appears as a closed tube with torus-like shape distal to the mitral valve orifice. In a two dimensional (2D) four-chamber view a 3D vortex ring appears as a counter-rotating vortex pair, one distal to the anterior MV leaflet and another distal to the posterior leaflet. Such vortex formation may help in efficient MV closure [5], efficient diastolic filling, minimizing kinetic energy loss [4, 6] and preventing thrombus formation [7]. An altered (early filling) vortex formation have been shown to develop in patients with diastolic dysfunction and dilated ischemic cardiomyopathy, suggesting a relation between abnormal vortex formation and LV dysfunction [7, 8]. On the other hand, in normal subjects, discrepancies arise in literature and little is known about vortex formation during late filling. Experimental studies using computational fluid dynamics (CFD)-based simulations of LV inflow have reported the formation of a vortex ring distal to the MV during late LV filling, [12-17]. In contrast, *in vivo* studies have reported only the formation of a single anterior vortex during late filling (i.e. not a vortex ring because of the absence of a posterior vortex) [6, 9, 18-21] or even the absence of any vortex [18]. While CFD simulation can provide higher temporal and spatial resolution than *in vivo* data, application of CFD techniques also involve simplifications of the geometry and dynamics of the left ventricle and mitral valve leaflets which might result in inaccurate modelling of the true blood flow.

4D Flow CMR (also known as 4D Flow MRI) with retrospective cardiac gating can acquire all the three directional velocity components (in-plane and through-plane) of the blood flow relative to the three spatial dimensions and over the whole cardiac cycle, providing a powerful tool for evaluating blood flow patterns during both early and late left ventricular filling *in-vivo* [6, 22, 23]. Previous studies have shown the feasibility of using 4D Flow CMR for vortex flow analysis [6, 19, 22, 24-27]. These studies mainly focus on vortex formation during early filling inflow but not late filling inflow. While paramount for

establishing normal ranges defining LV vortex flow, standardized quantitative characterization of the 3D shape and location of normal vortex flow are currently lacking.

Different from visualization-based vortex identification, vortex core detection techniques [28-30] base their vortex identification on the underlying physical properties of a vortex instead of only visual assessment, therefore, provide more objective vortex definition. CFD experiments have shown that LV vortex ring originates from the inlet jet through the mitral valve orifice during early LV filling [1, 4, 10, 13], therefore, the shape of the formed vortex is expected to resemble the shape of the originating valvular opening [4, 13]. Hence, we hypothesized that similar behavior could be identified *in vivo* where a more oval opening of the MV during peak late filling results in a more elliptical vortex ring compared to the one originating from a more circular valve opening during peak early filling. Accordingly, the aims of our study were to apply retrospectively-gated 4D Flow CMR and quantitative 3D vortex core analysis to 1) Assess feasibility of *in vivo* vortex flow analysis during both early and late diastolic filling in normal subjects 2) Establish normative quantitative parameters characterizing 3D LV vortex flow during both early and late ventricular filling in normal subjects.

2.2. Methods

2.2.1. Study population

Twenty-four healthy volunteers (9 males, mean age 20 ± 10 years; age range 9-44 years), without history of cardiac disease, abnormalities on ECG or echocardiography were included. The study protocol was approved by the institutional review board and written informed consent was given by all subjects or their legal representatives.

2.2.2. 4D Flow CMR protocol

All subjects underwent 4D Flow MR imaging using a 3T digital broadband multi-transmit CMR system (Ingenia, Philips Medical Systems, Best, The Netherlands), with maximal gradient amplitude 45 mT/m and maximal slew rate 200 T/m/s. For signal reception, a 60cm Torso coil was used in combination with the FlexCoverage Posterior coil in the tabletop, combining a maximum of 32 elements. A 3D time-resolved volume acquisition of the whole heart was performed with velocity encoding in all three directions with velocity sensitivity (VENC) of 150 cm/s. The acquired volume data was reconstructed in time-resolved manner (30 cardiac phases per cardiac cycle) into $2.3\times 2.3\times 3-4.2\text{mm}^3$

(three subjects were scanned with 3 mm slice thickness). Retrospective cardiac gating was performed with Vector ECG triggering. Scan parameters: echo time 3.0 ms, repetition time 9.9 ms, flip angle 10°, field-of-view 400 mm, number of signal averages 1. VENC 150 cm/sec. Acceleration was achieved by Echo Planar Imaging with EPI factor 5. Free breathing was allowed and no respiratory motion compensation was used. Commercially available concomitant gradient correction was used for phase offset correction.

2.2.3. 3D vortex core identification using the Lambda2-method

In this study, vortex cores in the LV cavity were detected over the diastolic phases using the Lambda2 (λ_2)-method [28]. The Lambda2-method is an objective method that identifies 3D vortex cores based on their physical fluid dynamics properties, and is considered the most accepted vortex detection technique [31]. In short, the Lambda2-method uses the fluid's velocity gradient properties to obtain a scalar value, λ_2 . In a loose sense, this obtained scalar reflects the pressure due to velocity gradients after excluding the effect of the irrotational part of the flow. The vortex cores are then identified as the regions with extreme negative λ_2 -values. These identified vortex cores can be visualized by use of isosurfaces of isovalue T_{λ_2} , which is an application-dependent threshold. More technical background of applying the Lambda2-method on 4D Flow CMR, including the choice of the isovalue threshold, has been described earlier [32].

2.2.4. Vortex core analysis workflow

4D Flow CMR data were analyzed with in-house developed software based on Matlab (Version R2012a, Mathworks Inc., Novi, MI). First, the LV endocardial boundaries were manually delineated using MASS research software (Version 2013EXP, Leiden University Medical Center, Leiden, The Netherlands). Subsequently, the Lambda2-method was applied to the 4D Flow CMR data to identify the vortex structures within the LV blood pool. Early (E) filling and atrial (A) filling phases were defined from the flow rate-time graph after transmitral velocity mapping in combination with retrospective valve tracking [33]. For every subject, the vortex ring core (if detected) of peak early filling and peak late filling was used for further quantitative analysis. As described in previous work, the Lambda2 isovalue threshold (T_{λ_2}) was defined as $T_{\lambda_2} = \mathbf{K}\mu$ (with \mathbf{K} as a real number and μ as the λ_2 average of voxels with $\lambda_2 < 0$) with \mathbf{K} chosen as the value providing the most circular vortex ring core having the least attached trailing structures [32]. The parameter \mathbf{K} was chosen separately for every filling phase. The shape and location of the peak early (E)

and late (A) -vortex ring cores were further quantitatively analyzed using the parameters explained below. In the remainder, the vortex cores detected at peak early filling and peak late filling will be denoted as E-vortex and A-vortex, respectively.

2.2.5. 3D quantitative characterization of diastolic vortex ring core

The 3D location and orientation of the vortex ring core were quantified using a standardized 3D local cardiac (cylindrical) coordinate system, abbreviated by CLR. Every vortex ring core center was localized using its circumferential (C), longitudinal (L) and radial (R) coordinates and orientation relative to the LV as defined and illustrated in (Figure 2.1). The shapes of the vortex ring cores were quantified using a dimensionless circularity index (CI), defined as the ratio between the vortex's short (D1) to long (D2) diameters, i.e., $CI = D1/D2$ (See Figure 2.2 a).

2.2.6. Intra and interobserver reproducibility:

One observer repeated the same measurements after one week to allow assessment of intraobserver reproducibility. Two independent observers repeatedly performed measurements on all subjects to assess interobserver reproducibility of derived parameters. The observers manually defined the Lambda2 threshold (T_{λ_2}) as explained above. Then, C, L, R coordinates and orientation of vortex ring cores for both early and late filling were quantified.

2.2.7. Vortex-Mitral flow association

To investigate the relationship between the geometry of the vortex ring core and the inflow jet area through the MV, the area of MV opening was assessed at two levels using retrospective valve tracking [33]. In short, at the same phase as the selected vortex, a plane was positioned at the annulus level and a second plane at one centimeter distal to the annulus (Figure 2.2: (b)) as an approximation of the tip level of the opened MV leaflets. These planes resulted in two cross-sectional images with through-plane velocity encoding in which the flow through the opened MV was outlined (Figure 2.2: (c), (d)). The outlined regions were then used to calculate the circularity index of the inflow area at the mitral annulus level (CI_{MV}) and at the valve tip level (CI_{MV_tip}), as the ratio between the short- to long-diameters of the outlined region. The correlation between the vortex circularity index (CI_{vortex}) of the diastolic vortex ring cores (E- and A- vortex ring cores pooled together) and each of CI_{MV} and CI_{MV_tip} were then evaluated.

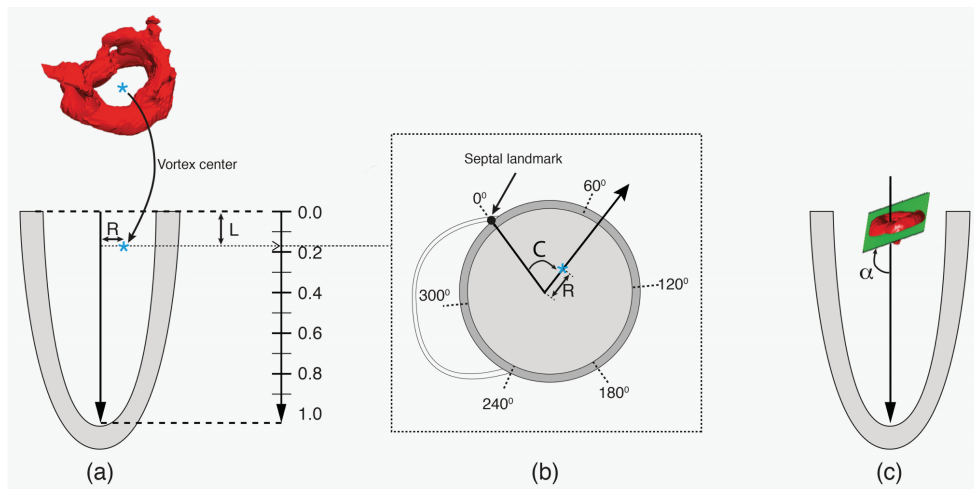


Figure 2.1. Definition of the local cardiac coordinate system (C, L, R) relative to the LV: The LV long-axis is defined as the line from the mid of the mitral valvular opening to the LV apex. The long-axis was calculated separately per filling phase (i.e. one for early filling and another for late filling). The center of the vortex ring was projected on this long-axis. The distance of the projected point to the MV and to the vortex center defined the vortex’s longitudinal (L) and radial (R) coordinates as illustrated in (a), respectively. Both L and R distances were normalized to the long-axis length and to the basal endocardial radius (measured on a reformatted short-axis slice), respectively to provide dimensionless parameters. Circumferential (C) Coordinate is defined as the angle between the septal landmark (the anterior attachment of the RV free wall with the LV) and the vortex center as illustrated in cross-sectional view (b). the vortex ring orientation (α) measured as angle between the LV long-axis vortex and a fitting plane of the vortex ring, where an orientation of 90° means a vortex ring is perpendicular to the LV long-axis as shown in (c).

2.2.8. Statistical analysis

Statistical analysis was performed using SPSS Statistics software (version 20.0 IBM SPSS, Chicago, Illinois). Quantitative parameters were presented as mean \pm standard deviation or median and inter-quartile ranges (IQR) where appropriate. Differences between E- vortex ring and A-vortex ring parameters were compared using paired Student t-test. Spearman’s correlation test was used to assess the relationship between vortex ring shape and mitral inflow area shape. Inter- and intraobserver reproducibility were determined by the interclass correlation coefficient for absolute agreement, the absolute and relative unsigned difference between measurements (with paired t-test) and the coefficients

of variance defined as the standard deviation of the difference divided by the mean of both measurements. A p-value <0.05 was considered statistically significant.

2.3. Results

2.3.1 Subject characteristics

Clinical characteristics of the study population are shown in Table 2.1. Three subjects with an absent A-vortex ring core are described separately.

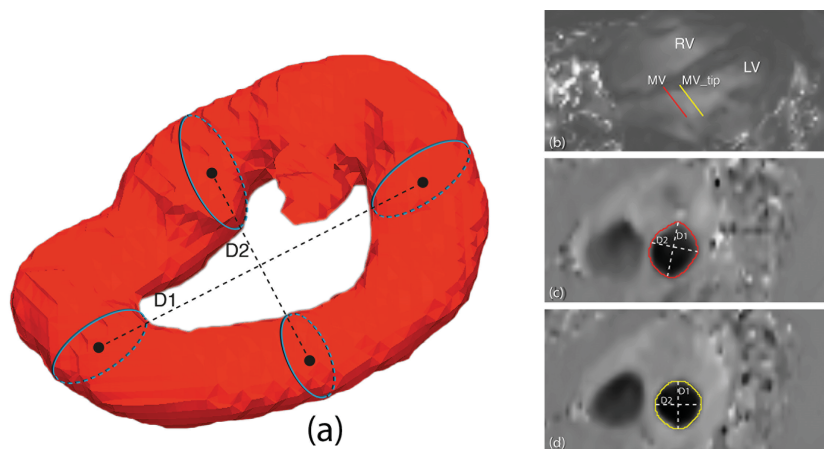


Figure 2.2. Diagram showing the measurement of the vortex circularity Index (CI). In (a), $CI=D2/D1$, D1 represents vortex's long diameter and D2 represents the vortex's shortest diameter. Both diameters measured as the distance between centers of corresponding and opposite cross-sections along the diameter of interest. (b) Two planes positioned on through-plane velocity-encoded MR images at the annulus level (red) and one centimeter distal of the annulus (yellow) resulted in two cross-sectional images of the through-plane velocity (c, d) in which the flow through MV was outlined and used to define circularity index of MV flow.

2.3.2 Characterization of 3D LV vortex ring cores

In all twenty-four subjects, during the E-filling, a compact quasi-torus-shaped vortex ring core (Figure 2.3: (a-c)) started to form distal to the mitral valve leaflets shortly after the onset of the E-filling and continued its development during the period of E-filling acceleration, reaching its full development with the E-filling approaching its peak (Figure 2.4: f1-f5). During E-filling deceleration and diastasis, the vortex core deformed into a

complex shape which tended to align with the LV long-axis (Figure 2.4: f6-f10) while progressing towards the apex. Only a remaining residual of the vortex ring core, located at the mid-ventricular level could be observed at the onset of atrial contraction and this remnant of the E-vortex ring core could not be observed anymore at end diastole (Figure 2.4: f17,f18). In the majority of subjects (twenty-one subjects, 88%), during the late diastolic filling, a new isolated compact and more asymmetrically shaped vortex ring core was formed at the ventricular basal level with a more dilated anterior side (i.e., the part close to the aortic outflow tract) and more compressed posterior side (Figure 2.3: (d-f)), reaching its complete formation while approaching peak late filling (Figure 2.4: f15-f17). The A-vortex ring core was persistently present until the end of diastole without major dissipation and was still located at the basal level (Figure 2.4: f18, f19). For the three remaining subjects, (subjects A, B and C in Table 2.1) no vortex ring core was present during late diastolic filling. Samples of the Lambda2-based detected peak early and late diastolic formed vortex ring cores are shown in Figure 2.3 and are depicted together with streamlines visualization of the velocity vector field in Figure 2.5. A time-sequence of the 3D vortex detection during the diastole is shown in Figure 2.4 (Additional file 1 and 2)^{1,2}.

2.3.3 3D Quantification of LV vortex ring core parameters

The quantified CLR parameters are presented in Table 2.2. The centers of the 3D vortex ring cores during early and late filling were located at the LV basal level, but the rings during A-filling were significantly closer to the mitral valve compared to the rings during E-filling (E-vortex $L=0.19\pm 0.04$ versus A-vortex $L=0.15\pm 0.05$; $p=0.0001$). The centers of the vortex rings during both E- and A-filling were located in the anterior and anterolateral segments (E-vortex: $C=89\pm 23^\circ$, A-vortex: $C=100\pm 23^\circ$; $p=NS$). A-filling vortex center was located closer to the ventricle's long-axis during A-filling compared to E-filling (E-vortex: $R=0.27\pm 0.07$, A-vortex: $R=0.20\pm 0.09$, $p=0.048$). Both E- and A-vortex ring cores were similarly orientated relative to the LV long-axis (E-vortex $71.0\pm 9^\circ$ versus A-vortex $74\pm 4^\circ$; $p=NS$). E-vortex rings were significantly more circular in shape compared to A-vortex rings (E-vortex: $CI=0.79\pm 0.09$, A-vortex: $CI=0.57\pm 0.06$; $p<0.001$).

¹ <http://www.jcmr-online.com/content/16/1/78/suppl/S1>

² <http://www.jcmr-online.com/content/16/1/78/suppl/S2>

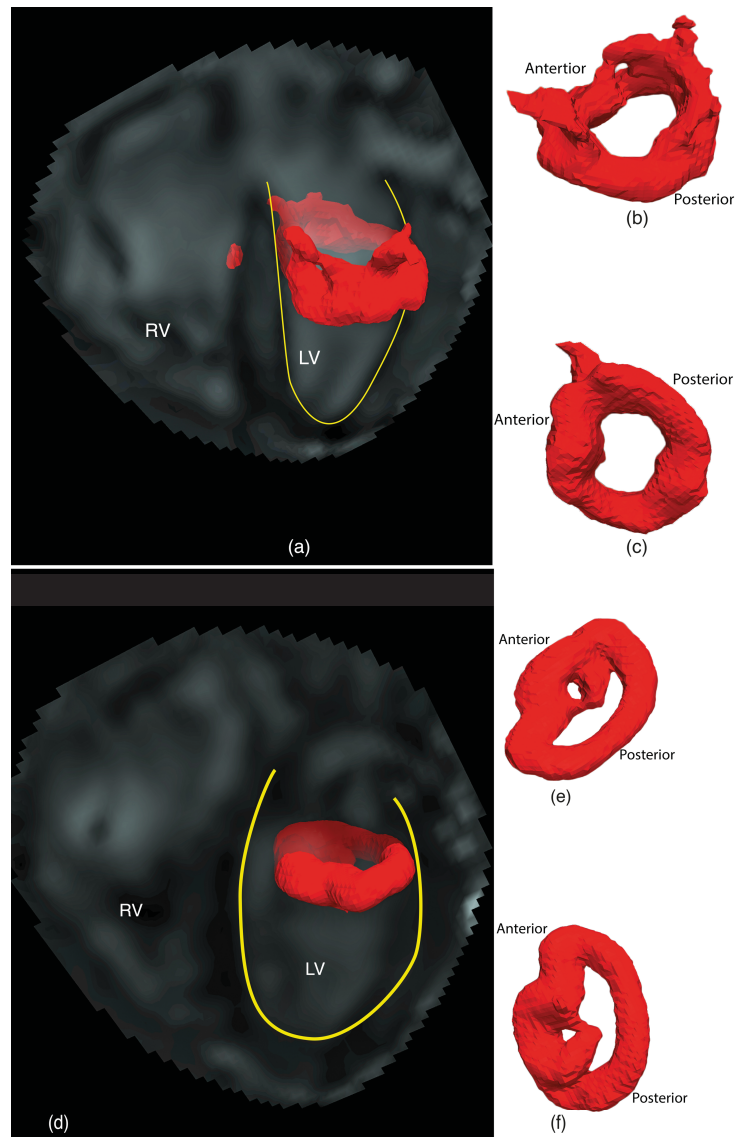


Figure 2.3. Results of Lambda2-based vortex core detection from a sample subject: (a) Identified vortex ring core at peak early (a) diastolic filling with respective location to LV (a), in top-down (b) and bottom-up (c) views. Similarly, identified peak late diastolic vortex ring core is shown in (d), (e) and (f). The core of the peak early filling vortex ring appears with a quasi-torus-like shape, more circular and symmetrical compared to the core of peak late filling vortex ring which appears more elliptical in shape and asymmetrical with dilated anterior side and compressed posterior side. Lambda2 isovalue threshold ($T_{\lambda_2} = 3\mu$) was used to define the isosurfaces of vortex ring cores (with μ as the λ_2 average of voxels with $\lambda_2 < 0$).

2.3.4 Inter and intra-observer variation

Results of inter- and intra-observer analysis for assessment of relative vortex core position and orientation are presented in Table 2.3 and Table 2.4. Inter-observer analysis revealed intraclass correlation coefficient higher or equal to 0.96 (all $p < 0.001$), with mean relative unsigned differences ranging between 1.5% and 7%, which was not statistically significant different. The coefficient of variation ranged between 1% and 3%. Intra-observer analysis showed intraclass correlation higher or equal to 0.97 (all $p < 0.001$), with a mean relative unsigned difference ranging between 0.5% and 3%, which was not statistically significant different. The coefficient of variation ranged between 1% and 8%.

Table 2.1. Study characteristics

Characteristics	21 subjects	Subject A	Subject B	Subject C	Total
age (years)	21±10	10	9	13	20±10
male/female	8/13	female	male	female	9/15
heart rate (bpm)	69±11	90	107	91	73±14
diastasis duration (ms)	108±73	22	0	0	95±77
E/A ratio	2.6±0.8	2.3	1.83	1.95	2.5±0.7

2.3.5 Vortex-Mitral flow association

The Spearman correlation coefficient between the shapes of the vortex ring (CI_{vortex}) and the MV inflow jet at the level of the annulus (CI_{MV}) was $R=0.66$ ($p < 0.001$). The correlation coefficient between CI_{vortex} with the shape of inflow jet at the tip of the valve leaflets ($CI_{\text{MV_tip}}$) was higher with $R=0.83$ ($p < 0.001$) (Figure 2.6).

2.4. Discussion

To our knowledge this is the first work to provide standardized quantitative characterization and comparison of the 3D LV vortex rings during both early and late diastolic filling in normal subjects. Using retrospective-gated 4D Flow CMR and 3D vortex core analysis, using the Lambda2-method, we observed the formation of a separate compact 3D vortex ring *in vivo* during late diastolic filling with different characteristics from the vortex ring formed during early filling. Our experiments quantitatively confirmed

the close correlation between the shape of the formed vortex ring and the shape of the inflow area through both the mitral annulus and the tip of the opened MV leaflets.

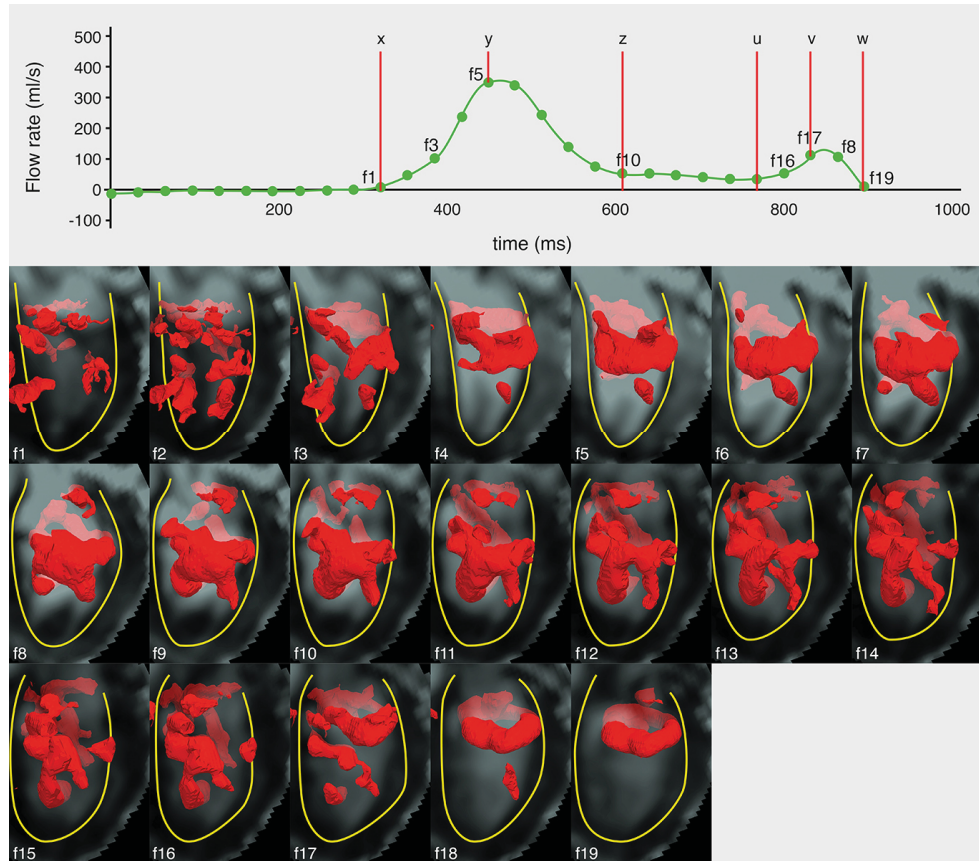


Figure 2.4. time-sequence of the Lambda2-detected 3D LV vortex structures (visualized as isosurfaces in red color) over all acquired diastolic phases of a sample normal subject, with E-filling onset (x), peak (y) and end (z), and A-filling onset (u), peak (v) and end (w). Diastasis is the duration between z and u. Every dot in the cardiac curve corresponds to a time point of the cardiac cycle in which a 4D Flow volume was acquired. With the start of diastolic phase (f1), the start of the presence of a compact ring-like shaped vortex ring during early- (f3) and late (f7) diastolic filling, the most developed vortex ring formed during early-(f5) and A-filling (f18), the start of vortex stretching or elongation in direction parallel to the LV long-axis (f10) and end of late filling while compact vortex ring is still identifiable (f19). Lambda2 isovalue threshold ($T_{\lambda_2} = 3\mu$) was used to define the isosurfaces of vortex ring cores (with μ as the λ_2 average of voxels with $\lambda_2 < 0$). To avoid cluttered view, only large scale vortex cores of 1 cm^3 or larger are visualized.

Table 2.2 Vortex quantification parameters

	C (clockwise) in degrees	L	R	Vortex Orientation in degrees	Vortex CI
E-vortex ring	89°±23°	0.19±0.04	0.27±0.07	71° ± 9°	0.79±0.09
A-vortex ring *	100°±23°	0.15±0.05	0.20±0.09	74° ± 4°	0.57±0.06
Statistical Significant	No	p=0.001	p=0.048	No	p<0.001

*In 21 subjects an A-filling vortex was observed. Data are presented as mean ± standard deviation

2.4.1 LV vortex ring formation and dynamics with emphasis on late diastolic filling

Several studies have demonstrated the presence of rotating flow distal to the MV corresponding to a compact vortex ring during the early diastolic filling. This vortex formation has been related to the normal shape and function of the LV and its alteration has been suggested to be associated with pathologies of the left ventricle [1, 4-6, 9, 11, 18, 24, 25]. In agreement with previous studies, in all subjects a compact 3D vortex ring core was identified distal to the mitral valve during the early filling phase of diastole [6, 9, 10, 18]. In previous studies, vortex analysis within LV flow has been primarily devoted to the early phase of the diastolic filling [1, 4-10, 15, 21, 34, 35]. Discrepancies exist in literature when defining or evaluating vortex formation during late diastolic filling, where CFD simulation reports vortex ring formation [12-17] and *in vivo* studies report no vortex ring formation but only a single vortex (rotating flow) distal to the anterior MV leaflet [6, 9, 19-21, 36, 37] or no vortex at all [18]. Some of the discrepancies among *in vivo* studies can be a result of limitations of the employed flow acquisition and/or analysis approach. 4D Flow CMR has intrinsic advantages over other *in vivo* flow imaging modalities such as Doppler Echocardiography or 2D phase contrast CMR, by allowing acquisition of all three directional velocity components and over the three spatial dimensions. Moreover, 4D Flow CMR provides the feasibility of retrospective flow acquisition therefore allowing acquisition of flow over both early and late diastolic filling phases instead of only the early filling phase as with prospective flow acquisition. Previous studies have successfully employed 4D Flow CMR to visualize and study LV vortex flow [6, 19, 22, 24-27]. In these studies no explicit analysis of vortex ring formation during late diastolic filling have been performed and relatively low temporal resolution (50-70 ms) were generally used [24, 27, 36] while higher temporal resolution of 30 ms was used in this study to help capturing flow

over the short duration of the late filling (five late filling phases were reconstructed on average).

Table 2.3. Inter observer analysis for C, relative L, relative R and orientation of vortex ring cores

	C	L	R	Vortex Orientation
Intraclass correlation (absolute agreement)	0.940 (p<0.001)	0.976 (p<0.001)	0.964 (p<0.001)	0.985 (p<0.001)
Mean difference	0.8	0.002	0.003	0.286
Confidence interval difference	-2.4;4.0	-0.003;0.006	-0.006;0.013	-0.239;0.811
p value difference	0.62	0.42	0.49	0.28
Mean relative unsigned difference	7%	4%	6%	1.5%
Coefficient of variance	11%	9%	13%	3%

In the current study, in agreement with CFD findings [12-17], in the majority of subjects (twenty-one subjects, 88%), a compact vortex ring core formed distal to the mitral valve during late diastolic filling. This ring formed at the basal level at the time when the remnant of the dissipating E- vortex ring core was located more apically, indicating that the A-vortex ring is a newly formed vortex as a result of the atrial contraction inflow and not just a continuation of the E-vortex. The A-vortex ring core was asymmetrically shaped in the anterior-posterior direction with a dilated anterior side, making most of the A-vortex flow being located close to the left ventricular outflow tract. This supports the postulation of Kilner et al. [6], about an expected role of the rotating flow beneath the mitral valve during the A-filling in aiding the redirection of the late diastolic inflow from the left atrium towards the left ventricular outflow tract, helping in an optimized ejection of blood. Therefore, with the revealed consistent formation of compact late diastolic vortex ring *in vivo*, extending the analysis of diastolic vortex formation to the late diastolic filling (instead of currently being limited to early filling) might help providing more understanding of the hemodynamics of the coupling between diastole and systole and associated pathologies. This emphasizes the importance of using retrospective cardiac gating when aiming for LV diastolic vortex flow analysis, where late filling phase can be acquired instead of the prospective-gating where late filling phase is generally missing. The absence of vortex ring formation during late filling in three subjects (Table 2.1) might be attributed to their age

related high heart rate and subsequent limited diastasis duration which might not allow developing the ventricular pressure gradient required for vortex formation [1].

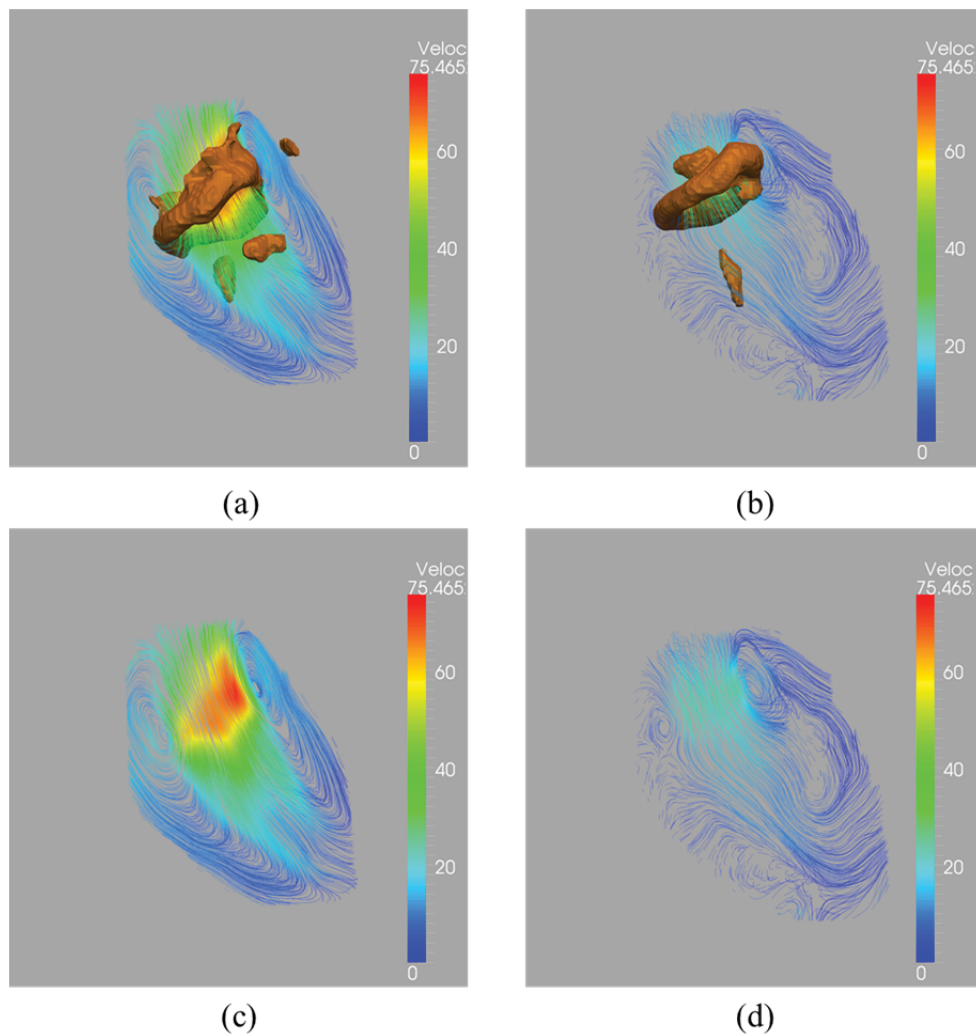


Figure 2.5. Streamline superimposed on vortex cores. Sample Streamline visualization of cross-sectional view of LV flow during peak early filling (a) peak late filling (b) showing pair of counter-rotating vortices. Streamlines are color coded (blue to red) based on velocity magnitude. Same frames were superimposed with 3D vortex ring cores identified using Lambda2-method and showing good overlap between the 3D Lambda2-detected vortex cores and the cores of corresponding 2D streamlines' counter-rotating vortices during both peak early (c) and peak late filling (d). Lambda2 isovalue threshold (T_{λ_2}) = 3μ was used to define the isosurfaces of vortex ring cores (with μ as the λ_2 average of voxels with $\lambda_2 < 0$).

2.4.2 Quantitative characterization of 3D diastolic vortex rings

Previous studies have successfully employed flow visualization techniques to identify LV vortex flow [6, 19-23, 26], quantify vortex volume [24] or evaluate early filling vortex formation [34]. However, to our knowledge, there have been no *in vivo* studies providing quantitative 3D characterization of the location and the shape of vortex flow during both early and late diastolic filling phases.

Defining the true boundary of a vortex is challenging task, especially in 3D space, as it is highly dependent on the identifier. Most *in vivo* studies identify a vortex based on visual assessment of the visualized flow [9, 11, 20, 21] which is generally an observer dependent definition. Instead, vortex cores are generally regarded as a robust and well localized approximation of a vortex [2, 3, 28, 38] and can provide more objective physical definition of a vortex. Different methods can be used for vortex core identification [13, 28-30], however, the Lambda2-method is considered the most accepted 3D vortex identification technique [1]. Vortex core analysis has been used before to detect vortices inside the heart but mainly for visualization purposes [10, 13, 27, 29, 32, 39]. In this work, we employ the 3D vortex cores identified using the Lambda2-method to derive quantitative parameters to characterize normal vortex ring formation during both peak early and peak late filling. In our experiments, following [32], Lambda2 isovalue threshold (T_{λ_2}) in the range of $[1,6] \mu$ (i.e. $\mathbf{K} = [1,6]$, with μ as the λ_2 average of voxels with $\lambda_2 < 0$) allowed identification of a separate compact vortex ring core (when detected) in all subjects. The strong inter- and intra-observer agreements (Table 2.3 and Table 2.4) indicate the robustness of the method with respect to Lambda2 threshold selection.

Table 2.4. Intra-observer analysis for C, relative L, relative R and orientation of vortex ring cores

	C	L	R	Vortex Orientation
Intraclass correlation (absolute agreement)	0.980 (p < 0.000)	0.985 (p < 0.000)	0.988 (p < 0.000)	0.971 (p < 0.000)
Mean difference	1.7	0.000	0.001	0.46444
Confidence interval difference	-0.1;3.6	-0.003;0.003	-0.004;0.007	-0.279;1.208
p value difference	0.07	0.90	0.58	0.21
Mean relative unsigned difference	3%	2%	3%	1%
Coefficient of variance	7%	7%	7%	3%

The vortex ring core is significantly closer to the mitral valve annulus (longitudinal position) at the late filling peak compared to early filling, which can be attributed to the lower velocity and shorter length of inflow jet during late filling compared to early filling. The relatively closer position of the vortex ring core to the LV long-axis (radial position) at the late filling, can be explained using the confirmed correlation between shapes of the vortex ring core and the mitral valve opening, where a restricted opening of the mitral valve during late filling results in a vortex core center closer to the long-axis compared to full valvular opening at the early filling. Since vortex ring originates from the inlet jet at the distal tip of the mitral valve (MV) leaflets [1, 10, 13], vortex ring forms parallel to the inclined MV orifice [40]. Therefore, in normal subjects, similarly oriented MV orifice of early and late filling (relative to the ventricle's long-axis) results in similarly oriented vortex rings (i.e. similar vortex orientation planes). Consequently, circumferential location (C), which is calculated using the vortex orientation plane, is similar as well between vortex rings of both early and late filling. The strong correlation between the vortex ring shape with the shape of the inflow area at the tip of the opened MV leaflets confirms the relationship between the mitral valvular opening and shape of formed vortex ring as reported earlier by CFD studies [4, 13]. To the best of our knowledge, this is the first *in vivo* study to quantitatively confirm this correlation.

The relatively small variation between normal subjects in derived parameters (Table 2.2) indicates good consistency of results. Therefore, the method defines normal quantitative ranges for diastolic vortex rings and might in future help evaluating whether changes in valve morphology or ventricular dilatation alters the location and shape of the formed vortices.

2.4.3 Clinical implications

The suggested LV-normalized vortex parameters might help to provide more insights about the normal vortex formation and provide normative parameters to compare the 3D vortex flow between controls and patients. This could help to understand the hemodynamics of patients with impaired LV relaxation and restrictive filling, where the E/A ratio is abnormal. In addition, the close correlation found between vortex formation and the flow at the tip of the opened mitral valve leaflets suggests that patients with impaired leaflet function, as can be seen in patients with left ventricular dysfunction [41] after mitral valve repair and with mitral valve stenosis, could develop aberrant vortex rings,

which possibly reduces efficiency of intra-cardiac flow. Therefore, further study is warranted to investigate the effect of mitral valve surgery on vortex formation during LV filling.

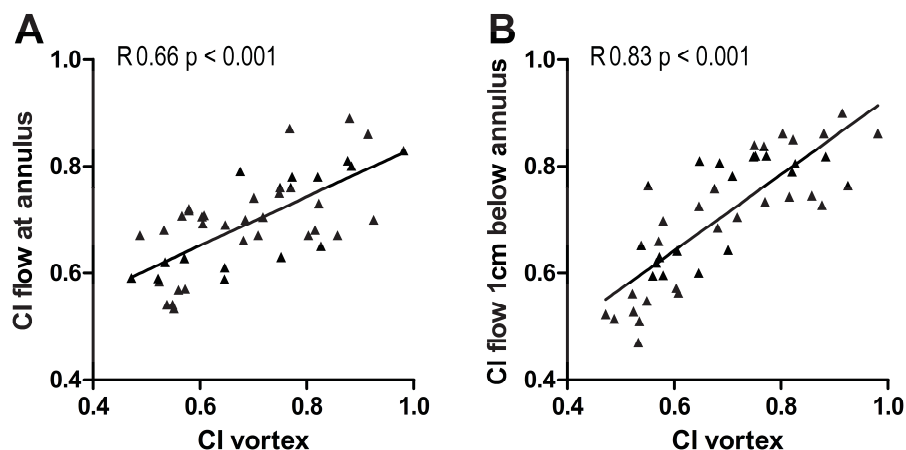


Figure 2.6. Correlation between the shape of the formed vortex ring cores (CI vortex) and the shape of the inflow area at the level of both the mitral annulus (A) and the tip of the opened MV leaflets approximated as 1 cm below the annulus (B).

2.4.4 Study limitations

Limitations of this study include a relatively small number of healthy subjects and lack of comparison with patients. However, an objective detection of possible anomalies in the vortex flow of patients should be preceded by finding reliable quantitative measures defining the reference normal vortex flow. The current study was performed in a relatively young population (age range 9 – 44 years). Global diastolic function parameters, as the E/A ratio remain relatively Table 2.2 during the second, third and fourth decade of life [42], which explains why we did not observe age related differences. As diastolic function is known to decrease later in life [43] future studies are required to compute normal values in an elderly population. Limitations of 4D Flow CMR include the relatively long scan times (typically between 8-10 minutes with heart rate 60-80bpm), and the need of averaging the data over several cardiac cycles. This time-averaging would potentially result in smoothing the low scale flow structures and does not, generally, account for flow variations due to heart rate variations. In this study, a relatively low spatial CMR resolution of $2.3 \times 2.3 \times 3\text{-}4 \text{ mm}^3$ was used. However, it was our aim to evaluate large scale vortex ring cores which are expected to have volumes significantly larger than the MR voxel size. In three volunteers, a

higher resolution of $2.3 \times 2.3 \times 3 \text{ mm}^3$ was used, which did not result in significant different findings from the other subjects. Further methodological and quantitative analysis on the effect of acquisition resolution may be helpful but was beyond the scope of this work. Identified Lambda2-based vortex cores could not be used for volumetric measurements (e.g. vortex volume or size) as applying different Lambda2 isovalue thresholds can result in different volumes for the same vortex core. Therefore, the vortex parameters derived in this study were chosen as not to be dependent on vortex volume. 4D Flow data was acquired using free breathing scans and no motion compensation was applied. Nevertheless, no motion artifacts were visually observed in the velocity data, and since all subjects underwent the same scan protocol, potential inter- and intra-subject effects on the measurements might be assumed to be similar among all subjects.

2.5. Conclusion

In summary, this is the first *in vivo* study using 4DFlow CMR to confirm previous CFD findings of vortex ring formation during late filling and to provide standardized parameters that allow quantitative characterization of vortex flow during both early and late left ventricular filling. The derived quantitative parameters provided consistent measurements within the studied population and strong correlation was found between the shape of the formed vortices and the shape of the inflow area at the level of both the mitral annulus and the tip of the opened MV leaflets. This study provides reference parameters defining normal vortex flow, which may allow objective quantitative evaluation of vortex flow in patients with cardiac disease.

Acknowledgements

We thank Pieter van den Boogaard for CMR acquisition and Gerrit Kracht for graphics design.

2.6. References

1. Kheradvar, A. and G. Pedrizzetti, Vortex formation in the cardiovascular system. 2012, Springer. p. 45-53.
2. Lim, T. and T. Nickels, Vortex rings, in Fluid vortices. 1995, Springer. p. 95-153.
3. Shariff, K. and A. Leonard, Vortex rings. Annual Review of Fluid Mechanics, 1992. 24(1): p. 235-279.
4. Pedrizzetti, G. and F. Domenichini, Nature optimizes the swirling flow in the human left ventricle. Physical review letters, 2005. 95(10): p. 108101.
5. Bellhouse, B., Fluid mechanics of a model mitral valve and left ventricle. Cardiovascular research, 1972. 6(2): p. 199-210.
6. Kilner, P.J., et al., Asymmetric redirection of flow through the heart. Nature, 2000. 404(6779): p. 759-761.

7. Ghosh, E., L. Shmuylovich, and S.J. Kovács, Vortex formation time-to-left ventricular early rapid filling relation: model-based prediction with echocardiographic validation. *Journal of Applied Physiology*, 2010. 109(6): p. 1812-1819.
8. Jiamsripong, P., et al., Impact of Acute Moderate Elevation in Left Ventricular Afterload on Diastolic Transmitral Flow Efficiency: Analysis by Vortex Formation Time. *Journal of the American Society of Echocardiography*, 2009. 22(4): p. 427-431.
9. Hong, G.R., et al., Characterization and Quantification of Vortex Flow in the Human Left Ventricle by Contrast Echocardiography Using Vector Particle Image Velocimetry. *Jacc-Cardiovascular Imaging*, 2008. 1(6): p. 705-717.
10. Domenichini, F., G. Pedrizzetti, and B. Baccani, Three-dimensional filling flow into a model left ventricle. *Journal of fluid mechanics*, 2005. 539: p. 179-198.
11. Kim, W.Y., et al., Left ventricular blood flow patterns in normal subjects: a quantitative analysis by three-dimensional magnetic resonance velocity mapping. *Journal of the American College of Cardiology*, 1995. 26(1): p. 224-238.
12. Cheng, Y., H. Oertel, and T. Schenkel, Fluid-structure coupled CFD simulation of the left ventricular flow during filling phase. *Annals of biomedical engineering*, 2005. 33(5): p. 567-576.
13. Schenkel, T., et al., MRI-based CFD analysis of flow in a human left ventricle: methodology and application to a healthy heart. *Annals of biomedical engineering*, 2009. 37(3): p. 503-515.
14. Vierendeels, J.A., E. Dick, and P.R. Verdonck, Hydrodynamics of color M-mode Doppler flow wave propagation velocity $V(p)$: a computer study. *Journal of the American Society of Echocardiography*, 2002. 15(3): p. 219-224.
15. Cooke, J., et al., Characterizing vortex ring behavior during ventricular filling with Doppler echocardiography: an in vitro study. *Annals of biomedical engineering*, 2004. 32(2): p. 245-256.
16. Saber, N.R., et al., Progress towards patient-specific computational flow modeling of the left heart via combination of magnetic resonance imaging with computational fluid dynamics. *Annals of biomedical engineering*, 2003. 31(1): p. 42-52.
17. Mihalef, V., et al., Patient-specific modelling of whole heart anatomy, dynamics and haemodynamics from four-dimensional cardiac CT images. *Interface Focus*, 2011. 1(3): p. 286-296.
18. Charonko, J.J., et al., Vortices formed on the mitral valve tips aid normal left ventricular filling. *Annals of biomedical engineering*, 2013. 41(5): p. 1049-1061.
19. Markl, M., et al., Time-resolved three-dimensional magnetic resonance velocity mapping of cardiovascular flow paths in volunteers and patients with Fontan circulation. *European Journal of Cardio-Thoracic Surgery*, 2011. 39(2): p. 206-212.
20. Abe, H., et al., Contrast echocardiography for assessing left ventricular vortex strength in heart failure: a prospective cohort study. *European Heart Journal-Cardiovascular Imaging*, 2013. 14(11): p. 1049-1060.
21. Sengupta, P.P., et al., Left ventricular isovolumic flow sequence during sinus and paced rhythms: new insights from use of high-resolution Doppler and ultrasonic digital particle imaging velocimetry. *Journal of the American College of Cardiology*, 2007. 49(8): p. 899-908.
22. Ebberts, T., Flow imaging: cardiac applications of 3D cine phase-contrast MRI. *Current Cardiovascular Imaging Reports*, 2011. 4(2): p. 127-133.
23. Markl, M., et al., Time-resolved three-dimensional phase-contrast MRI. *Journal of Magnetic Resonance Imaging*, 2003. 17(4): p. 499-506.
24. Töger, J., et al., Vortex ring formation in the left ventricle of the heart: analysis by 4D flow MRI and Lagrangian coherent structures. *Annals of biomedical engineering*, 2012. 40(12): p. 2652-2662.
25. Markl, M., P.J. Kilner, and T. Ebberts, Comprehensive 4D velocity mapping of the heart and great vessels by cardiovascular magnetic resonance. *J Cardiovasc Magn Reson*, 2011. 13(7): p. 10.1186.
26. Wigström, L., et al., Particle trace visualization of intracardiac flow using time-resolved 3D phase contrast MRI. *Magnetic Resonance in Medicine*, 1999. 41(4): p. 793-799.

27. Bolger, A.F., et al., Transit of blood flow through the human left ventricle mapped by cardiovascular magnetic resonance. *Journal of Cardiovascular Magnetic Resonance*, 2007. 9(5): p. 741-747.
28. Jeong, J. and F. Hussain, On the identification of a vortex. *Journal of fluid mechanics*, 1995. 285: p. 69-94.
29. Heiberg, E., et al., Three-dimensional flow characterization using vector pattern matching. *Visualization and Computer Graphics, IEEE Transactions on*, 2003. 9(3): p. 313-319.
30. Jiang, M., R. Machiraju, and D. Thompson, Detection and Visualization of Vortices. *The Visualization Handbook*, 2005: p. 295.
31. Kheradvar, A. and G. Pedrizzetti, Vortex formation in the cardiovascular system. 2012, Springer. p. 30.
32. ElBaz, M.S., et al., Automatic extraction of the 3D left ventricular diastolic transmitral vortex ring from 3D whole-heart phase contrast MRI using Laplace-Beltrami signatures, in *Statistical Atlases and Computational Models of the Heart. Imaging and Modelling Challenges*. 2014, Springer. p. 204-211.
33. Westenberg, J.J., et al., Mitral Valve and Tricuspid Valve Blood Flow: Accurate Quantification with 3D Velocity-encoded MR Imaging with Retrospective Valve Tracking I. *Radiology*, 2008. 249(3): p. 792-800.
34. Gharib, M., et al., Optimal vortex formation as an index of cardiac health. *Proceedings of the National Academy of Sciences*, 2006. 103(16): p. 6305-6308.
35. Kheradvar, A., et al., Assessment of transmitral vortex formation in patients with diastolic dysfunction. *Journal of the American Society of Echocardiography*, 2012. 25(2): p. 220-227.
36. Eriksson, J., et al., Quantification of presystolic blood flow organization and energetics in the human left ventricle. *American Journal of Physiology-Heart and Circulatory Physiology*, 2011. 300(6): p. H2135-H2141.
37. Eriksson, J., et al., Semi-automatic quantification of 4D left ventricular blood flow. *J Cardiovasc Magn Reson*, 2010. 12(9): p. 12.
38. Chakraborty, P., S. Balachandar, and R.J. Adrian, On the relationships between local vortex identification schemes. *Journal of Fluid Mechanics*, 2005. 535: p. 189-214.
39. Pedrizzetti, G., F. Domenichini, and G. Tonti, On the left ventricular vortex reversal after mitral valve replacement. *Annals of biomedical engineering*, 2010. 38(3): p. 769-773.
40. Le, T.B. and F. Sotiropoulos, On the three-dimensional vortical structure of early diastolic flow in a patient-specific left ventricle. *European Journal of Mechanics-B/Fluids*, 2012. 35: p. 20-24.
41. Otsuji, Y., et al., Restricted diastolic opening of the mitral leaflets in patients with left ventricular dysfunction: evidence for increased valve tethering. *Journal of the American College of Cardiology*, 1998. 32(2): p. 398-404.
42. Schmitz, L., et al., Left ventricular diastolic function in infants, children, and adolescents. Reference values and analysis of morphologic and physiologic determinants of echocardiographic Doppler flow signals during growth and maturation. *Journal of the American College of Cardiology*, 1998. 32(5): p. 1441-1448.
43. Nagueh, S.F., et al., Recommendations for the evaluation of left ventricular diastolic function by echocardiography. *Journal of the American Society of Echocardiography*, 2009. 22(2): p. 107-133.

Chapter 3

Altered left ventricular vortex ring formation by 4-dimensional flow magnetic resonance imaging after repair of atrioventricular septal defects

This chapter was adapted from:

Calkoen, E. E.*, Elbaz, M. S.*, Westenberg, J. J., Kroft, L. J., Hazekamp, M. G., Roest, A. A., & van der Geest, R. J. (2015). **Altered left ventricular vortex ring formation by 4-dimensional flow magnetic resonance imaging after repair of atrioventricular septal defects.** *The Journal of thoracic and cardiovascular surgery*, 150(5), 1233-1240.

* Calkoen, E. E. and Elbaz, M. S. contributed equally to this work.

Abstract

Objectives: During normal left ventricular (LV) filling, a vortex ring structure is formed distal to the left atrioventricular valve (LAVV). Vortex structures contribute to efficient flow organization. We aimed to investigate whether LAVV abnormality in patients with a corrected atrioventricular septal defect (AVSD) has an impact on vortex ring formation.

Methods: Whole-heart 4D flow MRI was performed in 32 patients (age: 26 ± 12 years), and 30 healthy subjects (age: 25 ± 14 years). Vortex ring cores were detected at peak early (E-peak) and peak late filling (A-peak). When present, the 3-dimensional position and orientation of the vortex ring was defined, and the circularity index was calculated. Through-plane flow over the LAVV, and the vortex formation time (VFT), were quantified to analyze the relationship of vortex flow with the inflow jet.

Results: Absence of a vortex ring during E-peak (healthy subjects 0%, vs patients 19%; $P = 0.015$), and A-peak (healthy subjects 10% vs patients 44%; $P = 0.008$) was more frequent in patients. In 4 patients, this was accompanied by a high VFT ($5.1-7.8$ vs 2.4 ± 0.6 in healthy subjects), and in another 2 patients with abnormal valve anatomy. In patients compared with controls, the vortex cores had a more- anterior and apical position, closer to the ventricular wall, with a more-elliptical shape and oblique orientation. The shape of the vortex core closely resembled the valve shape, and its orientation was related to the LV inflow direction.

Conclusions: This study quantitatively shows the influence of abnormal LAVV and LV inflow on 3D vortex ring formation during LV inflow in patients with corrected AVSD, compared with healthy subjects.

3.1. Introduction

Patients with an atrioventricular septal defect (AVSD) require corrective surgery early in life to prevent pulmonary overflow and heart failure. Compared with a normal mitral valve, the mural (posterior) leaflet of the left atrio-ventricular valve (LAVV) is smaller, and the anterolateral papillary muscle is positioned more laterally in AVSD hearts [1, 2]. Furthermore, the presence of a single papillary muscle and double orifice are described [3]. Moreover, surgical correction of an AVSD, including closure of the “cleft,” may result in restricted opening of the LAVV[4] and a more-lateral inflow [5], which might affect efficiency of cardiac blood flow in the left ventricle (LV).

Survival after surgical correction is excellent in the current era, but the reoperation rate due to valve regurgitation is high [6, 7]. Long-term follow-up data on cardiac function or exercise capacity after AVSD correction are lacking. However, deterioration of cardiac function and New York Heart Association class is described during pregnancy, when cardiac flow increases [8].

Recently, the formation of a vortex within the LV during diastole was related to the inflow area through the mitral valve in healthy subjects [9]. The formation of vortex structures (ie, compact regions of swirling blood flow) in LV blood flow patterns during diastolic filling has recently emerged as a potential novel index for characterizing efficient LV blood flow and evaluating cardiac chamber (dys) function [10]. During LV filling, a vortex ring structure distal to the mitral valve leaflets and enclosing the inflow jet is observed. This vortical flow is considered an efficient mechanism for transporting a significant portion of LV-filling volume toward the aorta [11], minimizing energy loss, and helping mitral valve closure [12, 13]. Recently, 3-directional, 3-dimensional (3D) and time-resolved velocity-encoded MRI (magnetic resonance imaging; 4D flow MRI) has been introduced to assess vortex ring formation during LV filling in vivo [9], because it has the advantage of a 3D evaluation of the vortex ring.

Given the relationship between the vortex ring properties and the mitral valve morphology and LV inflow [9, 14-17], we hypothesized that LAVV abnormalities, and associated abnormal lateral inflow⁵ after surgical AVSD correction, may result in disturbed vortex flow during LV filling. Therefore, we used 4D flow MRI to identify and quantitatively characterize the geometric properties and anatomic location of vortex ring cores during early and late LV filling, allowing quantitative assessment of 3D vortex ring properties in AVSD-corrected patients and comparison with healthy controls.

3.2. Methods

3.2.1 Study Population

The study was approved by the ethical committee of the Leiden University Medical Center, and written informed consent was obtained from all participants or their parents. Thirty-two patients with a history of corrected AVSD were prospectively enrolled from a surgical database [18]. Thirty healthy subjects of similar age, without a history of cardiac disease, were included for comparison.

Participants in the current study were included in previous studies with the aim of characterizing and quantifying diastolic transatrioventricular flow [5, 19]. Twenty-four of the 30 healthy subjects were included in a study that provided reference values for 3D vortex LV flow [9]. None of the previously published papers addresses vortex formation in corrected AVSD patients. For clarity, we use the term ‘‘left atrioventricular valve’’ (LAVV) in patients and controls, instead of referring to the mitral valve in healthy subjects, and the LAVV in patients.

3.2.2 Magnetic Resonance Imaging Acquisition and Analysis

Whole-heart 4D flow was obtained on a 3T MRI scanner (Ingenia; Phillips Medical Systems International, Best, The Netherlands), with a maximal gradient amplitude of 45 mT/m for each axis, and a slew rate of 200 T/m/s, using a combination of FlexCoverage Posterior coil in the tabletop with a dStream Torso coil, providing up to 32 coil elements for signal reception. Imaging details are reported elsewhere [5].

In short, a 3D volume acquisition of the heart was performed with a velocity encoding of 150 cm/s in all 3 directions, and spatial resolution of $2.3 \times 2.3 \times 3.0 - 4.2$ mm³; 30 cardiac phases were retrospectively reconstructed to represent one average heartbeat, with a maximal true temporal resolution of 31ms. Furthermore, to quantify LV volumes and ejection fraction, a left 2-chamber and 4-chamber cine view, and a short-axis cine stack of slices, was acquired with steady-state free-precession sequences as reported elsewhere [5]. Spatial resolution was $1.0 \times 1.0 \times 8.0$ mm³; in addition, for these acquisitions, 30 phases were retrospectively reconstructed.

All acquisitions were performed with free breathing and no respiratory motion control. The cine steady-state free-precession acquisitions were all performed with 3 signal averages to suppress breathing artifacts. After manual segmentation of LV endocardial boundaries, the LV end-diastolic volume (LVEDV), end-systolic volume (ESV), and

ejection fraction were calculated. The sphericity index of the LV was calculated as $LVEDV/(\pi/6 \times \text{long-axis at end-diastole})$ [3].

3.2.3 A 3D Vortex Core Analysis Based on the Lambda2 Method

Using the image analysis workflow described elsewhere [9], the cores of vortex structures within the LV blood flow during diastole, as acquired from the 4D flow MRI data, were identified by a single observer using the Lambda2 method [20]. In short, the Lambda2 method is a fluid-dynamics-based method that uses the gradient properties of the velocity field to identify vortex cores in the flow. For each subject, the vortex cores were identified at the early (E-peak) and late (A-peak) filling, defined from the trans-LAVV flow quantification, described later, and visualized as isosurfaces.

Qualitative visual inspection of the shape of detected vortex cores was performed to determine whether a 3D ring-shaped vortex core was present, defined as a vortex core with a donut-like (torus) shape (Figure 3.1). If a vortex ring core was detected during E-peak and/or A-peak, its 3D position (in normalized cylindrical coordinates), orientation, and shape were quantitatively characterized, as illustrated in Figure 3.1.

3.2.4 Trans-Left Atrioventricular Valve Flow

Trans-LAVV flow was quantified using the 4D flow MRI data and retrospective valve tracking [21]. From the through-plane LAVV velocity map, a flow-time curve of the LAVV flow was computed, and E-peak and A-peak were defined. The early LV filling fraction was calculated as $(\text{E-wave inflow volume}/\text{total inflow volume}) \times 100\%$. To study the association with diastolic vortex formation, LAVV and inflow characteristics were evaluated. The inflow area and peak velocity during E-peak were quantified at the level of peak inflow velocity. The peak velocity inflow angle (ie, angle between the long-axis and inflow direction) at E-peak was measured using streamline visualization of the flow velocity field on the 4-chamber view, as previously described [5].

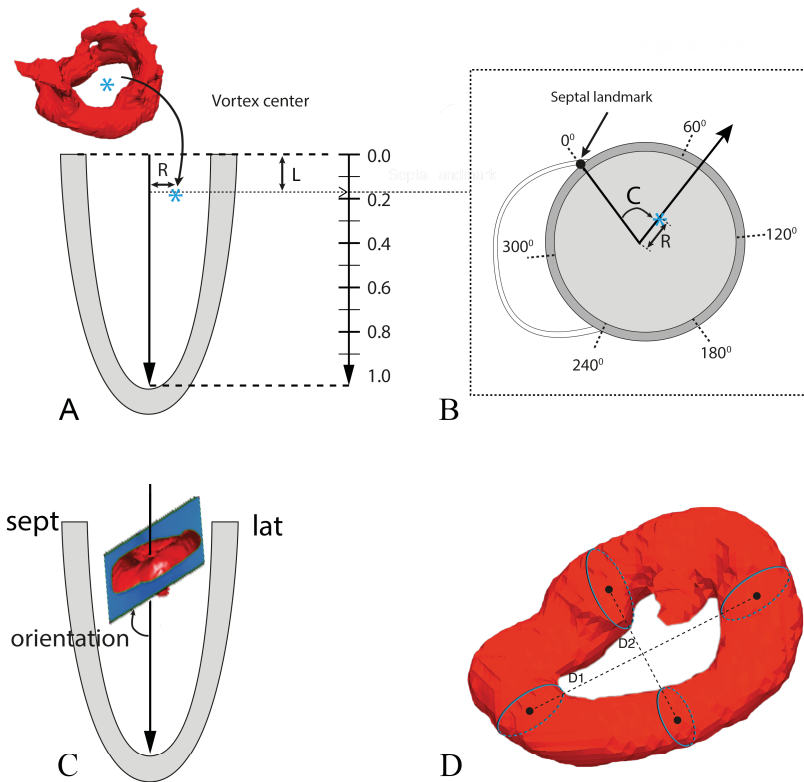


Figure 3.1. The 3-dimensional quantitative vortex core parameters. The cylindrical position of the (A) vortex core center (asterisk) was defined using L, C, and R coordinates relative to LV (A, B). L and R were normalized relative to the LV long-axis length and the radius of the LV endocardial cavity, respectively. The orientation angle was defined relative to the long-axis (C). The circularity index was defined as the ratio between the longest (D1) and shortest (D2) diameter (D). (Modified after Elbaz and colleagues [9]). R, Radial; L, longitudinal; C, circumferential; sept, septal; lat, lateral; D1, longest diameter; D2, shortest diameter.

3.2.5 Vortex Formation Time Index

The vortex formation time (VFT), a dimensionless index previously proposed to quantify the process of vortex progression during early filling [22], was determined using the formula: $VFT = (V_{avg} \times E_{duration})/D$, based on the average speed of blood flow during the early filling period (V_{avg}), the duration of the E-filling ($E_{duration}$), and the maximum diameter (D). The D denominator was computed at E-peak from the area of the LAVV flow, measured on the velocity map after retrospective valve tracking at peak

velocity level (ie, tip of the valves). The diameter was calculated as D , assuming the inflow area to be circular.

3.2.6 Statistical Analysis

Data analysis was performed using SPSS (version 20.0, SPSS, Inc, Chicago, Ill). Variables were tested for normal distribution using the Shapiro-Wilk test. Continuous variables are expressed as mean \pm SD, or as median with interquartile range (IQR), as appropriate. Differences between presences of E-peak versus A-peak vortex ring core were tested with a Pearson χ^2 analysis. Differences between patients and controls, and subjects with versus without E-peak vortex ring core, were assessed using an unpaired t test or a Mann-Whitney U test. Correlation between inflow directions, LV volume, and vortex position parameters were assessed with linear regression analysis (Pearson r).

3.3. Results

3.3.1 Patient Characteristics

Characteristics of patients and healthy controls are presented in Table 3.1. Of 32 patients, 1 had a double-orifice LAVV [3], 1 had a single papillary muscle [3], and another was known to have dextrocardia. In patients compared with controls, the mean LV ejection fraction was lower, diastasis was shorter, and the LV sphericity index was higher.

3.3.2 Presence of 3D Vortex Cores during E-Peak and A-Peak

In all controls, during peak E-filling, a quasi-ring-shaped vortex core was identified distal to the mitral valve in the LV blood flow pattern (Figure 3.2). In 26 (81%; $P=0.015$) patients, such a compact 3D vortex ring core distal to the LAVV was identified during peak E-filling. The shape of the detected 3D vortex ring cores in patients was more frequently deformed, albeit that the vortex cores were still compact and recognizable (Figure 3.2).

Visually, the shape of the vortex core tended to resemble the shape of the inflow area over the LAVV, as observed on the through-plane velocity maps (Figure 3.2). In 6 patients (19%) (Table 3.2), no E-peak vortex ring core was detected; instead, only a complex irregular vortex shape was present. The 6 patients included the patient with a double-orifice LAVV (Figure 3.4), and the patient with a single papillary muscle. The other 4 patients without an E-peak vortex ring core had a small LAVV area, higher peak velocity, and VFT deviating more than 2 SD (VFT = 5.1, 5.5, 7.4, and 7.8) (Table 3.2) from that for healthy participants (2.6 ± 0.6). The other patients with an E-peak vortex ring core had a mean VFT

of 2.4 ± 0.6 , which was very similar to the healthy participants. The LV shape parameters LVEDV and sphericity index, of the 6 patients without E-peak vortex, still fell within the ranges of the patients with an E-peak vortex ring core.

At peak A-filling, an asymmetric compact vortex ring core formed at the basal LV level in 27 healthy subjects (90%), but only 19 (59%; $P = 0.006$) patients. Details of patients with and without A-peak vortex ring core are presented in Table 3.3. Patients and healthy subjects without an A-peak vortex ring core had shorter diastasis (14 ± 17 ms), compared with patients and controls with an A-peak vortex ring (109 ± 85 ms; $P < 0.001$).

3.3.3 Quantitative 3D Parameters of Vortex Ring Cores and Association with the LAVV and LV Characteristics

The circumferential, longitudinal, and radial position, orientation, and circularity index were quantified for all detected vortex ring cores. During E-peak and A-peak, the center of the vortex ring core was positioned more anteriorly (lower circumferential value), closer to the apex (higher longitudinal value), and closer to the LV wall (higher radial value) in patients, compared with control subjects (Table 3.4).

In healthy subjects, the vortex orientation ranged from 55° to 88° , whereas in patients, the vortex orientation showed a wider range (14° - 134°). Three patients had a vortex orientation angle $> 90^\circ$ (ie, 102° , 115° , and 134°), indicating a reversed orientation of the ring (Figure 3.5), with the lateral side of the vortex being positioned toward the apex, in contrast to the control subjects, for whom the septal side was positioned more apically. In patients with nonreversed vortex ring cores (orientation $< 90^\circ$), cores were in a more-tilted position ($50^\circ \pm 20^\circ$), compared with the position in healthy subjects ($71^\circ \pm 9^\circ$; $P < 0.001$) (Figure 3.3).

During A-peak, the vortex ring core orientation was in a nonreversed, more-tilted position in all patients, compared with control subjects ($54^\circ \pm 21^\circ$ vs $72^\circ \pm 6^\circ$; $P = .001$). During both E-peak and A-peak, vortex ring cores were less circular in patients, compared with healthy subjects (Figure 3.3; Table 3.4). In patients, vortex ring core orientation angle relative to the LV long-axis showed a significant correlation with the inflow angle (E-peak $r = 0.41$; $P = .037$; A-peak $r = .62$; $P = .005$); inflow area during E-peak ($r = 0.47$; $P = .015$); and LVEDV (E-peak $r = 0.61$; $P = .001$; A-peak $r = 0.54$; $P = .017$).

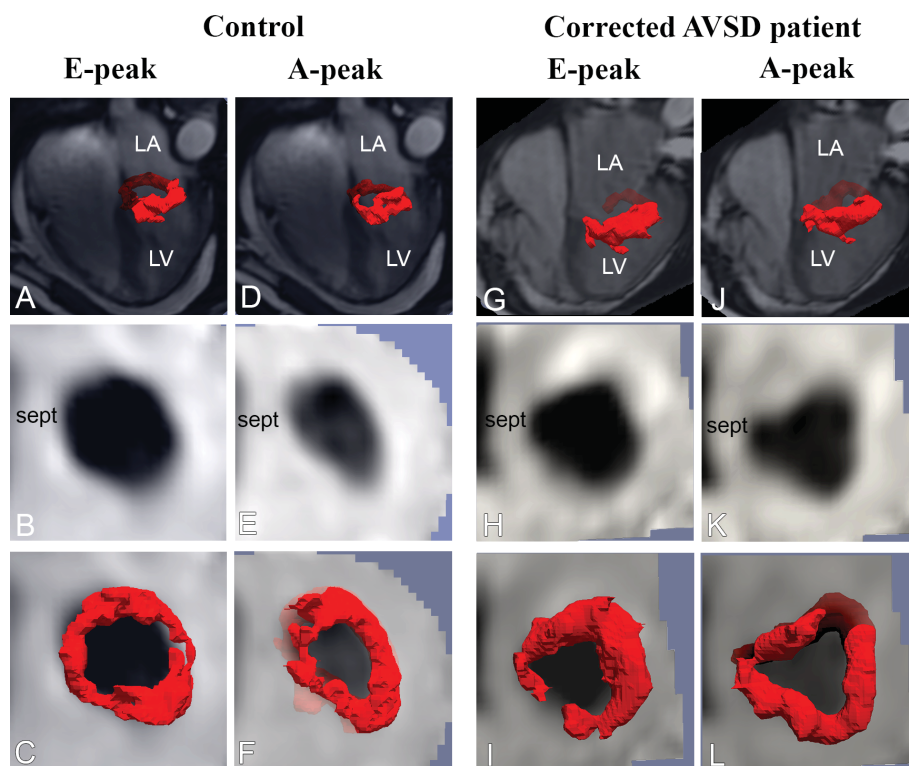


Figure 3.2. Shape of vortex core corresponds with the inflow area. Vortex cores depicted on reformat planes of through-plane flow at peak inflow velocity (B, E, H, K) during E-peak and A-peak in a healthy subject (A-F) and a patient (G-L). AVSD, Atrioventricular septal defect; E-peak, early filling; A-peak, late filling; LA, left atrium; LV, left ventricle; Sept, septal side.

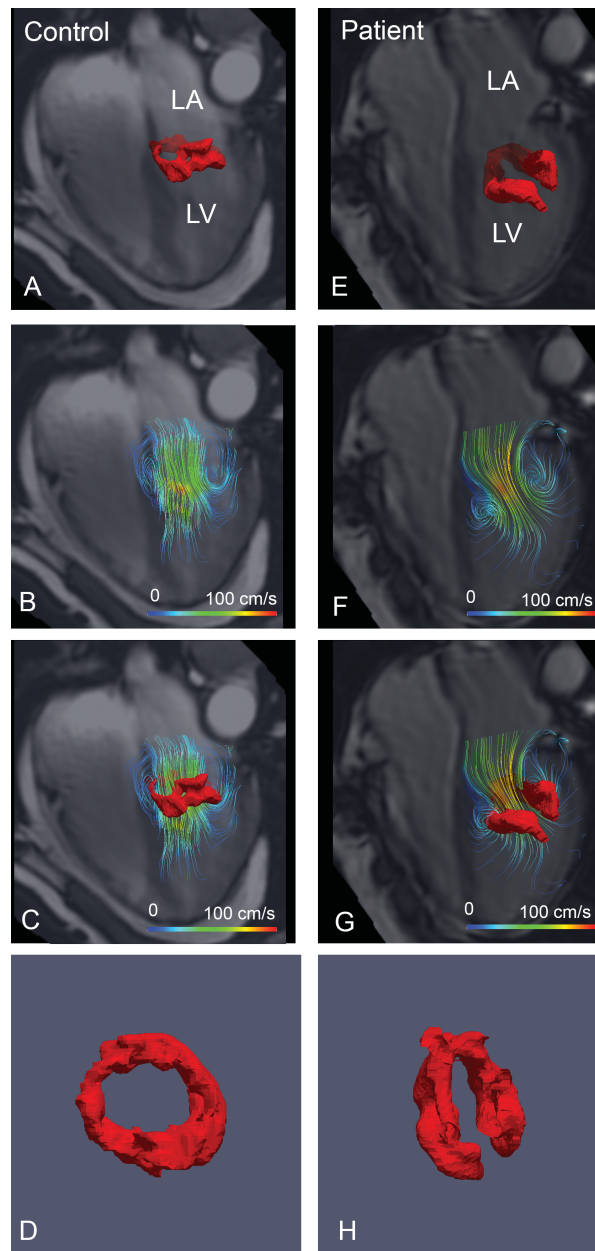


Figure 3.3. Example of a vortex core during early filling in a patient (E-H) and a healthy subject (A-D). Streamline visualization (color coding represents velocity magnitude) shows a more lateral inflow direction in the patient (F) compared with the control (B). The vortex core has a more-tilted orientation (G) and elliptical shape (H) in the patient, compared with the healthy control (C-D). LA, Left atrium; LV, left ventricle.

In healthy subjects, no significant correlations were found between orientation angle and inflow angle, inflow area, or LVEDV. In patients, the sphericity index of the LV did not show a relationship with vortex ring core characteristics. Ejection fraction did not correlate with vortex ring core presence or characteristics. In patients, no significant correlation ($P = 0.97$) was found between regurgitation fraction and vortex orientation.

Table 3.1 Characteristics of healthy subjects and patients

Characteristics	Healthy subjects	Patients with corrected AVSD
Age (y)	23 (13-38)	26 ± 12
Male (%)	14 (46)	9 (28)
Heart rate (bpm)	68 (60-78)	76 ± 13
Diastasis (ms)	116 ± 89	26 (0-67) ^{a, b}
Type AVSD	—	21 (66%) partial, 11 (33%) complete or intermediate
Time after surgical correction (y)		20 ± 9
Stroke volume LV (mL)	89 ± 23	85 ± 19
LVEDV (mL)	146 ± 42	155 ± 33
LVEDV/BSA (mL/m ²)	87 ± 13	91 ± 15
LV sphericity index	0.37 ± 0.06	0.57 ± 0.14 ^c
Inflow area (cm ²)	9.2 ± 2.0	8.5 ± 2.5
Peak velocity (cm/s)	94 ± 15	93 (77-145)
VFT index	2.6 ± 0.6	2.4 (1.9-3.1)
Blood pressure systolic (mm Hg)	112 ± 13	119 ± 20
Blood pressure diastolic (mm Hg)	67 ± 9	67 ± 12
E/A ratio peak flow rate	2.5 ± 0.8	2.1 (1.7-2.6) ^a
Early filling fraction (%)	76 ± 5	73 ± 13
Ejection fraction (%)	61 ± 5	56 (52-58) ^c
LAVV regurgitation (%)	—	14 ± 8

Boldface indicated the time after surgical correction. AVSD, Atrioventricular septal defect; bpm, beats per minute; LV, left ventricle; LVEDV, left ventricular end-diastolic volume; BSA, body surface area; VFT, vortex formation time; LAVV, left atrioventricular valve; E/A, early/late filling. ^a Excluding 2 cases without late-peak filling. ^b $P < .01$, ^c $P < .001$.

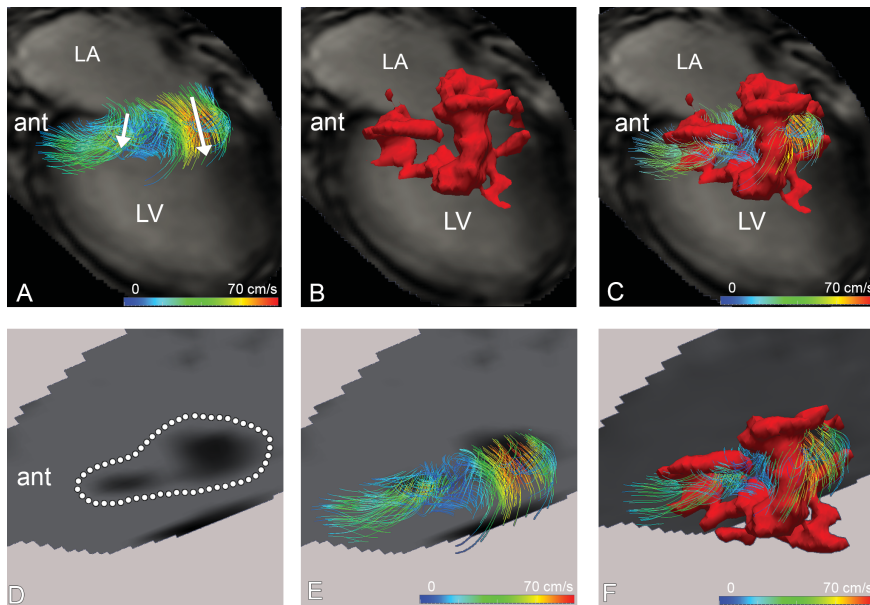


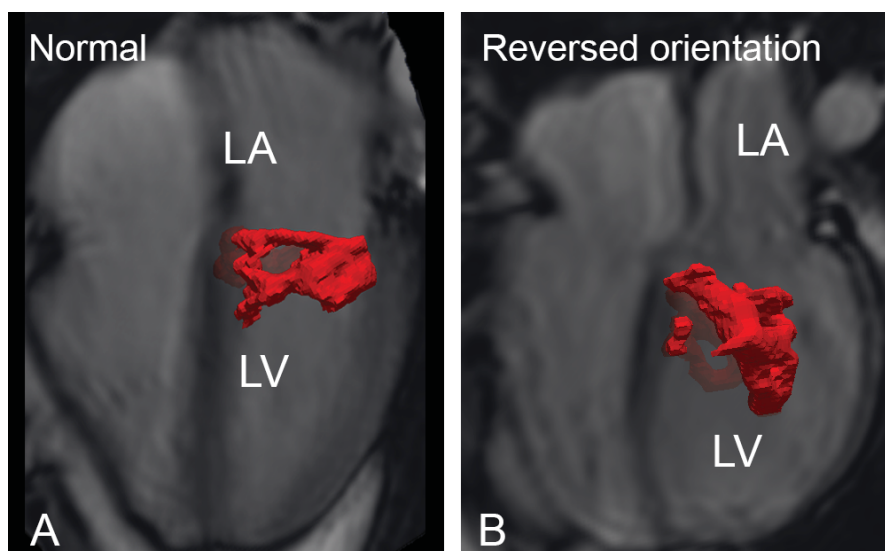
Figure 3.4. Patient with a double-orifice LAVV showed 2 separate inflow jets. Streamlines (color coding representing velocity magnitude) show (A) 2 inflow jets (white arrows). The vortex core had a complex shape (B), but fit with streamlines (C). (D) Through-plane flow analysis showed 3 jets in the LAVV (dotted line). Positioning the streamlines (E) and vortex core (F) on top of the velocity map shows that a core is formed around both jets. LA, Left atrium; LV, Left ventricle.

3.4. Discussion

This study, for the first time, quantitatively describes the effect of LAVV abnormalities and abnormal LV inflow on 3D vortex ring formation in LV blood flow patterns during early and late filling, in patients with surgically corrected LAVV valves compared with healthy subjects. These findings highlight the close relationship between AVV morphology and LV filling characteristics, with LV vortex formation. Previous studies on vortex formation in the presence of LAVV abnormalities were performed *in vitro*, or were based on 2-dimensional analysis using echocardiography.

The current report provides an *in vivo* 3D analysis using 4D flow MRI. Key findings are as follows: (1) Absence of vortex ring formation is more frequent in corrected-AVSD patients and is related to LAVV abnormalities (single papillary muscle and double-orifice) and a narrow LAVV diameter concomitant with high inflow velocities evidenced by a high VFT. (2) If a vortex ring core is present in corrected-AVSD patients, it has a different

position, a more-elliptical shape, and an oblique orientation compared with controls, and these differences correlate with LV inflow direction.



3

Figure 3.5. Reversed orientation of the vortex ring core in a corrected AVSD patient. Healthy subject (A), and patients (B). LA, Left atrium; LV, left ventricle; ant, anterior.

3.4.1 Absence of Vortex Ring Core Related to Valve Morphology and VFT

In the normal heart, adequate suction, correct shape of the valve leaflets, and normal electrical conduction allow vortex ring formation during LV filling [23]. In our study, 6 patients did not develop a vortex ring. One of these patients had a double-orifice LAVV, resulting in 2 inflow jets, as is seen after edge-to-edge repair. Absence of a ring in this patient is in agreement with computational fluid dynamics studies simulating edge-to-edge repair, resulting in abnormal vortex formation with increased energy loss and decreased LV filling efficiency [24]. Another patient without vortex ring formation had a single papillary muscle, stressing the contribution of the papillary muscles to the shape of the vortex ring [25].

Both cases underline the influence of morphologic LAVV abnormalities on vortex formation. Next to 2 patients with abnormal anatomy, 4 other patients were observed without E-peak vortex ring formation. These 4 had a VFT more than 2 SDs higher, compared with patients with an E-peak vortex ring core and with healthy subjects. The VFT index, studied *in vitro* and *in vivo*, is known to have an optimal value range that defines efficient vortex formation [22, 26]. In patients with mitral stenosis, higher values of

VFT have been related to the absence of a well-formed vortex ring, resulting in increased energy dissipation [27].

In the current MRI study, the VFT values in healthy subjects were lower than the reported range (3.5-5.5) measured with echocardiography [22]. This difference might be due to differences between modalities [28] and their definition of valve diameter measurement. However, the markedly higher VFT values in patients with an absent vortex ring confirms that patients with a narrow LAVV diameter and a higher peak velocity develop abnormal vortex flow [22, 26]. In addition, VFT measurements were comparable and not significantly different between controls and patients when an E-vortex ring core was present. Absence of a separate A-peak vortex ring core was related to the shorter diastasis in patients, similar to what is reported in healthy controls [9].

3.4.2 Vortex Ring Formation Related to LAVV and LV Characteristics

In normal hearts, a vortex ring forms at the tip of the LAVV [29], with the septal side positioned toward the apex, owing to the unbalanced shape of the leaflets (ie, longer anterior and shorter posterior leaflet) and interaction with the LV wall [23, 29]. The visual similarity between the 3D shape of the vortex ring core and the (abnormal) LAVV orifices (ie, LAVV inflow area) in this study illustrates the impact of the abnormal LAVV on vortex ring formation. Moreover, the observed correlation between disturbed vortex characteristics and altered inflow area and direction, indicates an influence of abnormal valve and inflow on vortex ring formation.

Our findings are in agreement with computational fluid dynamics experiments [16], 2-dimensional echocardiography analysis in human [17, 30], and an MRI study in sheep [31] showing that LAVV repair and replacement are related to unnatural vortex formation. Aside from the impact of the valve abnormalities, the correlation between vortex ring orientation and LVEDV shows an impact of LV size on vortex formation. This finding is in agreement with the relationship between LVEDV and vortex size observed in patients with dilated cardiomyopathy [32].

Table 3.2. Characteristics of the 6 patients without a vortex ring core during E-peak or A-peak.

Characteristics	Pt 1	Pt 2	Pt 3	Pt 4	Pt 5	Pt 6
Age	10	23	20	36	12	32
Type AVSD	Partial double-orifices	Complete single papillary muscle	Partial	Complete	Complete	Complete dextrocardia
Regurgitation %	10	23	20	36	12	32
Heart rate (bpm)	76	78	96	114	60	62
Diastasis (ms)	24	0	No A-peak	No A-peak	0	0
Early filling fraction (%)	61	80	100	100	81	88
Area LAVV (cm ²)	9.2	8.4	6.0	5.1	4.6	4.6
Peak velocity (cm/s)	58	110	144	158	146	155
VFT	1.6	2.5	5.1	5.5	7.8	7.4

AVSD, Atrioventricular septal defect; Pt, patient; A-peak, late-peak filling; bpm, beats per minute; LAVV, left atrioventricular valve; VFT, vortex formation

Table 3.3. Characteristics of healthy subjects and patients with a vortex ring core present during E-peak

Characteristics	Controls with E- and A-peak ring	Controls with only E-peak ring	Patients with E- and A-peak ring	Patients with only E-peak ring
N	27	3	19	7
Age	26 ± 13	11 ± 2	26 ± 14	28 ± 8
Type AVSD	-	-	14 partial 5 complete	5 partial 2 complete
Regurgitation %	-	-	12 ± 8	13 ± 6
Heart rate (bpm)	67 ± 10	95 ± 7	72 ± 12	80 ± 4
Diastasis (ms)	128 ± 86	7 ± 13	81 ± 79	22 ± 18
Passive filling fraction (%)	76 ± 5	79 ± 2	72 ± 11	68 ± 10
Area LAVV (cm ²)	9.5 ± 1.9	6.4 ± 0.8	8.8 ± 2.5	9.3 ± 2.3
Peak velocity (cm/s)	93 ± 16	105 ± 4	92 ± 15	94 ± 28
VFT	2.6 ± 0.6	2.6 ± 0.2	2.4 ± 0.6	2.4 ± 0.5

Values are mean ± SD, unless otherwise indicated. E-peak, Early-peak filling; A-peak, late-peak filling; AVSD, atrioventricular septal defect; bpm, beats per minute; LAVV, left atrioventricular valve; VFT, vortex formation time.

In the current study, no relationship was found between vortex ring core characteristics and sphericity index, as described in a previous study using vortex filling fraction [11]. However, absence of such a correlation might be due to the narrow range in sphericity index of patients in the current study. In addition, no relationship was found with the ejection fraction, which was close to normal in all patients. Consequently, a possible impact of a restrictive LV remains to be investigated.

3.4.3 Clinical Implications

During AVSD correction, the common atrioventricular valve is separated and the cleft is closed. During surgical correction of an AVSD, surgeons have to minimize valve regurgitation, without causing valve restriction. Even though the shape of the vortex will not be the main concern of the surgeon during correction of an AVSD, awareness of the effect of valve surgery on the formation of vortices in the LV blood flow is important, as changes in vortex formation might affect blood flow efficiency. Similar consideration accounts for LAVV surgery in other congenital and acquired heart disease.

These results do not preclude the possibility that the aberrant vortex formation is a coping mechanism of the heart and has a favorable effect on cardiac function. However, computational fluid dynamics studies have shown increased energy dissipation in cases with a disturbed LAVV shape and abnormal vortex flow formation [14-16], and reduced efficiency of the heart pump in patients with a higher VFT index [33]. A reversed vortex resulted in an increased energy-dissipation level compared with a normally oriented vortex [15]. Whether the aberrant vortex formation additionally results in clinically relevant changes in flow efficiency in corrected AVSD patients remains to be investigated during long term follow-up of this patient group.

In the current study, global diastolic and systolic functions were within normal ranges; however, vortex ring characteristics were significantly different in patients, compared with healthy subjects. This finding may suggest that vortex formation provides a more sensitive indication of disturbed diastolic function than do conventional functional parameters, and confirms the suggested role of vortex analysis as an early predictor of diastolic dysfunction [34]. In patients with unbalanced AVSD, the inflow direction may play a role in LV growth as well [35]. Analysis of vortex formation in unbalanced AVSDs potentially can contribute to predicting LV growth and decision making for biventricular repair.

The disturbed vortex formation observed at rest may become more pronounced during exercise or pregnancy, when cardiac blood flow increases. Future studies are needed to

analyze flow organization in situations with increased cardiac flow, such as during exercise. Furthermore, disturbed vortex ring formation might influence shear stress, which serves as an epigenetic factor in cardiac remodeling [13]. Therefore, future long-term studies have to reveal if abnormal vortex formation affects energy loss or cardiac pumping efficiency, and/or may serve as an early predictor for poor cardiac outcome [30].

Table 3.4. Quantitative vortex core characteristics, as presented in Figure 3.1, at E-peak and A-peak, in healthy subjects and patients

characteristics	Controls (N=30)	Patients (N=26)	P value
E-peak			
Circumferential	90 ± 26°	70 ± 21°	0.003
Longitudinal	0.19 ± 0.04	0.23 ± 0.07	0.015
Radial	0.26 ± 0.07	0.33 ± 0.08	0.001
Orientation	71 ± 9°	50 ± 20° *	<0.001 *
Circularity Index	0.80 ± 0.08	0.70 ± 0.13	0.002
	Controls (N=27)	Patients (N=19)	
A-peak			
Circumferential	106 ± 27°	80 ± 28°	0.003
Longitudinal	0.15 ± 0.05	0.19 ± 0.05	0.004
Radial	0.20 ± 0.08	0.32 ± 0.14	0.002
Orientation	72 ± 6°	54 ± 21°	0.001
Circularity Index	0.63 (0.59-0.69)	0.60 ± 0.10	0.115

E-peak, Early-peak filling; A-peak, late-peak filling. *Including patients with a nonreversed orientation (N = 23). Inclusion of all patients (n = 26) gives a mean orientation of 58 ± 29; P = .037.

3.4.4 Limitations

Absence or presence of a vortex ring was scored visually; however, a previous study [9] showed that vortex detection can be done with low inter- and intra-observer variation. In the current study, the absence of vortex formation was further confirmed by the significant high VFT, which is in line with previous work. The 4D flow MRI has the disadvantage of having a relatively long scan duration (8-10 minutes), and it is associated with relatively high costs, compared with echocardiography.

Vortex core analysis was limited to the E-peak and A-peak; thus, no data were available on the timing, forming, and disappearance of the vortex cores. Parameters of diastolic and systolic function of patients were all close to normal reference values, which made correlation with clinical parameters difficult. The inflow angle of the LV was measured on a 2-dimensional plane, but was compared with a 3D-determined vortex

orientation. If a vortex ring core was not elliptical, the circularity index was computed by approximating an ellipse around the deformed vortex shape. This approximation may not fully capture or characterize the deformed vortex ring shape.

3.5. Conclusions

Quantitative 3D vortex analysis of early- and late-filling vortex ring formation revealed a disturbed vortex ring formation in patients after correction of an AVSD. This disturbance is characterized by either the absence of a formed vortex ring or alterations in the geometric properties and location of the formed rings. These findings were associated with abnormal LV inflow and morphology of the LAVV in the studied patients. Using 3D analysis, the current in vivo study quantitatively confirms the relationship between LAVV abnormalities and altered vortex ring formation in the LV.

Our findings highlight the close relationship among AVV abnormalities. In addition, they create awareness of the influence of AVV abnormalities and AVV surgery on LV vortex formation. The exact implications of abnormal vortex formation and possible increased energy loss and cardiac remodeling, owing to aberrant vortex formation, need further investigation.

3.6. References

1. Penkoske, P.A., et al., Further observations on the morphology of atrioventricular septal defects. *The Journal of thoracic and cardiovascular surgery*, 1985. 90(4): p. 611-622.
2. Takahashi, K., et al., Quantitative real-time three-dimensional echocardiography provides new insight into the mechanisms of mitral valve regurgitation post-repair of atrioventricular septal defect. *Journal of the American Society of Echocardiography*, 2012. 25(11): p. 1231-1244.
3. Draulans-Noë, H.Y., A.C. Wenink, and J. Quaegebeur, Single papillary muscle ("parachute valve") and double-orifice left ventricle in atrioventricular septal defect convergence of chordal attachment: surgical anatomy and results of surgery. *Pediatric cardiology*, 1990. 11(1): p. 29-35.
4. Ando, M. and Y. Takahashi, Variations of atrioventricular septal defects predisposing to regurgitation and stenosis. *The Annals of thoracic surgery*, 2010. 90(2): p. 614-621.
5. Calkoen, E.E., et al., Characterization and improved quantification of left ventricular inflow using streamline visualization with 4DFlow MRI in healthy controls and patients after atrioventricular septal defect correction. *Journal of Magnetic Resonance Imaging*, 2014.
6. Ginde, S., et al., Long-term Outcomes after Surgical Repair of Complete Atrioventricular Septal Defect. *The Journal of Thoracic and Cardiovascular Surgery*, 2015.
7. Louis, J.D.S., et al., Contemporary outcomes of complete atrioventricular septal defect repair: Analysis of the Society of Thoracic Surgeons Congenital Heart Surgery Database. *The Journal of thoracic and cardiovascular surgery*, 2014. 148(6): p. 2526-2531.
8. Drenthen, W., et al., Cardiac complications relating to pregnancy and recurrence of disease in the offspring of women with atrioventricular septal defects. *European heart journal*, 2005. 26(23): p. 2581-2587.

9. Elbaz, M.S., et al., Vortex flow during early and late left ventricular filling in normal subjects: quantitative characterization using retrospectively-gated 4D flow cardiovascular magnetic resonance and three-dimensional vortex core analysis. *Journal of Cardiovascular Magnetic Resonance*, 2014. 16(1): p. 78.
10. Hong, G.R., et al., Characterization and Quantification of Vortex Flow in the Human Left Ventricle by Contrast Echocardiography Using Vector Particle Image Velocimetry. *Jacc-Cardiovascular Imaging*, 2008. 1(6): p. 705-717.
11. Martinez-Legazpi, P., et al., Contribution of the Diastolic Vortex Ring to Left Ventricular Filling. *Journal of the American College of Cardiology*, 2014. 64(16): p. 1711-1721.
12. Bellhouse, B., Fluid mechanics of a model mitral valve and left ventricle. *Cardiovascular research*, 1972. 6(2): p. 199-210.
13. Pasipoularides, A.R.E.S., Diastolic filling vortex forces and cardiac adaptations: probing the epigenetic nexus. *Hellenic J.Cardiol*, 2012. 53: p. 458-469.
14. Hu, Y., et al., Left ventricular vortex under mitral valve edge-to-edge repair. *Cardiovascular engineering and technology*, 2010. 1(4): p. 235-243.
15. Pedrizzetti, G., F. Domenichini, and G. Tonti, On the left ventricular vortex reversal after mitral valve replacement. *Annals of biomedical engineering*, 2010. 38(3): p. 769-773.
16. Kheradvar, A. and A. Falahatpisheh, The effects of dynamic saddle annulus and leaflet length on transmitral flow pattern and leaflet stress of a bileaflet bioprosthetic mitral valve. *Journal of Heart Valve Disease*, 2012. 21(2): p. 225.
17. Faludi, R., et al., Left ventricular flow patterns in healthy subjects and patients with prosthetic mitral valves: an in vivo study using echocardiographic particle image velocimetry. *The Journal of thoracic and cardiovascular surgery*, 2010. 139(6): p. 1501-1510.
18. Hoohenkerk, G.J., et al., More than 30 years' experience with surgical correction of atrioventricular septal defects. *The Annals of thoracic surgery*, 2010. 90(5): p. 1554-1561.
19. Calkoen, E.E., et al., Characterization and quantification of dynamic eccentric regurgitation of the left atrioventricular valve after atrioventricular septal defect correction with 4D Flow cardiovascular magnetic resonance and retrospective valve tracking. *Journal of Cardiovascular Magnetic Resonance*, 2015. 17(1): p. 18.
20. Jeong, J. and F. Hussain, On the identification of a vortex. *Journal of fluid mechanics*, 1995. 285: p. 69-94.
21. Westenberg, J.J., et al., Mitral Valve and Tricuspid Valve Blood Flow: Accurate Quantification with 3D Velocity-encoded MR Imaging with Retrospective Valve Tracking I. *Radiology*, 2008. 249(3): p. 792-800.
22. Gharib, M., et al., Optimal vortex formation as an index of cardiac health. *Proceedings of the National Academy of Sciences*, 2006. 103(16): p. 6305-6308.
23. Kheradvar, A., et al., Assessment of transmitral vortex formation in patients with diastolic dysfunction. *Journal of the American Society of Echocardiography*, 2012. 25(2): p. 220-227.
24. Jiang, S., et al., Effects of suture position on left ventricular fluid mechanics under mitral valve edge-to-edge repair. *Bio-medical materials and engineering*, 2013. 24(1): p. 155-161.
25. Töger, J., et al., Vortex ring formation in the left ventricle of the heart: analysis by 4D flow MRI and Lagrangian coherent structures. *Annals of biomedical engineering*, 2012. 40(12): p. 2652-2662.
26. Dabiri, J.O. and M. Gharib, The role of optimal vortex formation in biological fluid transport. *Proceedings of the Royal Society of London B: Biological Sciences*, 2005. 272(1572): p. 1557-1560.
27. Kheradvar, A. and G. Pedrizzetti, Vortex formation in the cardiovascular system. 2012, Springer. p. 45-79.
28. Paelinck, B.P., et al., Feasibility of tissue magnetic resonance imaging: a pilot study in comparison with tissue Doppler imaging and invasive measurement. *Journal of the American College of Cardiology*, 2005. 45(7): p. 1109-1116.
29. Kilner, P.J., et al., Asymmetric redirection of flow through the heart. *Nature*, 2000. 404(6779): p. 759-761.

30. Sengupta, P.P., J. Narula, and Y. Chandrashekhara, The Dynamic Vortex of a Beating Heart Wring Out the Old and Ring in the New! *Journal of the American College of Cardiology*, 2014. 64(16): p. 1722-1724.
31. Mächler, H., et al., Influence of a tilting prosthetic mitral valve orientation on the left ventricular flow—an experimental in vivo magnetic resonance imaging study. *European journal of cardio-thoracic surgery*, 2007. 32(1): p. 102-107.
32. Bermejo, J., et al., Intraventricular vortex properties in nonischemic dilated cardiomyopathy. *American Journal of Physiology-Heart and Circulatory Physiology*, 2014. 306(5): p. H718-H729.
33. Jiamsripong, P., et al., Impact of Acute Moderate Elevation in Left Ventricular Afterload on Diastolic Transmitral Flow Efficiency: Analysis by Vortex Formation Time. *Journal of the American Society of Echocardiography*, 2009. 22(4): p. 427-431.
34. Pedrizzetti, G., et al., The vortex-an early predictor of cardiovascular outcome? *Nature Reviews Cardiology*, 2014. 11(9): p. 545-553.
35. Overman, D.M., et al. Unbalanced Atrioventricular Septal Defect: Defining the Limits of Biventricular Repair. in *Seminars in Thoracic and Cardiovascular Surgery: Pediatric Cardiac Surgery Annual*. 2013. Elsevier.

Chapter 4

Assessment of viscous energy loss and the association with 3D vortex ring formation in left ventricular inflow: in vivo evaluation using 4DFlow MRI

This chapter was adapted from:

Elbaz, M. S., van der Geest, R. J., Calkoen, E. E., de Roos, A., Lelieveldt, B. P., Roest, A. A., & Westenberg, J. J. (2016). **Assessment of viscous energy loss and the association with three-dimensional vortex ring formation in left ventricular inflow: In vivo evaluation using four-dimensional flow MRI.** *Magnetic Resonance in Medicine*.

(in press): DOI 10.1002/mrm.26129

Abstract

Purpose: To evaluate viscous energy loss and the association with 3D vortex ring formation in left ventricular (LV) blood flow during diastolic filling.

Methods: Thirty healthy volunteers were compared with thirty-two patients with corrected atrioventricular septal defect as unnatural mitral valve morphology and inflow are common in these patients. 4DFlow MRI was acquired from which 3D vortex ring formation was identified in LV blood flow at peak early (E)-filling and late (A)-filling and characterized by its presence/absence, orientation and position from lateral wall. Viscous energy loss was computed over E-, A-filling and complete diastole using the Navier-Stokes energy equations.

Results: Compared to healthy volunteers, viscous energy loss was significantly elevated in patients with disturbed vortex ring formation as characterized by a significantly inclined orientation and/or position closer to the lateral wall. Highest viscous energy loss was found in patients without a ring-shaped vortex during E-filling (on average more than double compared to patients with ring-shape vortex, $p < 0.003$). Altered A-filling vortex ring formation was associated with significant increase in total viscous energy loss over diastole even in the presence of normal E-filling vortex ring.

Conclusion: Altered vortex ring formation during LV filling is associated with increased viscous energy loss.

4.1. Introduction

Evaluation of vortex ring formation in left ventricular (LV) blood flow during diastolic filling has recently emerged as a potential novel approach for characterization of LV blood flow efficiency and cardiac chamber (dys-)function[1-5]. A vortex is characterized by a flow pattern with compact vorticity (the curl of velocity). During LV filling, vortical flow is organized in a ring-like shape enclosing the inflow jet. During both LV filling phases, a vortex ring is formed in the shear layer at the distal tip of the mitral valve (MV) leaflets [6], eventually pinches off from these leaflets and propagates towards the apex. While propagating, the vortex ring dissipates in the bulk flow due to viscosity-driven friction between the vortex ring and the lateral LV wall [7].

Vortical flow in the LV cavity is thought to preserve momentum and kinetic energy in intra-LV blood flow and to help redirecting mitral inflow towards the aortic valve and therefore, minimizing the LV mechanical energy needed to eject the blood during systole [2, 6, 8]. Viscous dissipation of the vortex ring may contribute to or attenuate this flow organization [8, 9]. Viscous energy dissipation/loss is essentially kinetic energy converted into thermal energy due to viscosity-driven friction [10]. Consequently, in healthy hearts the viscous energy loss is proportional to the amount of kinetic energy produced in the flow which is in turn proportional to the amount of the inflow, i.e., the stroke volume [10].

The normal dissipation of the vortex ring in the LV is mainly driven by the asymmetric shape of MV leaflets and the annulus position [3, 7]. The MV setup is found to be optimal for minimizing viscous kinetic energy loss in LV blood flow [8, 9]. Using an idealized LV model, computational fluid dynamics (CFD) studies have shown that a breakup in the natural MV setup, by either displacing the annulus closer to the lateral wall [8] or changing the natural MV asymmetry [9], can alter the formed vortex ring orientation and/or position relative to the lateral wall. Such unnatural vortex ring formation is found to be associated with an increase in viscous energy loss during LV filling which then may require more mechanical energy from the LV to preserve the cardiac output during systole [3, 8, 9]. However, it has not been shown that a similar association between 3D vortex ring formation and viscous energy loss during LV filling is present in vivo.

Patients after atrioventricular septal defect (AVSD) correction are exemplary to have an unnatural MV/left atrioventricular valve (LAVV) setup with a more laterally positioned annulus and a smaller posterior leaflet compared to normal hearts [11-13]. This setup has shown to result in altered 3D vortex ring formation characterized by a more lateral position, more inclined orientation and more frequent absence of vortex ring formation

compared to healthy controls [14]. Moreover, the inflow jet was found to be directed towards the lateral wall in these patients [15]. Nevertheless, it is currently unclear whether these disturbed vortex ring parameters would correspond with different levels of viscous energy loss during LV filling in these patients compared to healthy volunteers.

Recently, 4DFlow MRI (also known as three-directional, three-dimensional (3D) and time-resolved velocity-encoded MRI) has enabled quantitative 3D vortex ring analysis during both early and late LV filling in healthy volunteers and patients including measurements of vortex ring orientation and radial position (i.e. distance from lateral wall) [14, 16, 17]. Given the role of natural vortex ring formation in minimization of viscous energy loss, previously reported in in vitro studies [8, 9], we hypothesized that disturbed vortex ring formation in patients would be associated with increased viscous energy loss in LV blood flow due to increased friction with the lateral wall. Therefore, the aim of this study was to employ 4DFlow MRI to evaluate viscous energy loss and assess the association with 3D vortex ring formation during LV filling in vivo in healthy volunteers and patients with altered vortex flow.

4.2. Theory

Mechanical energy can be described as the ability to move the mass of an object over some distance. In case of idealized flow in which no frictional forces are present, the total mechanical energy in the system (i.e., circulatory system) is conserved [10]. This means that any increase in potential energy (i.e., pressure) will be compensated by a decrease in kinetic energy and vice versa and the exchange of energy occurs without energy loss. In the LV, the blood flow is non-idealized and with blood being a viscous fluid, frictional forces exist resulting in irreversible mechanical energy loss mainly in the form of thermal energy (heat) [10]. Viscous energy loss corresponds to the mechanical kinetic energy irreversibly lost (converted) to thermal energy due to frictional forces induced by fluid viscosity and *no-slip* condition [10, 18].

4DFlow MRI can provide the three-directional velocity flow field \mathbf{v} over the three principal directions x , y , z and over the complete cardiac cycle [19]. Given the acquired velocity field \mathbf{v} , the instantaneous rate of viscous energy loss ($\dot{E}L$) in watt (W) and the total energy loss (EL_{total}) in joule (J) over a given period of time T can be computed using the viscous dissipation function Φ_v in the Newtonian Navier-Stokes energy equations [20-22]:

$$\Phi_v = \frac{1}{2} \sum_{i=1}^3 \sum_{j=1}^3 \left[\left(\frac{\partial v_i}{\partial x_j} + \frac{\partial v_j}{\partial x_i} \right) - \frac{2}{3} (\nabla \cdot \mathbf{v}) \delta_{ij} \right]^2, \begin{cases} \delta_{ij} = \mathbf{1}, \text{ if } i = j \\ \delta_{ij} = \mathbf{0}, \text{ if } i \neq j \end{cases} \quad [\text{s}^{-2}] \quad (1)$$

The viscous dissipation function Φ_v represents the rate of viscous energy dissipation per unit volume. i, j correspond to the principal velocity directions x, y, z . $\nabla \cdot v$ is the divergence of the velocity field. Hence, the volumetric rate of viscous energy loss ($\dot{E}L$) in watt at time instance t can be computed as:

$$\dot{E}L_t = \mu \sum_{w=1}^N \Phi_v L_w \quad [\text{watt (W)}] \quad (2)$$

with the dynamic viscosity $\mu=0.004$ Pa·s, assuming the blood as a Newtonian fluid, N as the total number of voxels in the given domain of interest (e.g. LV), L_w as the voxel volume.

Consequently, the total viscous energy loss (EL) in joules over time period T starting at phase t_{start} and ending at t_{end} can be computed as:

$$EL_T = \sum_{d=t_{\text{start}}}^{t_{\text{end}}} \dot{E}L_d p_d \quad [\text{joule (J)}] \quad (3)$$

with p_d the time step (temporal resolution) of the 4DFlow MRI acquisition.

Given the three-directional velocity vector field v , the kinetic energy (KE) over a domain of interest with N voxels of volume L at time instance t can be computed as

$$KE_t = \frac{\rho}{2} \sum_{k=1}^N \|v_k\|^2 L_k \quad [\text{J}] \quad (4)$$

with blood assumed as incompressible fluid with density $\rho= 1,025$ kg/m³.

4.3. Methods

4.3.1. Study population

The study was approved by the local ethical committee and written informed consent was obtained from all participants or their parents. Thirty-two patients with a history of corrected-AVSD were prospectively enrolled [23]. Thirty controls with a similar age and without history of cardiac disease were included for comparison. Patients underwent electrocardiography and ECG and their details were analyzed. All patients were in sinus rhythm. Forty-four percent of the patients presented with a right bundle branch block and six (19%) with some form of left bundle branch block. Data from patients and/or controls was previously reported in studies with the aim to characterize and quantify diastolic trans-atrioventricular valve flow [15, 24], providing reference values for 3D vortex flow in the LV [16] and evaluating LV inflow propagation velocity [25]. Two more recent publications have used the 4D flow MRI data to evaluate the intracardiac blood flow organization in the same populations of corrected AVSD patients and healthy controls [17, 26] and to evaluate vortex ring formation in patients after AVSD-repair [17]. However, none of these publica-

tions reported viscous energy loss, kinetic energy or its association with vortex ring parameters. For clarity, the term mitral valve (MV) will be used in both healthy subjects and patients (instead of LAVV).

4.3.2. 4DFlow MRI protocol and data preparation

Whole-heart 4DFlow MRI was obtained on a 3T MRI scanner (Ingenia 3T MRI with Software Stream 4.1.3.0, Philips Healthcare, Best, The Netherlands), using a combination of FlexCoverage Posterior coil in the table top with a dStream Torso coil, providing up to 32 coil elements for signal reception. Velocity encoding of 150cm/s was used in all three directions, with spatial resolution $2.3 \times 2.3 \times 3.0$ – 4.2mm^3 , flip angle 10° , echo time (TE) 3.2ms and repetition time (TR) 7.7ms, resulting in a maximal true temporal resolution of $4 \times \text{TR} = 31 \text{ms}$. Retrospective ECG-gating was used and 30 cardiac phases were reconstructed to represent one average heartbeat. Parallel imaging was performed using SENSE with factor 2 and echo planar imaging with factor 5 for acquisition acceleration. Furthermore, to quantify LV volumes and ejection fraction as well as facilitating LV segmentation, a left two-chamber and four-chamber cine view and a short-axis cine stack of slices were acquired with steady-state free-precession with TE/TR 1.5/3.0; 8mm section thickness; 45° flip angle; spatial resolution $1.0 \times 1.0 \times 8.0 \text{mm}^3$; three signal averages and parallel imaging with SENSE factor 2. Typical volume for a whole-heart 4DFlow MRI acquisition was 396 mm (right-left) \times 336 mm (anterior-posterior) \times 117 mm (feet-head). However, the field-of-view in anterior-posterior direction was adapted to the size of each subject. 4DFlow MRI acquisition took on average 8 minutes (range 5-12 minutes). Concomitant gradient correction and local phase correction were applied using the software available on the MRI system.

To enable a reasonable acquisition time (8-10 minutes), free breathing was allowed for both patients as well as controls, without using motion compensation techniques such as navigators. For each voxel, 4D flow MRI data was obtained in retrospectively gated time-resolved manner, using one velocity-compensated and three velocity-sensitive (in three orthogonal directions) recordings. No additional signal averaging was performed. For short-axis cine data, three signal averages were obtained to compensate for breathing motion.

Using in-house developed MASS software (Leiden University Medical Center), the LV endocardial contours were manually traced on short-axis slices over all acquired phases. Contours were then projected on the whole-heart 4DFlow data. To reduce possible

translation errors between cine short-axis and whole-heart 4DFlow acquisitions, automated image registration using Elastix [27] was performed between cine short-axis data and velocity magnitude reconstructed images of the 4DFlow data using a single phase that visually showed the best depiction of the LV in the velocity magnitude 4DFlow image. Registration was restricted to translation only. This registration result was then propagated to all 4DFlow phases. Registered 4DFlow MRI contours were then visually reviewed for any possible registration or projection errors and manually corrected whenever needed. The 3D velocity data within the segmented LV volume was then used to compute energy parameters as described in the Theory section. Segmented LV endocardial boundaries were also used to compute the LV end-diastolic volume (EDV), end-systolic volume (ESV), stroke volume (SV) and ejection fraction. Cardiac output (CO) was computed as $CO = (SV \times HR)$ with HR as the heart rate.

LV inflow was quantified from 4DFlow MRI data using retrospective mitral valve tracking [28]. The time points corresponding to peak early filling (E-peak) and peak late filling (A-peak) were defined from the flow-time curves which resulted from velocity mapping as previously described [15, 24]. E/A ratio was computed from flow rate values at E-peak and A-peak. To study the association with diastolic vortex formation, the inflow area and peak velocity during E-peak were quantified at the level of peak inflow velocity as previously described [15].

Image analysis was performed by one observer (EC) with two years of experience in cardiac MRI and verified by one observer (JW) with over 15 years of experience.

4.3.3. 3D vortex core identification using the Lambda2 (λ_2)-method

Using the previously validated 3D vortex analysis workflow [16], the 3D vortex cores within the segmented LV blood pool were identified from the 4DFlow MRI data at both LV filling phases using the Lambda2-method and visualized as 3D isosurfaces [29]. In short, the Lambda2-method is a well-established fluid-dynamics-based method that uses the gradient properties of the velocity field to generate a 3D scalar (λ_2) field. The λ_2 -field implicitly describes the fluid pressure at each voxel. Voxels with extreme negative values, i.e. below a predefined λ_2 threshold are labeled as part of a vortex core in the flow. Vortex cores are then visualized as isosurfaces of some negative λ_2 threshold. In this work, the threshold was defined using a previously validated interactive method [16]. Qualitative visual inspection of the shape of detected 3D vortex core isosurfaces were performed by a single observer (ME) to determine whether a ring-shaped vortex core (a vortex core with a

donut-like (torus) shape enclosing the inflow jet) was present. If such vortex ring core was detected during E-filling and/or A-filling, its normalized radial position and orientation relative to the LV long-axis were calculated as described previously [16] (Figure 4.1).

4.3.4. Vortex formation time (VFT) index

The Vortex Formation Time (VFT), a dimensionless index previously proposed to quantify the process of vortex progression during early filling [30], was determined as follows:

$$VFT = \frac{V_{avg} \times E_{duration}}{D} \quad (5)$$

with V_{avg} as the average speed of the blood flow during E-filling, $E_{duration}$ as the duration of E-filling and D as the maximum diameter of the MV opening. D was computed at E-peak from the area of the MV flow on retrospective valve tracking at peak inflow velocity level (i.e., approximately at the tip of the valves), using $D = 2\sqrt{Area/\pi}$, assuming a circular inflow area.

4.3.5. Energy Analysis

To quantify viscous energy loss in the LV during diastolic filling, the instantaneous volumetric rate of viscous energy loss ($\dot{E}L$) was computed for each time point during LV filling using Equation (2). To quantify the viscous energy loss over both E- and A-filling phases, the average rate of viscous energy loss over both periods ($\dot{E}L_{E-avg}$) and ($\dot{E}L_{A-avg}$) was computed. The average viscous energy loss rate was used instead of the total viscous energy loss to account for the variation in E- and A-filling durations among different subjects. The peaks $\dot{E}L$ during E-filling ($\dot{E}L_{E-peak}$) and A-filling ($\dot{E}L_{A-peak}$) were calculated as well as the ratio $\dot{E}L_{E-peak} / \dot{E}L_{A-peak}$, reported as $\dot{E}L_{E/A}$.

The total viscous energy loss over diastole ($EL_{diastole}$) was computed using Equation (3). To account for the variation in inflow volumes between different subjects, all computed viscous energy loss measurements were normalized by stroke volume (SV). This resulted in viscous energy loss measurements per unit volume EL (in J/m^3) and the rate of viscous energy loss $\dot{E}L$ per unit volume (in W/m^3). To compare with previously reported studies on viscous energy loss based on other modalities [31, 32], the absolute (i.e. not SV normalized) $EL_{diastole}$ is also reported as $abs_EL_{diastole}$.

To quantify the change of kinetic energy (KE) over the period of LV filling, the instantaneous volumetric KE was quantified at each time point during LV filling (defined

from the flow-time curve) using Equation (4). The average KE over E-filling (KE_{E-avg}) and A-filling (KE_{A-avg}) was computed. Also peak KE over E-filling (KE_{E-peak}) and A-filling (KE_{A-peak}) was calculated.

The amount of KE is proportional to the amount of LV inflow volume. Similar to EL, all computed KE were normalized by SV resulting in KE per unit volume (in J/m^3) to account for the variation in inflow volumes among subjects. To compare with previously reported KE [33], the absolute (i.e. not SV normalized) KE_{E-peak} and KE_{A-peak} are also reported as abs_KE_{E-peak} and abs_KE_{A-peak} .

Energy analysis was performed with an in-house software module developed using MATLAB (MathWorks Inc., version R2013b). Time-resolved segmented LV volumes were used in all provided analysis.

4.3.6. Statistical analysis

Data analysis was performed using SPSS Statistics (version 20.0 IBM SPSS, Chicago, Illinois). Variables were tested for normal distribution using the Shapiro-Wilk test. Continuous variables are expressed as mean \pm standard deviation (SD) or as median with inter-quartile range [IQR] where appropriate. Comparison of variables amongst different groups was performed using unpaired Student's t-test or Mann-Whitney U-test where appropriate, and $p < 0.05$ was considered statistically significant.

The normal limits of vortex ring's radial position and orientation were obtained from the 95%CI (confidence interval) in the controls group. For each of the two vortex parameters, the patients were divided into three groups; patients with data within, below or above 95%CI of controls. One additional group was constructed which included patients with a normal vortex ring, i.e., both radial position and orientation within 95%CI normal limits. For each group, the values of aforementioned parameters of $\dot{E}L$ and EL were compared with corresponding values in controls using Mann-Whitney U-test.

Correlations of $\dot{E}L_{E-avg}$ with KE_{E-avg} , $\dot{E}L_{A-avg}$ with KE_{A-avg} , stroke volume with $abs_EL_{diastole}$, ejection fraction with $abs_EL_{diastole}$, VFT with $EL_{diastole}$, $\dot{E}L_{E/A}$ with inflow E/A and $EL_{diastole}$ with HR were assessed from linear regression analysis (Pearson's R^2).

4.4. Results

4.4.1. Clinical characteristics

Clinical characteristics of the studied subjects are summarized in Table 4.1.

4.4.2. LV viscous energy loss (EL) over diastole

Detailed results are listed in Table 4.2. In all controls, the timing of the peaks in viscous energy loss rate $\dot{E}L$ over diastole appeared in good alignment with the peaks in the flow rate-time curves (one example shown in Figure 4.2a). Two distinct peaks of viscous energy loss (EL) during diastole were discriminated: the first during early filling and the second during late filling. The peak E-filling viscous energy loss was significantly higher than A-peak ($\dot{E}L_{E\text{-peak}} = 14.7 \pm 4.6 \text{ W/m}^3$, $\dot{E}L_{A\text{-peak}} = 5.1 \pm 2.8 \text{ W/m}^3$, $p < 0.001$). The ratio between the EL peaks $\dot{E}L_{E/A}$ was 3.4 ± 1.6 . The normal limits of 95%CI of EL_{diastole} were $[1.97\text{--}4.92 \text{ J/m}^3]$.

Table 4.1. Characteristics of healthy controls and corrected-AVSD patients

	Controls	Corrected-AVSD patients
Age (years)	23 [13–38]	26 ± 12
Male (%)	14 (46)	9 (28)
Heart rate (bpm)	68 [60–78]	76 ± 13
Diastasis (ms)	116 ± 89	26 [0–67] * †
Stroke volume (mL)	89 ± 23	85 ± 19
Cardiac output (L/min)	6.01 ± 1.3	6.39 ± 1.4
EDV (mL)	146 ± 42	155 ± 33
Early filling fraction (%)	76 ± 5	73 ± 13
Ejection fraction (%)	61 ± 5	56 [52–58] ‡
E/A ratio peak flow rate	2.5 ± 0.8	2.1 [1.7–2.6] *
VFT index	2.6 ± 0.6 (N=30)	2.4 [1.9–3.1] (N=32)

EDV = end-diastolic volume, VFT = vortex formation time, * excluding two cases without A-peak, † indicates $p < 0.01$, ‡ indicates $p < 0.001$. Normally distributed data is presented as mean ± SD while non-normally distributed data is presented as median [Interquartile Range].

In patients, similar to controls, two peaks could be detected in $\dot{E}L$ during diastole in good alignment with the peaks in the flow rate-time curves (Figure 4.2b). The $\dot{E}L_{E\text{-peak}}$ was significantly higher than in controls (patients $\dot{E}L_{E\text{-peak}} = 18.3 [13.9\text{--}28.6] \text{ W/m}^3$, $p = 0.002$). Similarly, the peak of energy loss rate during A-filling in patients was

significantly increased compared to controls (patients $\dot{E}L_{A\text{-peak}} = 10.4 \pm 5.3 \text{ W/m}^3$, $p < 0.001$). Furthermore, the E/A ratio between $\dot{E}L$ peaks was significantly reduced in patients compared to controls (patients $\dot{E}L_{E/A} = 1.9$ [1.3–2.9], $p = 0.003$). In two patients, no A-wave was discriminated and therefore in those cases, no results for A-peak were obtained. Compared to controls, patients showed a significant increase ($p < 0.001$) in viscous energy loss over complete diastole EL_{diastole} .

4.4.3. LV kinetic energy (KE) over diastole and the association with viscous energy loss

Detailed results are listed in Table 4.2. Similar to EL, two peaks $KE_{E\text{-peak}}$ and $KE_{A\text{-peak}}$ of KE could be detected in controls and patients with the timing of these peaks in good alignment with the flow rate-time curves (Figure 4.2). Both $KE_{E\text{-avg}}$ and $KE_{E\text{-peak}}$ were significantly higher ($p = 0.03$) in patients compared to controls. Similarly, both $KE_{A\text{-avg}}$ and $KE_{A\text{-peak}}$ were significantly increased in patients compared to controls ($p < 0.001$).

In controls, strong correlations were found between $KE_{E\text{-avg}}$ and $\dot{E}L_{E\text{-avg}}$ during E-filling ($R^2 = 0.81$) and between $KE_{A\text{-avg}}$ and $\dot{E}L_{A\text{-avg}}$ during A-filling ($R^2 = 0.88$) (Figure 4.3). This was similar for patients where strong correlations were found between $KE_{E\text{-avg}}$ and $\dot{E}L_{E\text{-avg}}$ during E-filling ($R^2 = 0.88$) and between $KE_{A\text{-avg}}$ and $\dot{E}L_{A\text{-avg}}$ during A-filling ($R^2 = 0.88$) (Figure 4.3).

4.4.4. LV vortex ring formation and viscous energy loss

In all controls, a compact vortex ring core was identified in the LV blood flow during E-filling and quantitatively characterized. In 26 patients (81%), a vortex ring core was present but with different characteristics from controls (Table 4.3, Table 4.5). Among these patients, 17 (65%) patients had significantly tilted vortex ring orientation beyond the 95%CI of controls' vortex orientation (Table 4.4): in 14 patients below the lower limit and in 3 patients above the upper limit of the 95%CI of controls. Compared to controls, patients with E-peak vortex ring orientation within the normal limits ($N = 9$) presented with non-significantly different E-filling viscous energy loss rate $\dot{E}L_{E\text{-avg}}$ but showed significantly higher $\dot{E}L_{A\text{-avg}}$ ($p < 0.01$) and EL_{diastole} ($p = 0.04$) (Table 4.5). Patients with E-peak vortex ring orientation beyond normal limits ($N = 17$) presented significantly increased viscous energy loss during E-filling, A-filling and complete diastole ($p < 0.01$). Detailed results are

listed in Table 4.5. In eight patients with both radial position and orientation of E-peak vortex ring within the normal limits, $\dot{E}L_{E-avg}$ was not significantly different from controls but $EL_{diastole}$ was still different from controls ($p < 0.01$). Patients with E-peak vortex ring positioned significantly more lateral (radial position $> 95\%CI$), showed a significant increase in viscous energy loss during E-filling, A-filling and over complete diastole.

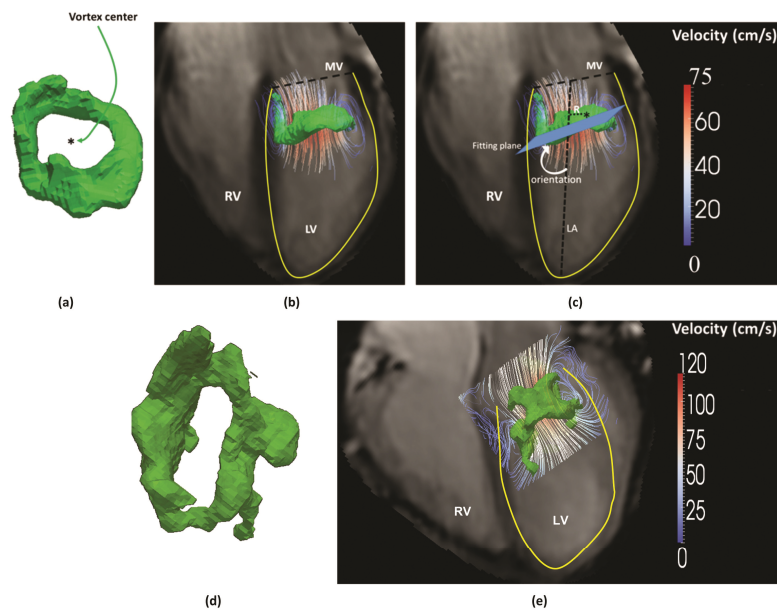


Figure 4.1. (a) Example of vortex ring isosurface (in green) at E-peak filling phase as identified using Lambda2-based vortex core detection (16) from a healthy volunteer (b) Streamlines superimposed on vortex ring isosurface (a) in a four-chamber view. (c) Definition of vortex ring orientation and normalized radial position relative to the LV long-axis: The LV long-axis is defined as the line from the mid of the mitral valvular opening to the LV apex. The normalized radial position was calculated as the distance of the vortex ring center (marked by ‘*’) to the LV long-axis normalized by the basal endocardial radius. Vortex ring orientation was measured as the angle between the fitting plane of the vortex ring isosurface and the LV long-axis (LA). (d) Example vortex ring isosurface (in light green) at E-peak filling phase from an AVSD-repaired patient with an inclined E-peak vortex ring orientation, showing a more elliptical vortex ring compared to controls. This deviated shape can be due to the restricted valve opening known to occur in AVSD patients after repair (17). (e) Streamlines superimposed on vortex ring isosurface presented in (d) showing the inclined inflow and vortex ring orientation in this patient in a four-chamber view.

Table 4.2. Quantitative analysis of viscous energy loss and kinetic energy during LV filling

	Controls (N=30)	Patients (N=32)	p-value
$\dot{E}L_{E-avg}$ (W/m ³)	6.6 [5.5–9.0]	12.2±7.2	<0.001
$\dot{E}L_{A-avg}$ (W/m ³)	3.9±2.2	8.1±3.8*	<0.001
$\dot{E}L_{E-peak}$ (W/m ³)	14.7±4.6	18.3 [13.9–28.6]	0.002
$\dot{E}L_{A-peak}$ (W/m ³)	5.1±2.8	10.4±5.3*	<0.001
$\dot{E}L_{E/A}$	3.4±1.6	1.9 [1.3–2.9]*	0.003
$EL_{diastole}$ (J/m ³)	2.7 [2.3–3.2]	4.9±2.0	<0.001
abs_ $EL_{diastole}$ (mJ)	0.24 [0.19–0.28]	0.37 [0.26–0.53]	<0.001
KE_{E-avg} (J/m ³)	25.1±7.8	34.1±18.8	0.03
KE_{A-avg} (J/m ³)*	9.3 [7.0–13.2]	21.4±11.2*	<0.001
KE_{E-peak} (J/m ³)	57.2±16.6	55.2 [46.4–76.5]	0.65
KE_{A-peak} (J/m ³)*	15.9±8.0	28.9±16.0*	<0.001
abs_ KE_{E-peak} (mJ)	5.0±1.9	5.5±2.7	0.73
abs_ KE_{A-peak} (mJ)*	1.3±0.5	2.26 [1.3–3.2]*	<0.001

*Two patients had no A-wave and were excluded.

In the remaining six patients (19%), no well-formed E-peak vortex ring core was detected but rather a complex flow with isolated vortex cores of irregular shape. These patients showed a significant increase in viscous energy loss over complete diastole ($EL_{diastole}$) compared to controls ($p<0.01$) as well as compared to the other patients ($p=0.002$) (Figure 4.2b, Table 4.4). Moreover, these patients presented significant increase in energy loss rate during E-filling ($\dot{E}L_{E-avg}$) compared to controls ($p<0.01$). Five out of these six patients showed EL per unit volume above the 95% CI [1.97–4.92 J/m³] of controls (Figure 4.4). In addition, these five patients showed significantly higher vortex formation time (VFT) compared to controls (VFT (six patients without E-vortex ring) = 6.4±1.3 versus VFT (controls) = 2.6 ±0.6, $p=0.002$) and compared to other patients (VFT (twenty-six patients with E-vortex ring)=2.4±0.6, $p=0.002$). The one remaining patient with no E-peak vortex ring presented with an abnormal valve anatomy with double orifice for which it was not feasible to determine the orifice diameter D (in Equation (5)). In controls, the values for VFT presented with a narrow range, therefore, low correlation was found between $EL_{diastole}$ and VFT ($R^2=0.03$, $p=0.35$) (Figure 4.5). However, in patients, with a wider range for VFT, this parameter showed good correlation with $EL_{diastole}$ ($R^2=0.864$, $p<0.001$) (Figure 4.5).

Table 4.3. Quantitative energy parameters in patients presented with vortex ring core vs. those without vortex ring.

	Patients with vortex ring (E-filling: N=26, A- filling: N=19)	Patients without vortex ring (E-filling: N=6, A- filling: N=13)	p-value
$\dot{E}L_{E-avg}$ (W/m ³)	9.3 [7.5–12.4] ^b	21.0±11.6 ^b	0.003
$\dot{E}L_{A-avg}$ (W/m ³)*	1.6±1.1 ^a	2.2±0.9 ^{b*}	0.04
$\dot{E}L_{E-peak}$ (W/m ³)	17 [13.8–22.5] ^a	41.8±20.0 ^b	0.001
$\dot{E}L_{A-peak}$ (W/m ³)*	9.4 [6–13.3] ^b	12.1±5.5 ^{b*}	0.16
$EL_{diastole}$ (J/m ³)	4.2±1.3 ^b	7.60±2.2 ^b	0.005
KE_{E-avg} (J/m ³)	26.8 [22.8–34.9] ^{NS}	54.4±31.8 ^b	0.03
KE_{A-avg} (J/m ³)*	19.0±11.4 ^a	25.5±10.1 ^{b*}	0.13
KE_{E-peak} (J/m ³)	57.8±0.2 ^{NS}	101.6±59.2 ^a	0.05
KE_{A-peak} (J/m ³)*	24.9 [16.0–40.8] ^a	34.5±16.2 ^{b*}	0.07

^{NS} p>0.05 compared to controls ^a p<0.05 compared to controls ^b p<0.01 compared to controls. *Two patients had no A-wave and were excluded.

In 27 (90%) controls, a vortex ring core was identified during late filling. In the remaining three controls with no identified A-filling vortex ring, a short or no diastasis was observed [16]. During A-filling, a vortex ring core was identified in 19 patients (59%). In the other 13 patients (41%), only irregular isolated vortex cores were present. Although $\dot{E}L_{A-avg}$ was significantly increased in patients with absent A-peak vortex ring compared to controls, it was not significantly different from the other patients who presented with A-peak vortex ring. Detailed results are presented in Table 4.3 and Table 3.5.

During A-filling, patients with A-peak vortex ring orientation and/or radial position within the normal limits still presented significant increase in viscous energy loss rate $\dot{E}L_{A-avg}$ (p<0.05) compared to controls. These patients showed significant increase in the corresponding E-filling energy loss rate ($\dot{E}L_{E-avg}$) with p<0.01. There was no significant difference of $\dot{E}L_{E-avg}$ between patients with significantly laterally positioned A-peak vortex ring and those within 95%CI.

Only three patients had both E-peak and A-peak vortex rings with orientation and radial position within normal limits. Compared to controls, these patients presented comparable viscous energy loss of $\dot{E}L_{E-avg}$ (p=0.5), $\dot{E}L_{A-avg}$ (p=0.2) and $EL_{diastole}$ (p=0.3).

4.4.5. Association between viscous energy loss with global functional parameters

No correlation was found between ejection fraction and $\text{abs_EL}_{\text{diastole}}$ in controls ($R^2=0.04$, $p=0.31$) or patients ($R^2=0.001$, $p=0.7$). Good correlation was found between $\text{abs_EL}_{\text{diastole}}$ and stroke volume in controls ($R^2=0.56$, $p<0.001$). This correlation was moderate in patients ($R^2=0.32$, $p=0.001$) (Figure 4.5). E/A ratio showed moderate correlation with $\text{EL}_{\text{E/A}}$ in both controls ($R^2=0.31$, $p=0.001$) and patients ($R^2=0.36$, $p=0.001$). No correlation was found between $\text{EL}_{\text{diastole}}$ and HR in controls ($R^2=0.008$, $p=0.97$) or patients ($R^2=0.11$, $p=0.55$).

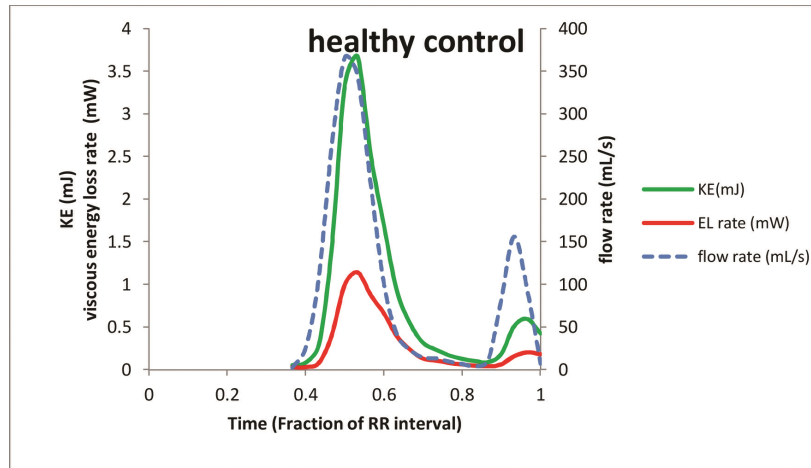
Table 4.4. Controls' vortex ring parameters and normal limits

Phase	Vortex ring parameter	95%CI range		N (total=30)	N _{outside}
		Lower limit (2.5%)	Upper limit (97.5%)		
E-filling peak	Orientation	55°	87°	28	2
	Normalized Radial Position	0.14	0.39	28	2
A-filling peak*	Orientation	57 °	84 °	25	2
	Normalized Radial Position	0.05	0.39	25	2

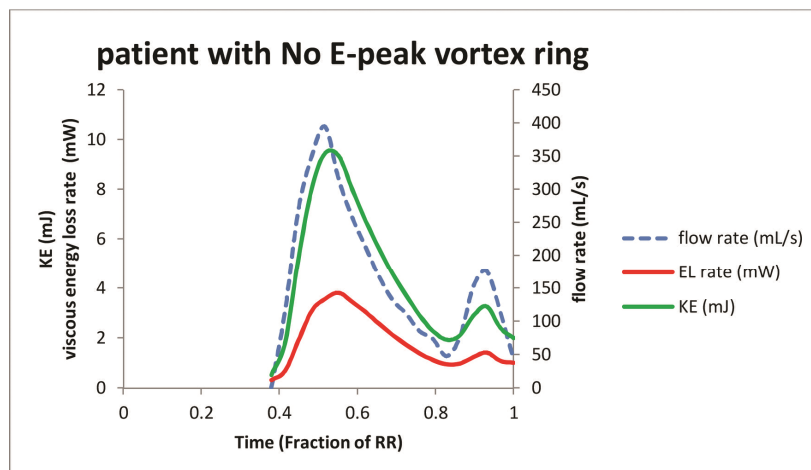
95% Confidence Interval (CI) represents the interval [2.5%–97.5%]. N is the number of subjects that presented a vortex ring core within the 95%CI range. N_{outside} is the number of subjects with detected vortex ring core but outside the 95%CI range. Radial position is normalized to the basal endocardial radius (measured on a short-axis slice). * three subjects did not present vortex ring core at peak late filling.

4.5. Discussion

The present study quantitatively evaluates the viscous energy loss during LV filling in healthy volunteers and patients with altered 3D vortex ring formation (corrected-AVSD patients) in LV blood flow by means of 4DFlow MRI. The main finding of this study is that viscous energy loss during LV filling is significantly elevated in patients with altered diastolic vortex ring parameters characterized by an abnormal orientation and/or position of the vortex ring relative to the lateral wall. The highest viscous energy loss was found in patients who presented without ring-shaped vortex during early filling in combination with a VFT significantly beyond the normal limit.



(a)



(b)

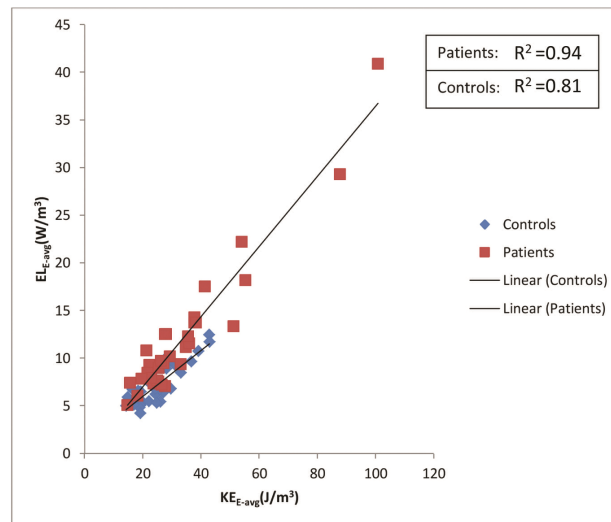
Figure 4.2 Temporal evolution of viscous energy loss rate (\dot{E}_L), kinetic energy (KE) and inflow rate over LV diastole of a) a typical healthy subject b) a patient who did not present E-vortex ring formation but rather a complex irregular flow instead. Viscous energy loss characterized by E- and A-peaks is significantly elevated (with more than two-fold increase) in the patient (b) compared to the healthy control subject (a).

Previous *in vitro* [22] and *in vivo* [20] studies showed the feasibility of MRI-derived viscous energy loss calculation. However, no studies have reported *in vivo* viscous energy loss in 3D (+time) in the LV using 4DFlow MRI and no gold standard currently exists. Nevertheless, the reported quantitative values of viscous energy loss for healthy

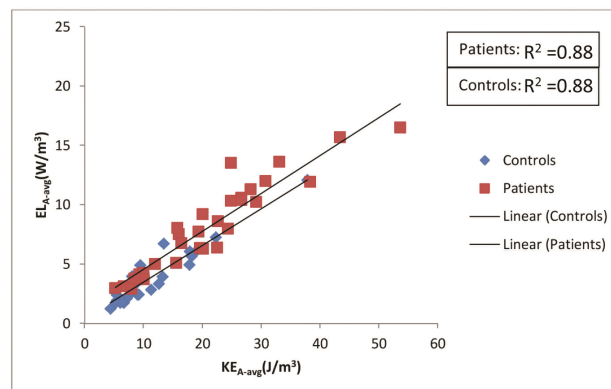
volunteers in this study are in good agreement with those reported in recent in vitro studies. A CFD study using an echo-derived LV model [32] reported a mean total viscous energy loss over diastole from 20 volunteers (age 19 ± 4 years) of 0.17 ± 0.07 mJ. This is in the same order of magnitude of our results ($\text{abs_EL}_{\text{diastole}} = 0.24$ [0.19–0.28] mJ). Similarly, the reported mean viscous energy loss in patients in the current study ($\text{abs_EL}_{\text{diastole}} = 0.37$ [0.26–0.53] mJ) is in good agreement with the calculated in vitro energy loss (0.39 mJ) reported from a CFD simulation in a patient with unnatural mitral valve [31]. Moreover, the appearance of the viscous energy loss-time curves agree with previously reported in vitro results [8, 9]. Likewise, our reported results of kinetic energy in LV blood flow in healthy volunteers for both E-peak ($\text{abs_KE}_{\text{E-peak}} = 5.0 \pm 1.9$ mJ) and A-peak ($\text{abs_KE}_{\text{A-peak}} = 2.26$ [1.3–3.2] mJ) agree well with those reported by Carlsson et al. [33] as 6.0 ± 0.6 mJ and 1.3 ± 0.2 mJ, respectively. Using a time-resolved KE measurements, similar to the current study, Hussaini et al. [34] reported peak KE from 10 healthy volunteers to be 4.90 ± 1.49 mJ which is again in good agreement with our reported results ($\text{abs_KE}_{\text{E-peak}} = 5.0 \pm 1.9$ mJ). Furthermore, the obvious strong correlation found in this study between viscous energy loss and kinetic energy during both early and late filling as well as the good correlation with the stroke volume may further emphasize the feasibility of 4DFlow MRI for in vivo computation of kinetic energy and viscous energy loss in the LV.

During normal LV filling, vortex ring formation in LV blood flow is thought to contribute to organizing the inflow and its kinetic energy by preserving momentum, rearranging flow direction and minimizing collision of flow with the LV wall and therefore, minimizing energy loss [6, 8, 9, 18]. In AVSD patients, the connection between the atria and ventricles is characterized by a common atrioventricular valve [12, 13]. Compared to the normal MV, the LAVV in AVSD hearts is characterized by a smaller posterior leaflet which is positioned more laterally [11-13]. Surgical correction of an AVSD may also result in a restricted opening of the LAVV [35] causing the inflow jet to be directed towards the lateral wall [15]. The abnormal LAVV morphology in corrected-AVSD patients compared to the MV in healthy controls is associated with altered vortex ring orientation and shifted radial position towards the lateral wall [14]. In this study, we demonstrated that these different vortex characteristics are also associated with an increase in viscous energy loss compared to healthy controls. A possible explanation may be that the deformed asymmetry of the MV leaflets in corrected-AVSD patients [11-13] inclines the inflow jet more towards the lateral wall [8, 9, 15]. Consequently, the vortex ring originates with an abnormal orientation during LV filling and propagates towards (instead of along) the lateral wall, eventu-

ally colliding with it. Friction due to vortex-wall interaction increases the viscous dissipation [8]. Also, the shifted position of the vortex ring brings the lateral vortex side in close interaction with the lateral wall.



(a)



(b)

Figure 4.3. Correlation between average viscous energy loss during E-filling (EL_{E-avg}) (a) and late filling (EL_{A-avg}) (b) with corresponding kinetic energy (KE), i.e., KE_{E-avg} and KE_{A-avg} , respectively in controls (blue) and patients (red).

The associations between vortex characteristics and viscous energy loss reported in this study are in agreement with previous studies. Using idealized LV models with a circular mitral annulus and CFD experiments, Pedrizzetti et al. [8] showed that a shift of the annulus towards the lateral wall altered vortex ring formation during diastole which was

associated with elevated viscous energy loss. Furthermore, in vitro experiments [9, 36] showed that a change in the natural MV asymmetry corresponded with altered vortex ring formation and increase in viscous energy loss. Moreover, simulations using an abnormal symmetric prosthetic mitral valve orifice resulted in reversed vortex ring orientation which was associated with increased viscous energy loss [9, 18], similar to the findings in three patients in this study. Additionally, in an in vivo study using particle image velocimetry and ultrasound, abnormal vortical flow associated with increased energy dissipation was found in patients with an unnaturally oriented or positioned prosthetic mitral valve [37]. Finally, in another CFD simulation of a patient with mitral valve stenosis, de Vecchi et al. [31] reported the formation of an abnormally skewed vortex ring towards the lateral wall which was associated with increased viscous energy loss during diastole.

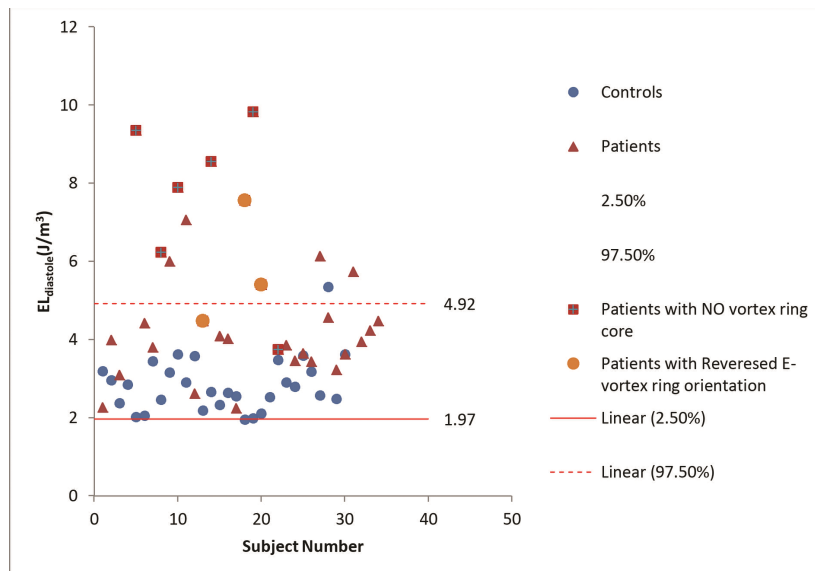


Figure 4.4. Normal limits (95%CI (confidence interval)) of the total viscous energy loss integrated over complete diastole and normalized by stroke volume ($EL_{diastole}$) as derived from thirty healthy controls (in blue circles). Solid red horizontal line represents the 2.5% (lower limit) and dashed red horizontal line represents 97.5% (upper limit). Five (out of the six) patients who showed no vortex ring formation during E-filling presented elevated viscous energy loss considerably beyond the upper limit of the healthy controls. Likewise, two (out of the three) patients who presented E-peak vortex ring orientation above the 95%CI showed significant increase in viscous energy loss beyond the upper limit with the remaining patient approaching the upper limit.

Highest viscous energy loss was found in patients who presented without a ring-shaped vortex during early filling. Given the suggested role of vortex ring formation in minimizing inflow collision with the LV wall [3, 6, 8, 9, 18], the absence of vortex ring formation in patients could lead to a disorganized LV inflow with increased blood-wall interaction as a result and associated increased viscous energy loss. In this study, the absence of vortex ring formation during E-filling in patients was further confirmed by a high VFT. This agrees with previous studies showing that in the presence of elevated VFT, the vortex ring will not pinch off from the MV leaflets, i.e., the vortex ring does not form efficiently [18, 37, 38] which was associated with increased viscous energy loss [37]. Furthermore, VFT is proportional to mitral inflow velocity and inversely proportional to mitral inflow diameter [30], therefore, the reported good correlation between VFT with diastolic viscous energy loss in patients might implicate similar association between energy loss and mitral inflow diameter and velocity.

In this study, patients with a normal E-peak vortex ring orientation and radial position presented comparable viscous energy loss to controls. However, this was not the case in patients with normal A-peak vortex ring orientation and/or radial position as significantly higher levels of energy loss during A-filling were presented compared to controls. In these patients, viscous energy loss was significantly elevated during E-filling which might have an additional effect to the viscous energy loss during A-filling and subsequently increasing its total viscous energy loss. Although only in three patients, normal vortex characteristics for both E- and A-filling did show comparable viscous energy loss during E- and A-filling compared to the normal subjects. Reported results of $EL_{diastole}$ in association with E- and A-vortex ring formation suggest that normal vortex ring formation during both E- and A-filling might be necessary to maintain normal levels of total viscous energy loss over diastole. Accordingly, presence of only normal E-vortex ring formation might not be sufficient to retain or indicate normal total diastolic viscous energy loss. This could suggest the need to extend vortex flow analysis in the LV to A-filling vortex ring formation which is not included in recent analyses of vortex formation [30, 38].

Despite the normal ranges of conventional global diastolic and systolic functional parameters in the studied patients, viscous energy loss was significantly increased and discriminative in patients compared to healthy controls. This included a more pronounced decrease in $\dot{E}L_{E/A}$ compared to the conventional E/A ratio. This may suggest that viscous energy loss could be more sensitive to altered LV inflow than conventional global diastolic parameters.

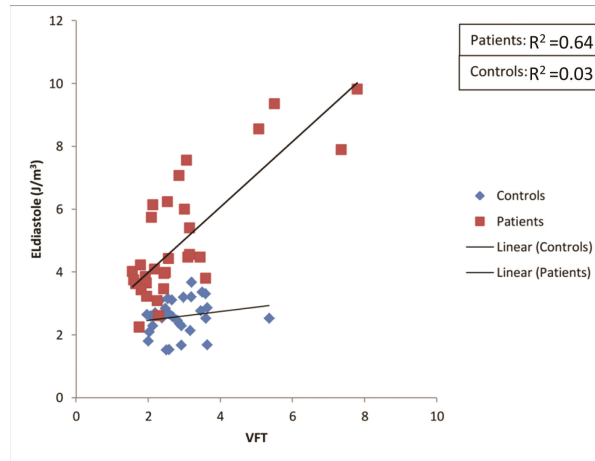
Table 4.5. Viscous energy loss in corrected-AVSD patients with normal or abnormal E-peak vortex ring orientation and/or radial position

	Phase	N	Vortex Orientation (degrees)	$\dot{E}L_{E-avg}$ (W/m^3)	$\dot{E}L_{A-avg}$ (W/m^3)	$EL_{diastole}$ (J/m^3)
Patients with Orientation within 95% CI	E-filling	9	71±10 ^{NS}	8.4±1.8 ^{NS}	8.3±3.9 ^b	3.8 [2.6–4.0] ^a
	A-filling	10	71±7 ^{NS}	9.7±2.6 ^b	6.7±3.9 ^b	3.7±0.8 ^b
Patients with Orientation below 95% CI	E-filling	14	37±11 ^b	10.0±3.2 ^b	8.3±4.2 ^b	4.4±1.30 ^b
	A-filling	9	35±13 ^b	10.0±3.7 ^b	8.3±4.0 ^b	4.8±1.1 ^b
Patients with Orientation above 95% CI	E-filling	3	118±16 ^b	16.1±5.2 ^b	8.1±5.3 ^a	5.8±1.6 ^b
	A-filling	0	-	-	-	-
		N	Normalized Radial Position	$\dot{E}L_{E-avg}$ (W/m^3)	$\dot{E}L_{A-avg}$ (W/m^3)	$EL_{diastole}$ (J/m^3)
Patients with Radial position within 95% CI	E-filling	20	0.29±0.06 ^{NS}	9.5 [7.4–12.5] ^b	8.1±4.1 ^b	4.1±1.4 ^b
	A-filling	12	0.25±0.07 ^{NS}	10.5±3.4 ^b	6.5±3.3 ^b	4.0(3.4–5.2) ^b
Patients Radial position below 95% CI	E-filling	0	-	-	-	-
	A-filling	0	-	-	-	-
Patients with Radial position above 95% CI	E-filling	6	0.43±0.03 ^b	9.0±1.8 ^a	8.8±4.2 ^b	4.6±1.0 ^b
	A-filling	7	0.47±0.04 ^b	8.7±2.0 ^a	9.3±4.5 ^b	4.2±0.7 ^b
Patients with both Radial position and Orientation within 95% CI	E-filling	8	0.28±0.05 ^{NS}	8.5±1.9 ^{NS}	7.8±3.9 ^b	3.7 [2.5–4.0] ^a
	A-filling	7	0.25±0.08 ^{NS}	9.6±2.9 ^a	4.8±1.7 ^a	3.±1.0 ^a

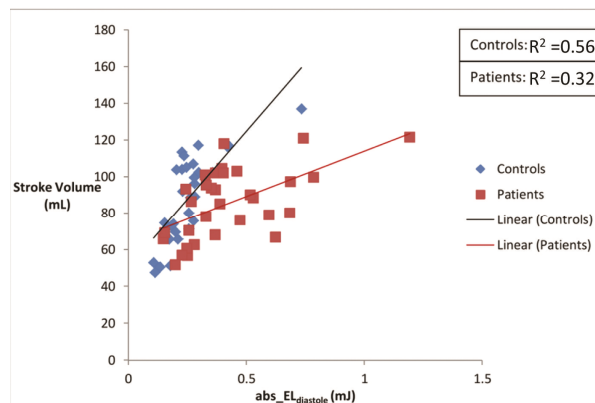
^{NS} $p > 0.05$. ^a $0.01 < p < 0.05$ when compared to controls. ^b $p \leq 0.01$ when compared to controls.

The reported association between viscous energy loss and vortex ring formation emphasizes the previously suggested role of vortex ring formation in optimizing blood flow in the LV [1, 18]. This knowledge can be important for all heart disease, congenital or acquired, leading to cardiac failure. With respect to AVSD patients, this study shows that the surgeon correcting these defects should be aware of the influence of valve abnormalities on energy balance within the LV. Although, currently, the main concern in correcting an AVSD is avoiding regurgitation and/or stenosis, ensuring a more natural orientation/position of the LAVV may encourage normal inflow vortex ring formation and associated minimization of viscous energy loss. Furthermore, altered vortex ring interaction with

the lateral wall might influence the wall shear stress which serves as an epigenetic factor in cardiac remodeling [1, 18]. However, future follow-up studies are needed to assess the impact of abnormal vortex ring formation and its associated increase in viscous energy loss on cardiac function.



(a)



(b)

Figure 4.5 (a) Correlation between total viscous energy loss integrated over diastole but not normalized by stroke volume ($abs_EL_{diastole}$) with stroke volume in controls (blue) and patients (red). (b) Correlation between total viscous energy loss integrated over diastole ($EL_{diastole}$) with vortex formation time (VFT) in controls (blue) and patients (red).

This study has some limitations. The typical limited spatiotemporal resolution of 4DFlow MRI may influence the accuracy of the velocity gradients used in the viscous energy loss equations and therefore, affect the accuracy of the computed viscous energy loss.

However, in this study both controls and patients underwent similar 4DFlow MRI protocols with similar spatiotemporal resolutions to minimize possible discrepancy and to allow for comparative analysis. The aim of this study was to provide relative comparative analysis of viscous energy loss in association with vortex ring formation in subjects acquired under the same resolution/protocol, and not to provide absolute values for viscous energy loss which can be resolution dependent. In this study, the noise level (σ_v), the standard deviation of the signal intensity (i.e. velocity) in the stationary chest wall, was measured and found in the order of 0.75 cm/s in all three directions (0.5% of the velocity sensitivity VENC=150 cm/s). Noise level is expected to be similar among subjects of this study where the 4D flow MRI protocol was maintained similar and therefore, allowing for the relative comparison. Furthermore, the reported strong correlation with kinetic energy, for which no derivatives are involved in its calculation, may further indicate feasibility of the computed viscous energy loss. However, future studies are needed to evaluate the impact of spatial resolution and noise on in-vivo viscous energy loss calculations. The viscous energy loss and kinetic energy computations are automated calculations without observer dependency. Only the LV segmentation from cine short-axis slices required manual interaction. However, this has previously shown to have low inter- and intra-observer variability [39]. The registration of the cine short-axis contours to the 4DFlow MRI was performed automatically using the Elastix image registration toolbox [27].

The presence and absence of vortex rings was visually scored. Nevertheless, a previous study [16] showed that vortex detection can be done with low inter- and intra-observer variation. Moreover, the absence of vortex ring formation in some patients in this study was further confirmed by the significantly high VFT values which are in good agreement with previous literature. Analysis of vortex ring formation was limited to only E-peak and A-peak, subsequently no data was available on the timing, forming and disappearance of the vortex rings. It was the objective of this work to mainly characterize and quantify the viscous energy loss globally by means of average and total viscous energy loss (over E-, A-filling and complete diastole), to associate with vortex ring formation at peak E-filling, peak A-filling as full vortex ring development occurs at these phases [16]. Analysis of the association between the instantaneous viscous energy loss rate over the cardiac cycle and corresponding instantaneous vortex ring evolution/deformation could provide more insights on vortex-energy association but was beyond the focus of this work. Future studies are needed to assess the impact of vortex ring time evolution on viscous energy loss. The presence of elevated kinetic energy as reported in patients with absent E-vortex,

may yield turbulent flow which increases energy loss by means of turbulence [10, 18]. Whenever turbulent energy loss is present in the flow, it can dominate the viscous dissipation by orders of magnitude, becoming the main source of energy loss [10, 18]. Turbulent energy loss [40] was not investigated in this study and is left for future work.

In this study, a possible effect of the left bundle branch block observed in 6 patients cannot be ruled out, but we expect that this will predominantly influence LV ejection during systole and not the LV inflow during diastole, which is the focus of this work.

In the current MRI study, the VFT values in controls were lower than previously reported range [3.5-5.5] with echocardiography and CFD [30]. This might be due to differences between modalities and their measurement of valve diameter. However, our results are in agreement and may further confirm the recent Echo publication by Stewart et al. [41] who studied VFT of sixty volunteers using echocardiography and reported a mean of 1.6, much below the previously reported CFD-derived and experimentally observed VFT, suggesting that the vortex ring pinch-off in the human left ventricle occurs before the end of E-filling i.e. earlier than the experimentally observed and CFD-derived time range. Moreover, in this study, VFT measurements were comparable and not significantly different between controls and patients who presented an E-vortex ring core. Meanwhile, the considerably higher VFT values in patients with an absent E- vortex ring confirm that patients with a narrow mitral valve diameter and higher peak velocity develop abnormal vortex flow [30, 36].

In this work, stroke volume was used to normalize the in vivo-derived LV energetics. A similar approach was used in a recent study where Mangual et.al. [32] have normalized energy dissipation to account for stroke volume differences between subjects. However, a previous in vitro CFD study of Fontan patients [42] suggested a different normalization of energy dissipation by $\rho \frac{CO^3}{BSA}$ with ρ as the blood density, CO as cardiac output and BSA as body surface area. Future in vivo studies are needed to evaluate the impact of different normalizations on energy loss (dissipation) for inter-subject analysis.

4D flow MRI was acquired without respiratory gating. However, a recent publication showed that 4D flow MRI acquired without respiratory gating yields comparable quantitative measurements, both kinetic energy and vortex ring formation, to 4D flow MRI with respiratory gating [43]. Furthermore, possible errors due to motion blurring from breathing are expected to be similar in magnitude between patients and controls.

4.6. Conclusion

Altered vortex ring formation in the blood flow during LV filling is associated with elevated viscous energy in the LV in the studied patient cohort. Further work is needed to understand the connection between increased viscous energy loss in the LV and clinical outcomes.

4.7. References

1. Pedrizzetti, G., et al., The vortex-an early predictor of cardiovascular outcome? *Nature Reviews Cardiology*, 2014. 11(9): p. 545-553.
2. Hong, G.R., et al., Characterization and Quantification of Vortex Flow in the Human Left Ventricle by Contrast Echocardiography Using Vector Particle Image Velocimetry. *Jacc-Cardiovascular Imaging*, 2008. 1(6): p. 705-717.
3. Kheradvar, A., et al., Assessment of transmitral vortex formation in patients with diastolic dysfunction. *Journal of the American Society of Echocardiography*, 2012. 25(2): p. 220-227.
4. Martinez-Legazpi, P., et al., Contribution of the Diastolic Vortex Ring to Left Ventricular Filling. *Journal of the American College of Cardiology*, 2014. 64(16): p. 1711-1721.
5. Sengupta, P.P., J. Narula, and Y. Chandrashekhar, The Dynamic Vortex of a Beating Heart Wring Out the Old and Ring in the New! *Journal of the American College of Cardiology*, 2014. 64(16): p. 1722-1724.
6. Kilner, P.J., et al., Asymmetric redirection of flow through the heart. *Nature*, 2000. 404(6779): p. 759-761.
7. Domenichini, F., G. Pedrizzetti, and B. Baccani, Three-dimensional filling flow into a model left ventricle. *Journal of fluid mechanics*, 2005. 539: p. 179-198.
8. Pedrizzetti, G. and F. Domenichini, Nature optimizes the swirling flow in the human left ventricle. *Physical review letters*, 2005. 95(10): p. 108101.
9. Pedrizzetti, G., F. Domenichini, and G. Tonti, On the left ventricular vortex reversal after mitral valve replacement. *Annals of biomedical engineering*, 2010. 38(3): p. 769-773.
10. Akins, C.W., B. Travis, and A.P. Yoganathan, Energy loss for evaluating heart valve performance. *The Journal of thoracic and cardiovascular surgery*, 2008. 136(4): p. 820-833.
11. Adachi, I., et al., Surgical anatomy of atrioventricular septal defect. *Asian Cardiovascular and Thoracic Annals*, 2008. 16(6): p. 497-502.
12. Penkoske, P.A., et al., Further observations on the morphology of atrioventricular septal defects. *The Journal of thoracic and cardiovascular surgery*, 1985. 90(4): p. 611-622.
13. Takahashi, K., et al., Quantitative real-time three-dimensional echocardiography provides new insight into the mechanisms of mitral valve regurgitation post-repair of atrioventricular septal defect. *Journal of the American Society of Echocardiography*, 2012. 25(11): p. 1231-1244.
14. Elbaz, M.S., et al., Disturbed diastolic left ventricular inflow vortex ring formation in patients with corrected atrioventricular septal defect: quantitative three-dimensional vortex core analysis from 4DFlow MRI. *Journal of Cardiovascular Magnetic Resonance*, 2015. 17(Suppl 1): p. O4.
15. Calkoen, E.E., et al., Characterization and improved quantification of left ventricular inflow using streamline visualization with 4DFlow MRI in healthy controls and patients after atrioventricular septal defect correction. *Journal of Magnetic Resonance Imaging*, 2014.
16. Elbaz, M.S., et al., Vortex flow during early and late left ventricular filling in normal subjects: quantitative characterization using retrospectively-gated 4D flow cardiovascular magnetic resonance and three-dimensional vortex core analysis. *Journal of Cardiovascular Magnetic Resonance*, 2014. 16(1): p. 78.

17. Calkoen, E.E., et al., Altered Left Ventricular Vortex Ring Formation by 4DFlow MRI after repair of Atrioventricular Septal Defects. *The Journal of Thoracic and Cardiovascular Surgery*, 2015.
18. Kheradvar, A. and G. Pedrizzetti, Vortex formation in the cardiovascular system. 2012, Springer. p. 45-79.
19. Markl, M., et al., 4D flow MRI. *Journal of Magnetic Resonance Imaging*, 2012. 36(5): p. 1015-1036.
20. Barker, A.J., et al., Viscous energy loss in the presence of abnormal aortic flow. *Magnetic Resonance in Medicine*, 2014. 72(3): p. 620-628.
21. Bird, R.B., W.E. Stewart, and E.N. Lightfoot, *Transport phenomena*. 2007: John Wiley & Sons.
22. Venkatachari, A.K., et al., Noninvasive quantification of fluid mechanical energy losses in the total cavopulmonary connection with magnetic resonance phase velocity mapping. *Proceedings of the National Academy of Sciences*, 2007. 25(1): p. 101-109.
23. Hoohenkerk, G.J., et al., More than 30 years' experience with surgical correction of atrioventricular septal defects. *The Annals of thoracic surgery*, 2010. 90(5): p. 1554-1561.
24. Calkoen, E.E., et al., Characterization and quantification of dynamic eccentric regurgitation of the left atrioventricular valve after atrioventricular septal defect correction with 4D Flow cardiovascular magnetic resonance and retrospective valve tracking. *Journal of Cardiovascular Magnetic Resonance*, 2015. 17(1): p. 18.
25. Calkoen, E.E., et al., High-temporal velocity-encoded MRI for the assessment of left ventricular inflow propagation velocity: Comparison with color M-mode echocardiography. *J Magn Reson Imaging*, 2015.
26. Calkoen, E.E., et al., Disturbed Intracardiac Flow Organization After Atrioventricular Septal Defect Correction as Assessed With 4D Flow Magnetic Resonance Imaging and Quantitative Particle Tracing. *Investigative Radiology*, 2015.
27. Klein, S., et al., Elastix: a toolbox for intensity-based medical image registration. *IEEE Transactions on Medical Imaging*, 2010. 29(1): p. 196-205.
28. Westenberg, J.J., et al., Mitral Valve and Tricuspid Valve Blood Flow: Accurate Quantification with 3D Velocity-encoded MR Imaging with Retrospective Valve Tracking I. *Radiology*, 2008. 249(3): p. 792-800.
29. Jeong, J. and F. Hussain, On the identification of a vortex. *Journal of fluid mechanics*, 1995. 285: p. 69-94.
30. Gharib, M., et al., Optimal vortex formation as an index of cardiac health. *Proceedings of the National Academy of Sciences*, 2006. 103(16): p. 6305-6308.
31. de Vecchi, A., et al., Towards a fast and efficient approach for modelling the patient-specific ventricular haemodynamics. *Progress in biophysics and molecular biology*, 2014. 116(1): p. 3-10.
32. Mangual, J.O., et al., Comparative numerical study on left ventricular fluid dynamics after dilated cardiomyopathy. *Journal of biomechanics*, 2013. 46(10): p. 1611-1617.
33. Carlsson, M., et al., Quantification of left and right ventricular kinetic energy using four-dimensional intracardiac magnetic resonance imaging flow measurements. *American Journal of Physiology-Heart and Circulatory Physiology*, 2012. 302(4): p. H893-H900.
34. Hussaini, S.F., A. Roldán-Alzate, and C.J. Francois, Left and right ventricular kinetic energy using time-resolved versus time-average ventricular volumes. *Journal of Cardiovascular Magnetic Resonance*, 2015. 17(1): p. 1-2.
35. Ando, M. and Y. Takahashi, Variations of atrioventricular septal defects predisposing to regurgitation and stenosis. *The Annals of thoracic surgery*, 2010. 90(2): p. 614-621.
36. Kheradvar, A. and A. Falahatpisheh, The effects of dynamic saddle annulus and leaflet length on transmitral flow pattern and leaflet stress of a bileaflet bioprosthetic mitral valve. *Journal of Heart Valve Disease*, 2012. 21(2): p. 225.
37. Faludi, R., et al., Left ventricular flow patterns in healthy subjects and patients with prosthetic mitral valves: an in vivo study using echocardiographic particle image velocimetry. *The Journal of thoracic and cardiovascular surgery*, 2010. 139(6): p. 1501-1510.

38. Jiamsripong, P., et al., Impact of Acute Moderate Elevation in Left Ventricular Afterload on Diastolic Transmitral Flow Efficiency: Analysis by Vortex Formation Time. *Journal of the American Society of Echocardiography*, 2009. 22(4): p. 427-431.
39. Van der Geest, R.J., et al., Comparison between manual and semiautomated analysis of left ventricular volume parameters from short-axis MR images. *Journal of computer assisted tomography*, 1997. 21(5): p. 756-765.
40. Dyverfeldt, P., et al., Assessment of fluctuating velocities in disturbed cardiovascular blood flow: in vivo feasibility of generalized phase-contrast MRI. *Journal of Magnetic Resonance Imaging*, 2008. 28(3): p. 655-663.
41. Stewart, K.C., et al., Left ventricular vortex formation is unaffected by diastolic impairment. *American Journal of Physiology-Heart and Circulatory Physiology*, 2012. 303(10): p. H1255-H1262.
42. Dasi, L.P., et al., Functional analysis of Fontan energy dissipation. *Journal of biomechanics*, 2008. 41(10): p. 2246-2252.
43. Kanski, M., et al., Whole-heart four-dimensional flow can be acquired with preserved quality without respiratory gating, facilitating clinical use: a head-to-head comparison. *BMC medical imaging*, 2015. 15(1): p. 20.

Chapter 5

Abnormal left atrial flow patterns in patients after atrio-ventricular septal defect correction and regurgitation: evaluation with 4DFlow Magnetic Resonance Imaging and particle tracing

This chapter was adapted from:

Calkoen E. E., Elbaz, M. S., de Koning P. J.H., Jongbloed M. R. M., Kroft L. J. M., van der Geest, R. J., Blom N. A., de Roos A., Roest, A. A., & Westenberg, J. J. **Abnormal left atrial flow patterns in patients after atrioventricular septal defect correction and regurgitation: evaluation with 4DFlow Magnetic Resonance Imaging and particle tracing.** *submitted.*

Abstract

Background: During ventricular systole, a compact recirculating flow pattern forms in the left atrial (LA) blood flow. We aimed to evaluate LA recirculating flow structures in healthy volunteers and patients with corrected atrioventricular septum defect (AVSD) with both none-mild and moderate left atrioventricular valve (LAVV) regurgitation with the use of 4DFlow MRI.

Methods: Data was obtained in eighteen controls (age 24 ± 14 years) and eighteen corrected AVSD patients: nine (24 ± 12 years) with none-mild regurgitation ($< 9\%$) and nine (21 ± 13 years) with moderate regurgitation ($> 17\%$). Recirculating flow was quantified based on streamline visualization in late systole. Vortex cores were extracted by the lambda2-method at this time point and backwards particle tracing was performed to quantify contribution of the left pulmonary veins (LPVs) and right pulmonary veins (RPVs) respectively to the vortex core.

Results: In healthy controls, a single recirculating flow structure was visualized in the LA by streamlines (size 4.3 ± 2.9 mL) with a similar volume as the lambda2-extracted vortex core (3.9 mL, IQR 3.0–6.8 mL, $p=0.27$). In patients with regurgitation of the LAVV, two recirculating flow structures were observed in the LA, with opposing circulation direction. Recirculating blood flow contribution originated less frequently from the LPVs in patients with none-mild regurgitation ($27 \pm 25\%$, $p=0.023$) and moderate regurgitation (6%, IQR 0–23%, $p=0.002$) compared with controls ($49 \pm 21\%$).

Conclusion: Quantitative 3D analysis showed disturbed recirculating LA flow patterns in corrected AVSD patients with decreased contribution to the vortex cores from the LPVs. Furthermore, LAVV regurgitation caused multiple recirculating flow structures and disturbed flow from the LPVs.

5.1. Introduction

The left atrium (LA) has a reservoir function during ventricular systole when blood enters from the right pulmonary veins (RPVs) and left pulmonary veins (LPVs). During diastole, after opening of the left atrioventricular valve (LAVV), the LA serves as a conduit when blood flows from the RPVs and LPVs through the LA into the left ventricle. Efficient filling of the LA, contraction and draining into the ventricle contribute to adequate cardiac function [1].

Recirculating flow patterns and vortex formation are well described in the left ventricle and are known to contribute to efficient blood flow [2]. Recirculating flow in the LA has been described in healthy hearts during systole and mid-diastole based on streamline and pathline analysis from intra-cardiac blood flow velocity data. This phenomenon is suggested to play a role in preventing thrombus formation, preservation of LA flow momentum during ventricular systole and efficient diastolic left ventricular (LV) filling [1, 3-5]. Previous studies suggest that the recirculating flow during ventricular systole mainly consist of blood originating from the LPVs. Blood flow from the RPVs was proposed to be directed along the inter-atrial septum towards the ventricle [1].

Regurgitation of the left atrioventricular valve (LAVV) has been a predictor for a poor clinical outcome even in asymptomatic patients [6]. An increase in turbulent kinetic energy in the LA has been described around LAVV regurgitation jets [7]. Patients after atrioventricular septal defect (AVSD) correction often present with LAVV regurgitation [8] and the re-operation rate is as high as 28% [9]. Moreover, the regurgitation direction in corrected AVSD patients is lateral towards the ostia of the LPVs, though the direction varies dynamically during systole [10]. We hypothesize that the dynamic and eccentric regurgitant jet in these patients disturbs formation of normal LA recirculating blood flow patterns.

Novel 4DFlow MRI techniques allow 3D quantification of intra-cardiac flow patterns and vortex analysis [11, 12]. Therefore, the aim of this explorative study was to evaluate flow patterns in the LA in healthy subjects and patients after AVSD correction with the use of 4DFlow MRI-based visualization methods. In this study, normal flow behavior in the LA will be evaluated in healthy controls and in patients after correction of an AVSD correction. Furthermore, the effect of LAVV regurgitation on LA flow patterns will be studied by comparing left atrial flow patterns in patients with none-to-mild versus moderate LAVV regurgitation.

5.2. Methods

Twenty healthy controls and twenty patients with a corrected AVSD were included. Patients were selected from a total group of 34 patients who underwent cardiac MRI. Selection was based on regurgitation grade: ten patients were selected with none to mild regurgitation (regurgitation fraction below 9%) and ten patients with moderate regurgitation (regurgitation fraction above 17%). Subjects with aliasing in LA velocity data were excluded. Informed consent was obtained from all patients and controls and/or their parents. Subjects and controls in the current study were also included in previous studies using 4DFlow MRI [10, 12, 13], but in none of these studies atrial flow patterns were evaluated.

5.2.1. Magnetic Resonance Imaging

All subjects underwent whole-heart 4DFlow MRI on a 3T system (Ingenia, Philips Medical Systems, The Netherlands) with maximal amplitude of 45mT/m for each axis and a slew rate of 200T/m/sec. A combination of FlexCoverage Posterior coil in the Table top with a dStream Torso coil, providing up to 32 coil elements for signal reception was used, with the following acquisition settings: velocity-encoding of 150cm/s in all three directions, spatial resolution $2.3 \times 2.3 \times 3.0$ - 4.2mm^3 , flip angle 10° , echo time (TE) 3.2ms, repetition time (TR) 7.7ms, true temporal resolution ($4 \times \text{TR}$) 31ms, SENSE factor 2 in anterior-posterior direction and Echo Planar Imaging with a factor 5. Retrospective VCG-gating was used with 30 phases reconstructed to represent one average heart cycle and free breathing without motion compensation was allowed. Commercially-available concomitant gradient correction and local phase correction filter were applied from the software available on MRI system (Ingenia 3 T with Software Stream 4.1.3.0). Acquisition time of the 4DFlow scan with a heart beat 60-80bpm was typically 8-10 minutes. Cine 2D left 2-chamber and 4-chamber views were acquired to quantify maximal left atrial volume according to the biplane area-length method $(8/3\pi \times \text{Area}(4 - \text{chamber}) \times \text{Area}(2 - \text{chamber})) / (\text{shortest atrial length})$.

5.2.2. Streamline evaluation of compact recirculating flow

As regurgitation occurs during ventricular systole, flow patterns were evaluated during the reservoir function phases of the LA. Streamline display of the velocity field at any instant of time allows visualization of flow structures at a specific time point [14]. Streamline visualization using Mass software (LUMC, Leiden, The Netherlands) was used

to assess and quantify compact recirculating flow structures in the LA. A stack of reformatted planes parallel to the 4-chamber view was analyzed with streamlines to visualize the flow pattern in the LA. The number of compact recirculating flow structures (i.e. where streamlines are circular and connected) was visually scored and the rotational direction with respect to the feet-head axis (clockwise or counter-clockwise) was determined (Figure 5.1A). A previous study showed that the vortex inside the atrium reached its largest volume just before the end of systole [1]. Therefore, the volume of the compact recirculating flow structure was measured two phases before end-systole. The compact recirculating flow structure was manually outlined in each axial slice and the areas were summed and multiplied by the slice thickness to compute the volume of the recirculating flow structure.

5.2.3. Vortex detection in the left atrium and particle tracing

Three-dimensional (3D) vortex cores can be identified using the gradient properties of the 4DFlow MRI data [12]. Vortex core detection was used to provide a more objective definition of the compact region of recirculating flow in the LA. Backwards particle tracing [15] was then used to distinguish respective contribution of the LPVs and RPVs to the detected vortex core. First, the LA was manually segmented on magnitude images of the 4DFlow scans. Subsequently the lambda2-method [12] was used to detect the vortex core from the velocity field two phases before end-systole. The 3D velocity data of the whole-heart 4DFlow acquisition was used for particle tracing algorithm, using 4th order Runge-Kutta numerical integration to create pathlines. To identify the origin of the recirculating flow, each voxel in the vortex core was designated as a seed point and backward particle tracing was performed until the start of systole. At the first phase of systole the particles were scored as 1) originating from LPVs; 2) originating from RPVs; 3) originating from LV (i.e., regurgitation); 4) particles already present in LA at start of systole (Figure 5.1). Particles entering the LA from outside the heart and not part of the pulmonary venous flow or LV regurgitation were excluded and considered as tracing errors (i.e., particles crossing the myocardial wall due to the discrete time step or spatial discretization used in the integration algorithm or due to other sources of error such as imaging artifacts). Additionally, to calculate the contribution of particles originating from LPVs and RPVs to the whole LA volume, at the same phase (two phases before systole) the whole atrium was seeded with particles and backwards tracing was performed to the start of systole.

5.2.4. Retrospective flow quantification

Using the same 4DFlow data set, retrospective valve tracking and through-plane flow mapping over the aorta and LAVV was performed. From aortic and LAVV flow-time curves the start and end of systole were determined as well as the regurgitation fraction [16]. Furthermore, the combined flow through the superior and inferior LPVs and the combined flow through the superior and inferior RPVs was quantified by retrospectively placing measurement planes at the ostium of each pulmonary vein, perpendicular to the inflow direction into the LA as visualized with streamlines. A resultant flow-time curve was formed for the summed LPVs and RPVs and peak systolic (S) and peak diastolic (D) flow from the pulmonary veins was defined. Furthermore, the time to peak systolic flow was determined.

5.2.5. Statistical analysis

Data are described as mean \pm standard deviation or median (interquartile range) where appropriate. Differences between patients and controls are calculated with an independent t-test or Mann-Whitney U test where appropriate. The within-subject difference were tested with a paired t-test or Wilcoxon signed-rank test where appropriate between 1) volume of the compact recirculating flow structure (defined by streamlines) and vortex core volume defined using the lambda2-method) 2) the left atrial inflow volume defined with particle tracing and the total trans-pulmonary vein inflow. Correlation between different flow volumes were evaluated with Pearson's test.

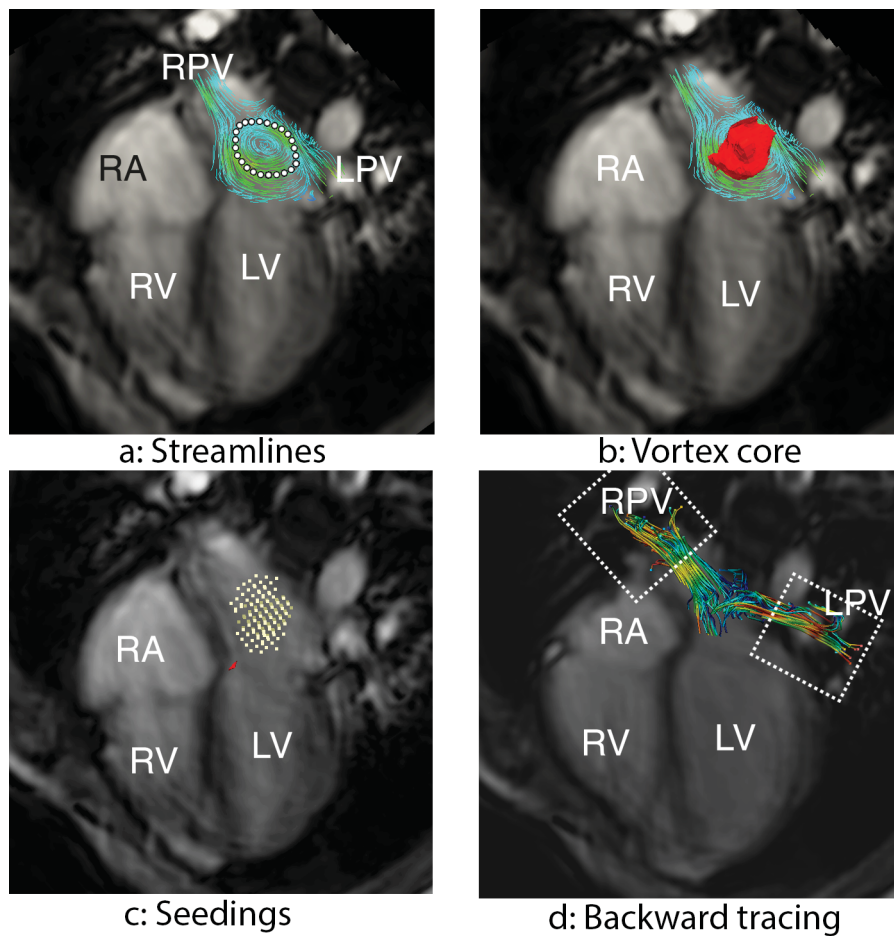
5.3. Results

Visual grading of the 4DFlow scans revealed aliasing in the area of the LA in 2 controls and 2 patients (1 with none to mild regurgitation and 1 with moderate regurgitation), who were excluded from further analysis. Characteristics of included subjects are described in Table 5.1.

5.3.1. Controls

In the remaining 18 controls, a single counter-clockwise (with respect to the feet-head axis) compact recirculating flow pattern could be detected with streamline visualization during ventricular systole (Figure 5.2A). The manually segmented compact recirculating flow structure had a median volume of 4.3 ± 2.9 mL when measured just before end-systole. These measured volumes showed modest correlation with total LA

volume ($r = 0.60$, $p = 0.009$), but not with age ($p = 0.73$). In all controls, a vortex core could be detected with the lambda2-method in the LA. The median volume (3.9mL, IQR 3.0 – 6.8mL) was not different from the volume detected with streamlines (mean difference 0.51mL, $p = 0.267$ with 95%CI -0.7 – 1.7mL) and correlation between both volumes was $r = 0.61$ ($p = 0.007$).



5

Figure 5.1. Explanation of used methodology. Streamline visualization shows recirculating flow (dotted line in A) in clockwise direction with respect to the feet-head axis. The lambda2-method is used to extract the vortex core (red in B). Vortex cores are filled with seeds (dots in C). Backwards particle tracing allows the distinction between flow from the right pulmonary veins (RPV) and left pulmonary veins (LPV). RA = right atrium, RV = right ventricle, LV = left ventricle.

Backward tracing of the vortex core volume revealed a mean of $49 \pm 21\%$ of the total vortex volume originating from the LPVs, a median of 7% IQR 3 – 14% originating from the RPVs with a remaining mean of $40 \pm 15\%$ of the total vortex volume originating from blood particles already present within the atrium at the start of ventricular systole. The flow from the four pulmonary veins could be separately detected and quantified in 15 of 18 controls. In the remaining three controls, streamline visualization was not adequate to depict LA inflow at the ostium of all four veins respectively, and to perform retrospective flow mapping. For the remaining 15 controls, the combined flow from the four veins ($38 \pm 15\text{mL}$) was comparable to the combined particle volumes of the LPVs and RPVs after seeding the whole atrium and backward tracing ($36 \pm 15\text{mL}$) (mean difference -1.8 mL , $p = 0.60$, 95%CI $-9.3 - 6.0\text{ mL}$). Pulmonary venous flow during ventricular systole in controls showed a right-left volume ratio of 1.2 ± 0.4 . Peak velocity was significantly higher in the LPVs ($54 \pm 14\text{cm/s}$) as compared with the RPVs ($36 \pm 11\text{cm/s}$, $p < 0.001$). Peak systolic flow rate was reached in the LPVs $195 \pm 49\text{ms}$ and in the RPV 107ms IQR 87 – 175ms (difference $p = 0.003$) after the start of ventricular systole.

Table 5.1. Subject characteristics

	Controls	Patients with none-mild LAVV regurgitation	Patients with moderate LAVV regurgitation
Number	18	9	9
Age (years)	24 ± 14	24 ± 12	21 ± 13
Male (%)	50	66	6
Type of AVSD		6 partial, 3 complete/intermediate	5 partial, 4 complete/intermediate
Age of surgery (months)		58 ± 55	69 ± 110
Time after surgery (years)	-	19 ± 9	16 ± 8
Regurgitation fraction (%)	-	5 ± 2	24 ± 6
Atrial volume (mL)	60 ± 31	74 ± 21	72 ± 24
Atrial volume / BSA (mL/m^2)	34 ± 13	41 ± 8	48 ± 8 *
LV Ejection fraction (%)	62 ± 4	57 ± 4 *	55 ± 8 *

* $p < 0.05$ as compared with controls

5.3.2. Patients

All patients were in sinus rhythm, one patient previously underwent a cardioversion because of atrial fibrillation. In patients, the normal LA flow pattern was disturbed. Differences between both patient groups (none to mild regurgitation and moderate regurgitation) and the controls are presented in Table 5.2.

Of the patients with none to mild regurgitation streamline visualization revealed a single recirculating flow pattern in the LA as seen in controls in 8 (89%) patients and two separate compact recirculating flow structures in 1 (11%) patient, with a regurgitation fraction of 9%. Total volume of compact recirculating flow patterns combined was 3.2 ± 2.0 mL in the none to mild regurgitation group, which was not significantly different from the vortex core volume in controls (mean difference patients with none to mild regurgitation to controls 1.0 mL, $p = 0.34$, 95%CI -1.2 – 3.3 mL). In patients with none to mild regurgitation, particles seeded from inside the vortex core originated less frequently from the LPVs compared with controls ($27 \pm 25\%$, $p = 0.023$). Moreover, an increased contribution to the vortex core of blood already present in the LA at the start of ventricular systole was observed in patients with none to mild regurgitation compared with controls ($57 \pm 23\%$, $p = 0.03$). Using retrospective mapping, detection of flow from four separate pulmonary veins was possible in all patients with none to mild regurgitation and revealed a non-significantly different right-left volume ratio as described in controls (1.1 IQR 0.9 – 1.6, $p = 0.61$). Peak flow velocity was similar in patient and controls in LPVs and RPVs (Table 5.2). In patients with none to mild regurgitation, peak flow rate was reached later in the RPVs as compared with controls (mean difference -69ms, 95%CI -121 – -18ms, $p = 0.01$).

In contrast to the controls, in patients with moderate regurgitation, streamline visualization revealed two or three separate compact recirculating flow structures in the LA in 8 (89%) patients (difference between patient groups $p = 0.002$) (Figure 5.2C). In patients with multiple recirculating flow structures, two structures could be detected around the regurgitant jet; one circulating in counter-clockwise direction and one in clockwise direction with respect to the feet-head axis. In 3 out of 9 patients with recirculating flow around the regurgitant jet, another (third) counter-clockwise recirculating flow pattern was seen more cranially in the atrium. Total volume of compact recirculating flow patterns combined was 4.7 ± 3.4 mL in the moderate regurgitation group, which was not significantly different from the vortex core volume in controls (mean difference patients with moderate regurgitation -0.4mL, $p = 0.74$, 95%CI -3.0 – 2.1 mL). In patients with

moderate regurgitation, particles seeded from inside the vortex core originated less frequently from the LPVs compared with controls (6% IQR 0 – 23%, $p = 0.002$). A trend towards an increased contribution to the vortex core of blood already present in the LA at the start of ventricular systole was observed in patients with moderate regurgitation ($62 \pm 27\%$, $p = 0.05$) compared with controls. Pulmonary venous flow quantification, possible in five patients with moderate regurgitation, revealed a non-significantly different right-left volume ratio as described in controls (1.3 ± 0.4 , $p = 0.90$). Peak flow velocity was similar in patients and controls in the LPVs and RPVs (Table 5.2). Systolic peak flow rate was reached later in the cardiac cycle in patients with moderate regurgitation compared with controls in both the LPVs (mean difference -48ms , 95%CI $-84 - -12\text{ms}$, $p = 0.012$) and the RPVs (mean difference -92ms , 95%CI $-139 - -44\text{ms}$, $p = 0.001$). Time to systolic peak flow rate in the LPVs was moderately correlated with the regurgitation fraction ($r = 0.49$, $p = 0.04$) whereas timing of peak flow rate in RPVs was not significantly correlated.

5.4. Discussion

This explorative study provides new insights in blood flow characteristics in the LA in healthy controls and patients after AVSD correction with recurrent LAVV regurgitation, with the combined use of streamline visualization, semi-automated vortex core detection and particle tracing of pulmonary venous flow of 4DFlow MRI data. Key findings of the study are 1) in controls, on average 49% of volume of the single compact recirculating flow structure in the LA originates from the LPVs, but also on average 7% contribution to the volume originating from the RPVs was observed; 2) in corrected AVSD patients with none to mild regurgitation and with moderate regurgitation, the LPVs contribute less to the vortex core and systolic peak flow was reached later in the RPV; 3) additional differences in corrected AVSD patients with moderate LAVV regurgitation are multiple compact recirculating flow patterns and delayed systolic peak flow in the LPV that was related to regurgitation fraction.

5.4.1. Vortex formation in the LA in healthy controls

During ventricular systole the LA is filled and serves as an expanding reservoir. Previous studies observed recirculating blood in the LA [1, 3-5], which in some studies is addressed as vortex flow. The recirculating flow conceivably avoids stasis and thrombosis and minimizes static pressure on the atrial wall [17]. Recirculating flow also contributes to

the preservation of momentum in blood flow during ventricular systole, when the atrium is filled. Preserved momentum may aid efficient LV filling during early diastole.

Previous MRI studies used vector graphs, streamline analysis and pathline analysis [1, 4, 18] to visualize recirculating flow in 3D, however quantification of duration and size (area) of recirculating flow was limited to a 2D plane. Park et al. used echocardiography [5], with the advantage of a high frame rate and real-time imaging, but the limitation of analyzing 3D structures on 2D images. Complementing the quantification based on streamlines, the current study used the lambda2-method [12], to allow quantification of atrial vortex flow in 3D. Volumes of streamline-based recirculating flow were comparable to lambda2-detected atrial vortex cores, however, the shape of vortex cores appeared more irregular than the usually compact structures as segmented on streamline representation.

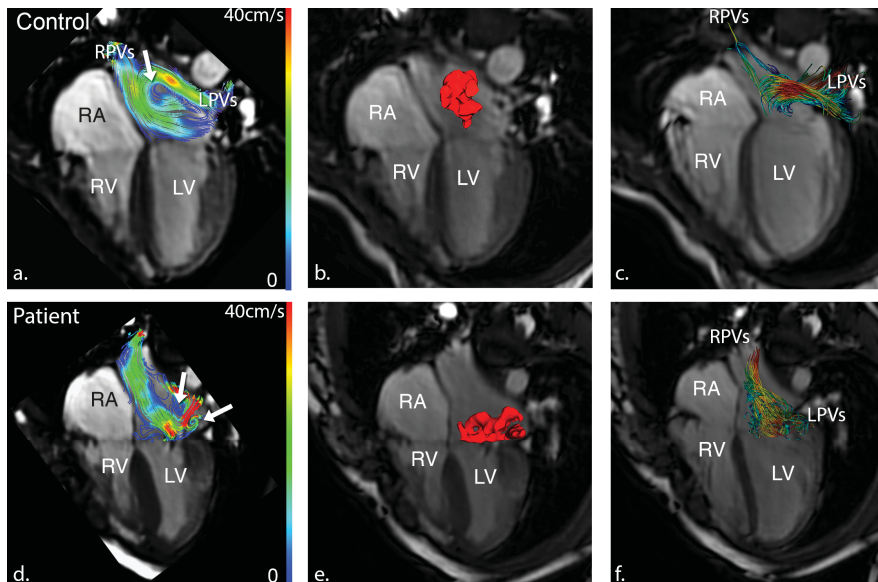


Figure 5.2. Differences between healthy control (A-C) and a patient with 36% left atrioventricular valve regurgitation (D-F). Streamline visualization shows a single counter-clockwise (with respect to the feet-head axis) recirculating flow structure in the control (arrow in A) compared with multiple recirculating flow structures in the patient (arrows in D). The vortex core in the patient is less compact and nearer to the atrioventricular valve (E). Backward tracing in the healthy control shows predominant contribution of the left pulmonary veins (LPVs) to the vortex core, whereas in the patient only contribution from the right pulmonary veins (RPVs) is observed (F). RA = right atrium, RV = right atrium, LV = left ventricle.

Table 5.2. Differences between controls and the two patients groups.

		Controls	Patients with none-mild LAVV regurgitation	Patients with moderate LAVV regurgitation
N		18	9	9
Streamlines	Volume compact recirculating flow (mL)	4.3 ± 2.9	3.2 ± 2.0	4.7 ± 3.4
	Rotational direction	100% single, counter-clockwise	89% single counter-clockwise, 11% one counter-clock wise and one clockwise	11% single counter-clockwise, 11% two counter-clockwise structures and 78% one counter-clockwise and one clockwise
Vortex core	Volume vortex (mL)	3.9 (IQR 3.0 – 6.8)	4.0 (IQR 3.3 – 6.8)	4.2 (IQR 2.3 – 6.7)
	Contribution LPVs (%)	49 ± 21	27 ± 25 *	6 (IQR 0 – 23) *
	Contribution RPVs (%)	7 (IQR 3 – 14)	16 ± 15	17 (IQR 4 – 31)
	Residual in atrium (%)	40 ± 15	57 ± 23 *	62 ± 27 *
Pulmonary venous flow	Right-left ratio systolic volume ^	1.3 ± 0.3	1.1 (IQR 0.9 – 1.6)	1.3 ± 0.4
	Peak velocity LPVs (cm/s)	54 ± 14	46 ± 12	49 ± 17
	Peak velocity RPVs (cm/s)	36 ± 11	33 ± 12	36 ± 12
	Time to peak LPVs (ms)	195 ± 49	207 ± 53	242 ± 28 *
	Time to peak RPVs (ms)	107 (IQR 87 – 175)	201 ± 74 *	223 ± 61 *

* indicate $p < 0.05$ as compared with controls. ^ pulmonary vein right-left ratio only computed in cases with four pulmonary veins detected. Rotational direction is described with respect to the feet-head axis.

Postulations that flow from the LPVs mainly contributes to the LA recirculating flow formation and that flow from the RPVs is mostly directed along the LA wall with only little contribution to the vortex, were thus far based on qualitative evaluations only [1]. The

current study quantitatively showed that flow from LPVs in healthy controls has a substantially higher contribution to the vortex core than flow from RPVs (on average 49% versus 7%). The higher peak velocities in the flow from the LPVs compared with the RPVs might be a factor in this difference in contribution. However, even in healthy volunteers a large variation in venous contribution was observed, which is possibly caused by diversity in pulmonary vein anatomy [19], which was not assessed in this study.

5.4.2. Left atrial flow in patients after AVSD correction

A recent 4DFlow streamline-based study showed frequent absence of a vortex core in the LA in patients with a variety of organic heart disease, which was related to pulmonary venous peak velocity, but not pulmonary vein insertion angle [18]. In studies using computer fluid dynamics [20], echocardiography [5] and 4DFlow MRI [3], abnormal LA flow was also described in patients with atrial fibrillation and a relation with thrombus formation was suggested in these patients [21].

Decreased contribution of blood flow from the LPVs to the vortex core was observed in corrected AVSD patients with moderate as well as none to mild regurgitation. Therefore, the laterally directed regurgitation (i.e., towards the LPVs) can only partly explain the decreased contribution of flow from the LPVs to the atrial vortex core in corrected AVSD. Contributing effects may include the different pulmonary vein and LA anatomy after AVSD correction, possibly caused by remodeling after surgery. The delayed peak flow rate in the LPVs was predominately present in patients with moderate LAVV regurgitation and correlated to the regurgitation fraction and might therefore be a direct result of regurgitation or caused by increased atrial pressure secondary to regurgitation.

In the current study, patients after AVSD correction showed a disturbed recirculating flow pattern. Patients after AVSD correction often develop eccentric and dynamic regurgitation of LAVV. In patients with regurgitation, two recirculating structures were detected around the regurgitation jet(s). In an *in vitro* study, regurgitation jets with a high velocity in the presence of a prosthetic mechanical heart valve were related to aberrant LA vortex formation and an increase of shear stress in the blood flow near the wall, which directly activates platelets and has the ability to damage endothelial cells [22]. If endothelial cells fail to produce enough platelet inhibitors, this can lead to thrombus formation. The vortex formation observed around the regurgitant jet(s) in our study may similarly affect the atrial wall. Subsequently, it may contribute to the LA enlargement, diastolic dysfunction and atrial fibrillation observed in patients with chronic regurgitation

of the LAVV [6]. On the other hand, others have suggested a protective property of LAVV regurgitation for thrombus formation, due to the increased velocity which may prevent stasis [23].

The clinical relevance of our preliminary findings comprise the role of disturbed LA flow patterns on outcome in patients with and without regurgitation. Early correction of moderate-severe regurgitation is debated even in asymptomatic patients [6] as regurgitation may result in LA dilatation, diastolic dysfunction and atrial fibrillation. Our study showed that LA blood flow in patients after AVSD correction is disturbed, and specifically LAVV regurgitation disturbs normal recirculating flow structures during ventricular systole. The parameters described in this study can be used in future studies to investigate if regurgitation in patients with other congenital or acquired heart disease similarly disturbs LA flow patterns. Further insights in LA flow patterns will help to better understand the effect of regurgitation on the LA and will eventually allow better prediction of the effect of regurgitation, which may be of benefit to optimization of timing of interventions.

5.4.3. Study limitations

Current study is a pilot study with small numbers of patients and no patients with severe LAVV regurgitation were available. Compact recirculating flow patterns were manually segmented based on streamline visualization. Streamlines only present the velocity field at an instant in time and therefore cannot represent the true trajectory of recirculating flow. To overcome the limitations of streamlines and the manual segmentation, we have in addition used a semi-automatic method to detect vortex cores, which resulted in similar volumes. Particle tracing resembles the true pathlines of blood flow over time, however changes in velocity magnitude and direction faster than the temporal and spatial resolution allow to detect, cannot be represented in the tracing algorithm. The border between atrium and pulmonary veins was manually segmented, which might have introduced inaccuracies in quantification.

5.5. Conclusion

Using 4DFlow MRI, quantitative 3D analysis of recirculating flow structures and vortex cores in the LA blood flow during ventricular systole showed a higher contribution of blood flow from the LPVs versus RPVs in healthy controls. Furthermore, patients after AVSD correction with and without regurgitation presented a decreased contribution of flow from the LPVs to the vortex cores. Finally, LAVV regurgitation in patients with a corrected

AVSD resulted in disturbed LA flow patterns with two recirculating flow structures around the regurgitation jet with an opposed circulation direction. Follow-up studies in patients with disturbed LA flow are needed to further explore the long-term consequences of this disturbed atrial flow on cardiac function.

5.6. References

1. Fyrenius, A., et al., Three dimensional flow in the human left atrium. *Heart*, 2001. 86(4): p. 448-455.
2. Pedrizzetti, G., et al., The vortex-an early predictor of cardiovascular outcome? *Nature Reviews Cardiology*, 2014. 11(9): p. 545-553.
3. Fluckiger, J.U., et al., Left atrial flow velocity distribution and flow coherence using four-dimensional FLOW MRI: A pilot study investigating the impact of age and Pre-and Postintervention atrial fibrillation on atrial hemodynamics. *Journal of Magnetic Resonance Imaging*, 2013. 38(3): p. 580-587.
4. Föll, D., et al., Age, gender, blood pressure, and ventricular geometry influence normal 3D blood flow characteristics in the left heart. *European Heart Journal-Cardiovascular Imaging*, 2013. 14(4): p. 366-373.
5. Park, K.-H., et al., Characterization of the left atrial vortex flow by two-dimensional transesophageal contrast echocardiography using particle image velocimetry. *Ultrasound in medicine & biology*, 2013. 39(1): p. 62-71.
6. Enriquez-Sarano, M., et al., Quantitative determinants of the outcome of asymptomatic mitral regurgitation. *New England Journal of Medicine*, 2005. 352(9): p. 875-883.
7. Dyverfeldt, P., et al., Hemodynamic aspects of mitral regurgitation assessed by generalized phase-contrast MRI. *Journal of Magnetic Resonance Imaging*, 2011. 33(3): p. 582-588.
8. Hoochenkerk, G.J., et al., More than 30 years' experience with surgical correction of atrioventricular septal defects. *The Annals of thoracic surgery*, 2010. 90(5): p. 1554-1561.
9. Lange, R., et al., The presence of Down syndrome is not a risk factor in complete atrioventricular septal defect repair. *The Journal of thoracic and cardiovascular surgery*, 2007. 134(2): p. 304-310.
10. Calkoen, E.E., et al., Characterization and quantification of dynamic eccentric regurgitation of the left atrioventricular valve after atrioventricular septal defect correction with 4D Flow cardiovascular magnetic resonance and retrospective valve tracking. *Journal of Cardiovascular Magnetic Resonance*, 2015. 17(1): p. 18.
11. Calkoen, E.E., et al., Cardiovascular function and flow by 4-dimensional magnetic resonance imaging techniques: new applications. *Journal of thoracic imaging*, 2014. 29(3): p. 185-196.
12. Elbaz, M.S., et al., Vortex flow during early and late left ventricular filling in normal subjects: quantitative characterization using retrospectively-gated 4D flow cardiovascular magnetic resonance and three-dimensional vortex core analysis. *Journal of Cardiovascular Magnetic Resonance*, 2014. 16(1): p. 78.
13. Calkoen, E.E., et al., Characterization and improved quantification of left ventricular inflow using streamline visualization with 4DFlow MRI in healthy controls and patients after atrioventricular septal defect correction. *Journal of Magnetic Resonance Imaging*, 2014.
14. Napel, S., et al., Visualizing three-dimensional flow with simulated streamlines and three-dimensional phase-contrast MR imaging. *Journal of magnetic resonance imaging*, 1992. 2(2): p. 143-153.
15. Buonocore, M.H., Visualizing blood flow patterns using streamlines, arrows, and particle paths. *Magnetic resonance in medicine*, 1998. 40(2): p. 210-226.
16. Westenberg, J.J., et al., Mitral Valve and Tricuspid Valve Blood Flow: Accurate Quantification with 3D Velocity-encoded MR Imaging with Retrospective Valve Tracking I. *Radiology*, 2008. 249(3): p. 792-800.

17. Sengupta, P.P. and J. Narula, A la mode atrioventricular mechanical coupling. *JACC: Cardiovascular Imaging*, 2014. 7(1): p. 109-111.
18. Suwa, K., et al., Characteristics of Intra-Left Atrial Flow Dynamics and Factors Affecting Formation of the Vortex Flow. *Circulation Journal*, 2014. 79(1): p. 144-152.
19. Porres, D.V., et al., Learning from the pulmonary veins. *Radiographics*, 2013. 33(4): p. 999-1022.
20. Mouret, F., et al., In vitro atrial flow dynamics: normal conditions versus atrial fibrillation. *Journal of biomechanics*, 2004. 37(11): p. 1749-1755.
21. Markl, M., et al., Left Atrial 4-Dimensional Flow Magnetic Resonance Imaging: Stasis and Velocity Mapping in Patients With Atrial Fibrillation. *Investigative radiology*, 2015.
22. Milo, S., et al., Mitral mechanical heart valves: in vitro studies of their closure, vortex and microbubble formation with possible medical implications. *European journal of cardiothoracic surgery*, 2003. 24(3): p. 364-370.
23. Fukuda, N., et al., Relation of the severity of mitral regurgitation to thromboembolic risk in patients with atrial fibrillation. *International journal of cardiology*, 2011. 146(2): p. 197-201.

Chapter 6

Automatic extraction of the 3D left ventricular diastolic transmitral vortex ring from 3D whole-heart phase contrast MRI using Laplace-Beltrami signatures

This chapter was adapted from:

ElBaz, M. S., Lelieveldt, B. P., Westenberg, J. J., & van der Geest, R. J. (2014). **Automatic extraction of the 3D left ventricular diastolic transmitral vortex ring from 3D whole-heart phase contrast MRI using Laplace-Beltrami signatures.** In *Statistical Atlases and Computational Models of the Heart. Imaging and Modelling Challenges STACOM-MICCAI* (pp. 204-211). Springer Berlin Heidelberg.

Abstract

In this work, a new method is proposed for automatic extraction of the left ventricular diastolic transmitral vortex ring from 3D whole-heart three directional Phase Contrast MRI. The proposed method consists of two parts, training and extraction. In the training step, an average reference signature of the complex transmitral vortex ring is captured from training subjects using Laplace-Beltrami spectrum and the Lambda2 method. In the vortex extraction step, the trained signature is used to identify the vortex ring by performing an iterative search for the vortex object with minimum distance from the trained signature. The proposed method is validated on a dataset of 8 healthy volunteers with 32 observed diastolic vortex rings. The method was able to successfully extract 27 diastolic vortex rings from a total of 32. Furthermore, the conducted experiments showed the capability of the proposed method in dealing with vortex shape changes that occur between the phases of early and late diastolic filling.

6.1. Introduction

Vortex formation in intra-cardiac flow patterns has recently gained much interest due to its vital role in keeping balance between blood motion and stresses of surrounding structures. Vortices are complex flow structures that evolve as a result of a change in velocity direction around an imaginary axis. In the cardiac Left Ventricle (LV), during early and late diastolic filling, the flow behind the mitral valve develops as a closed vortex tube: a vortex ring [1]. Vortex rings are frequently observed in nature because of their stability [1]. Recent studies have shown that transmitral vortex rings evolve in the LV during rapid early filling (E-wave) and late filling (A-wave) [2, 3]. These vortex rings help in improving blood transport through the ventricle towards the aorta, minimizing the loss of energy and preventing blood stagnation [1, 2, 4]. Moreover, patients with diastolic dysfunction have been shown to form different diastolic vortex rings compared to healthy volunteers [5-7]. This makes vortex ring analysis a promising tool for detection of diastolic blood flow abnormalities. Nevertheless, most of the reported studies are based on Computational Fluid Dynamics (CFD) simulations [1, 4] or Echocardiography [5, 6]. CFD simulations usually require simplifications of the anatomy (i.e. cardiac chambers) or boundary conditions, which might result in simulated blood flow velocities different from the actual flow. In echocardiography, generally only one single velocity component out of the three velocity components can be acquired providing limited flow velocity information.

Phase Contrast MRI (PC-MRI), also referred to as Velocity-Encoded MRI, can acquire all the three directional velocity components (in-plane and through-plane) of the blood flow relative to the three spatial dimensions and over the cardiac cycle, providing a powerful tool for cardiac flow analysis. In [7], Toger et al. used PC-MRI flow data to measure diastolic vortex ring volume using manual delineation of the vortex ring boundary from visualized Lagrangian coherent structures. They used the measured vortex volumes to differentiate between healthy volunteers and patients with dilated ischemic cardiomyopathy. In [8], Eriksson et al. proposed to quantify the intraventricular cardiac blood flow based on the visualization of PC-MRI data using pathline extraction, which allowed them to subdivide the intracardiac flow into four components based on their rates of passage relative to the cardiac cycle. In [9, 10] flow visualization techniques (e.g. particle tracing, streamlines, streaklines,...etc) for PC-MRI flow were used to qualitatively assess the aorta function. Nevertheless, in most of these studies, vortex rings were defined qualitatively using flow visualization techniques (e.g. as region of swirling pathlines or streamlines), which might suffer from observer bias or high cluttered data. In [11], ElBaz et al. used the lamb-

da2 method which is a quantitative method to define vortex rings. However, vortex rings were then extracted manually which is a tedious and time consuming process.

Due to the complex intra-cardiac blood flow, vortex rings are neither the only nor always the largest vortex object in the heart. Thus, using simple metrics (e.g. vortex size or location) is not enough to extract the LV vortex ring from surrounding vortex structures, similar in size, close in space, but different in shape. Furthermore, cardiac vortex rings are not ideally shaped rings but rather complex structures that tend to have a quasi-ring-like shape (Figure 6.1). All these factors make automatic vortex ring extraction from PC-MRI flow data a difficult and challenging task.

In this paper, we propose a novel method for automatic extraction of diastolic transmitral vortex rings from three-directional, three dimensional time resolved Phase Contrast MRI flow data during the rapid early (**E**) and late (**A**) filling phases. In the proposed work, we use a cardiac-vortex-specific shape signature to tackle the complex cardiac vortex shape and structure problems.

The proposed method consists of two parts. First, vortex structures are identified from the PC-MRI flow field using the Lambda2 method [12]. From this, a cardiac vortex ring signature is defined using the Laplace-Beltrami spectrum method [13]. Second, the cardiac vortex is extracted from the PC-MRI flow field by searching iteratively for the object with the best signature match relative to the reference signature. To the best of our knowledge, this work is the first attempt to extract vortex rings automatically from Phase Contrast MRI flow data in general and from the LV in particular.

6.2. Methodology

6.2.1. Vortex identification using the Lambda2 method

The first step towards vortex ring extraction is to identify vortex structures from the MRI flow field. To achieve this, we use the Lambda2 method [13] to detect vortex cores as it is considered the most accepted vortex identification technique [1]. Furthermore, the Lambda2 method is a quantitative detection method, i.e. it does not depend on visualization techniques but rather on the physical fluid dynamics definition of the vortex structure. The input for the Lambda2 method are the three velocity components of the velocity vector field. Let U, V and W denote the three velocity components of the flow field acquired using PC-MRI and X, Y, Z denote the three spatial dimensions. Then the Lambda2 method can be applied as follows. First, the velocity gradient tensor \mathbf{J} is computed as

$$\mathbf{J} = \begin{bmatrix} \frac{\partial u}{\partial x} & \frac{\partial u}{\partial y} & \frac{\partial u}{\partial z} \\ \frac{\partial v}{\partial x} & \frac{\partial v}{\partial y} & \frac{\partial v}{\partial z} \\ \frac{\partial w}{\partial x} & \frac{\partial w}{\partial y} & \frac{\partial w}{\partial z} \end{bmatrix} \quad (1)$$

Second, the tensor \mathbf{J} is decomposed into its symmetric part, the strain deformation tensor $\mathbf{S} = \frac{\mathbf{J} + \mathbf{J}^T}{2}$ and the antisymmetric part, the spin tensor $\mathbf{\Omega} = \frac{\mathbf{J} - \mathbf{J}^T}{2}$, where T is the transpose operation. Then, eigenvalue analysis is applied only on $\mathbf{S}^2 + \mathbf{\Omega}^2$. Finally, a voxel is labeled as part of a vortex core only if it has two negative eigenvalues i.e. if $\lambda_1, \lambda_2, \lambda_3$ are the eigenvalues whereas $\lambda_1 \geq \lambda_2 \geq \lambda_3$ then a voxel is labeled as vortex core if its $\lambda_2 < 0$. However, usually the velocity data is noisy, and as a result of which $\lambda_2 < 0$ gives cluttered results. Therefore, a λ_2 threshold, $T_{\lambda_2} < 0$, is applied instead to allow separation of strong vortex structures from weaker ones. Using the detected vortex voxels, a vortex structure is defined as connected region of these voxels. In this work, we used connected component analysis (CCA) [14] to define the connected vortex cores. The CCA performance is governed by the threshold T_{λ_2} i.e. it is important that T_{λ_2} results in separate vortex structures for CCA to be able to define them as separate objects. The Lambda2 method yields the vortex structures in the flow field. These vortex structures are usually visualized as isosurfaces with T_{λ_2} as the isovalue.

It is important to note that the Lambda2 method detects all vortex structures from the flow field i.e. vortex rings may be included in the extracted vortices but not all extracted vortices are vortex rings. The output of this step is converted to isosurfaces of the detected vortex structures from the PC-MRI flow field data (Figure 6.1). The vortex shape signature is subsequently captured by applying the Laplace-Beltrami method to these isosurface meshes.

6.2.2. Capturing Vortex Ring Shape Signature using Laplace-Beltrami Spectrum

From Figure 6.1, it is obvious that cardiac vortex rings are rather complex structures which tend to have a quasi-ring-like shape. Therefore, a method for extraction of cardiac vortex rings should capture the features specific for cardiac vortex rings. We achieve this by using the recently introduced Laplace-Beltrami spectral shape signature [13]. This spectral shape signature is a global shape signature computed only from the object's inherent geometry (e.g. curvature, surface area and volume). Furthermore, this signature can be used to compare objects independent of their representation, position and size. This signature is

defined as the beginning sequence of the Laplace-Beltrami (LB) differential operator. That is, for a given manifold M , if the LB operator is denoted by Δ , then the Laplacian eigenvalue equation can be written as :

$$\Delta f = -\lambda f \quad (2)$$

where λ is a real scalar value corresponding to the eigenvalue of the Laplacian Δ and f corresponds to its eigenvectors. The shape spectral signature is then defined as the diverging sequence of eigenvalues $0 < \lambda_1 \leq \lambda_2 \leq \lambda_3 \leq \dots + \infty$. This spectrum is truncated at the d th eigenvalue where d is application specific, and determined empirically. In our case, we apply the LB operator on the Lambda2 vortex isosurfaces which are discrete triangle meshes, hence, we solve (2) using a finite element method and apply the discrete Laplace-Beltrami (LB) operator and follow the same procedure as described in [13] to capture the LB spectrum for the vortex isosurface.

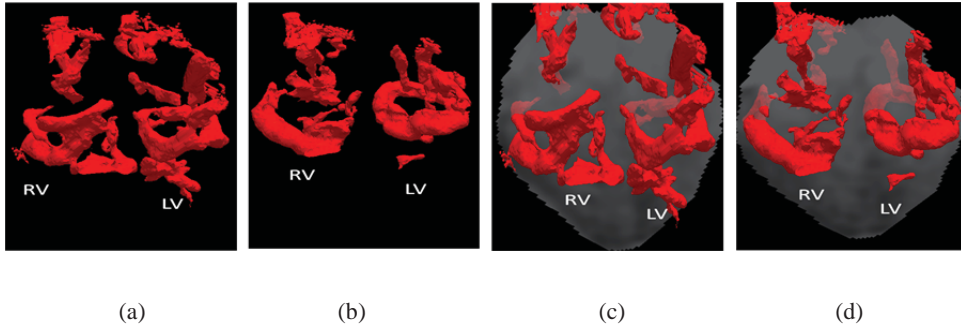


Figure 6.1. (a, b) Lambda2 isosurfaces of peak early filling (**E**) and late filling (**A**) phases respectively (c,d) their respective heart position in whole heart region of interest magnitude images.

Though similar, cardiac vortex rings differ between subjects. Therefore, we derive an averaged signature from multiple subjects using Laplace-Beltrami analysis as follows. First, for each training subject, the peak early filling (**E** phase) transmitral vortex ring isosurface is manually selected from the identified vortex structures. Second, for each extracted vortex, the Laplace-Beltrami signature is captured as described above. Then, every signature is normalized by both slope of its fitting line and the volume of the vortex isosurface (i.e. the number of voxels in the isosurface) [6]. The reason for this normalization is to make signatures scale invariant. Finally, signature average is computed. Through the rest of the paper we denote the computed vortex shape signature average by **VS**. Due to the repre-

sentation, position and size invariance properties of the LB signature [13], no shape registration is required prior to averaging. The steps for the vortex ring signature extraction from one subject are illustrated in Figure 6.2.

Of note, in addition to the **E**-phase averaged signature, we tested a signature trained on shapes of both phases (**E** and **A**) vortex rings. However, this provided identical results as for using only **E**-phase averaged signature.

6.2.3. Vortex Ring Extraction

The vortex ring extraction starts by identifying the vortex structures from the PC-MRI data using Lambda2 method as explained in section 6.2.1 Then, the normalized signature of each vortex object in the desired frame is captured using Laplace-Beltrami spectral shape analysis as explained in the previous section. For each vortex object in the current frame, its signature distance D_{sig} from the reference signature **VS** is computed as the L2 norm and computed as:

$$D_{sig}(m) = \sum (g_m - \mathbf{VS})^2, m=1 \dots M \quad (3)$$

with g_m being the m^{th} object signature and M the total number of vortex objects in the frame under processing. The extracted vortex ring is then defined as the vortex structure with the minimum D_{sig} .

6.3. Experiments

6.3.1. Data and Preprocessing

The proposed method was evaluated on a data from eight healthy volunteers (mean age: 40 ± 15 years) who underwent three-dimensional (3D), time resolved, three-directional Phase Contrast (VE) MR imaging at 1.5 T (Philips). VE MRI was performed in a 3D isotropic dataset of $4.2 \times 4.2 \times 4.2 \text{mm}^3$ covering all 4 cardiac chambers. Retrospective gating with 30 phases with average temporal resolution of 30 ms were reconstructed and velocity sensitivity of 150cm/s in all directions were used. This data was then linearly interpolated spatially to result in a 1mm^3 spatial resolution. The whole heart (not just the LV) region was then outlined manually from all slices and time frames. There are two reasons behind segmenting the whole heart region instead of just the LV. First, to investigate the ability of our method in extracting the LV vortex rings in the presence of other vortex structures formed in other ventricles. Second, to avoid the need for LV segmentation from

the PC-MRI magnitude images (Figure 6.1. b and d) which usually suffer from low contrast between LV and right ventricle (RV) boundaries making LV segmentation a difficult task.

6.3.2. Diastolic Vortex Ring Extraction

Using the manually segmented whole heart flow field volumes resulting from the previous step, vortex structures were identified using the Lambda2 method. After Applying threshold T_{λ_2} (as explained in Sec. 2.1), connected component analysis method (CCA) [14] was then applied to define the identified vortices as connected vortex objects. After that, LV vortex rings were labeled manually to be used as ground truth. In this work, for each subject, two observed rings were labeled from each of the rapid early (**E**) and late filling (**A**) diastolic phases. The two early filling rings correspond to the rings of the peak early filling PC-MRI phase and the subsequent frame. Similarly, the two late filling rings were labeled from the peak late filling phase and the subsequent frame. These were the frames in which vortex rings were observed consistently in all 8 subjects. From the eight volunteers, in total 32 LV vortex rings were manually labeled which then used as the ground truth to evaluate the proposed extraction method. For computing the Laplace-Beltrami (LB) signature [13], the vortex shape signature is captured from the Lambda2 isosurfaces with T_{λ_2} as isovalue.

To quantitatively evaluate the proposed method and to avoid bias in the selection of the average signature **VS**, a leave-one-out cross-validation approach was used. The average signature **VS** was computed from 7 subjects out of the available 8 subjects (i.e. computed as average of the corresponding 28 vortex signatures). This **VS** is then used to extract the LV vortex rings from the 4 aforementioned frames of the left out subject. This is repeated 8 times, leaving out different subjects. To evaluate the extraction performance we used the precision criterion, which was computed as the proportion $TP/(TP+FP)$ where TP stands for the true positive i.e. the number of correctly extracted LV vortex rings, FP for false positive i.e. the number of the mis-extracted LV vortex rings.

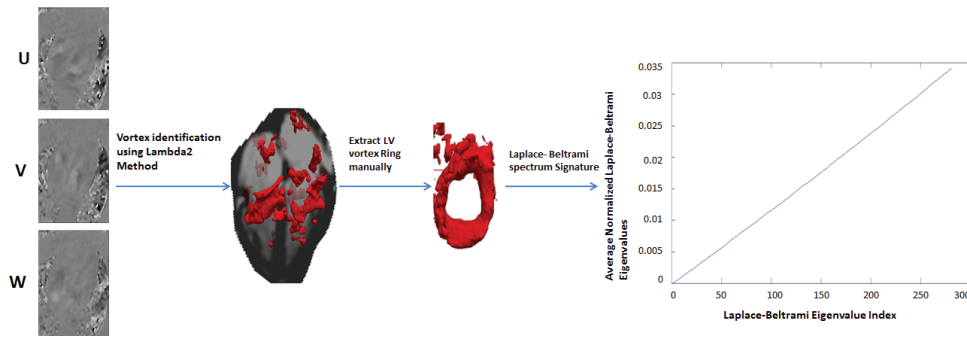


Figure 6.2. Steps of the proposed vortex ring shape signature extraction from one subject, U, V, W are three volumes representing the PC-MRI flow field velocity components.

6.3.3. Parameter selection

In the proposed method there are two empirically determined parameters, T_{λ_2} and d . T_{λ_2} is application and subject specific. In this study, T_{λ_2} was manually adjusted per subject until meaningful vortex rings could be differentiated from surrounding structures. In our experiments, T_{λ_2} in the range of $[2-5] \mu$ (with μ as the λ_2 average of voxels with $\lambda_2 < 0$) was found to give good results. Second, in the applied Laplace-Beltrami analysis, a signature of 300 eigenvalues (i.e. $d=300$) was sufficient in all experiments.

6.4. Results

The overall precision is 0.844, detailed results for the performance over the two diastolic phases are given in Table 6. 1, where every phase has a total of 16 LV transmitral vortex rings to be extracted. In the reported results, vortex rings were extracted from an average of 43 different sized surrounding vortex structures in the **E**-phases and an average of 30 structures in the **A**-diastolic phases. The proposed method failed in extracting only 5 rings, 1 from the **E** phase and 4 from **A**, out of the total 32 vortex rings.

Table 6. 1. LV Transmitral vortex ring extraction results

Phase	E (n=16)	A (n=16)	Total (n=32)
True Positive	15	12	27
False Positive	1	4	5

6.5. Discussion and Conclusion

Our results show that the proposed cardiac-vortex-specific signature based extraction is rather accurate in extracting LV diastolic transmitral vortex rings from whole heart PC-MRI with 27 successfully extracted LV vortex rings out of the total 32 rings yielding an overall precision of 0.844. In all 5 failed cases, the proposed algorithm extracted the RV C-shape or incomplete rings instead of the LV ring i.e. it was successful in ring extraction but could not differentiate between the RV partial rings and the more complete LV vortex rings. This could be due to the similarity in shape (e.g. curvature and complexity) of RV and LV vortex rings. Moreover, in all failed experiments, the LV vortex ring was ranked second after the RV partial ring based on the distance defined in Eqn.3 with a small difference of 0.16 ± 0.23 from the highest rank while the third ranking structure (not ring) was more distant (2.72 ± 1.90) from the highest ranking structure. It is important to note that the proposed **E**-phase trained average signature was able to detect most of the **A**-phase rings (12 out of 16), which shows the ability of the proposed method to deal with shape variability of the transmitral vortex rings between the **E** and **A** diastolic phases. The proposed method is automatic relative to the LV vortex ring extraction process. In this work, the whole heart region was still segmented manually from PC-MRI as automatic segmentation is out of this paper's focus. On the other hand, vortex identification is a complex fluid dynamics topic and no definite rigorous vortex definition is yet reached. In this work, we used the Lambda2 method which is the most commonly accepted fluid dynamics definition of a vortex [1]. Nevertheless, this method requires definition of T_{λ_2} threshold for defining meaningful vortex structures. To the best of our knowledge, no objective method has been reached yet for defining T_{λ_2} . Currently, we are working on developing a method for objective definition of this threshold. For the LB signature normalization, we evaluated different normalizations as suggested in [13], however, the best normalization in our case was to normalize by both the signature's fitting line slope and the vortex volume.

To our knowledge, this is the first attempt to automatically extract transmitral vortex rings from PC-MRI in general and from the LV in particular. Our results show that the proposed method is a promising technique for left ventricular vortex ring extraction. Furthermore, the results show the capability of the proposed method dealing with the vortex ring shape differences between the two diastolic (**E** and **A**) phases. As such, this work can be seen as a first step towards a quantitative understanding of cardiac vortex structures, their evolution and physiological implications. In addition, the proposed method could be used for vortex ring analysis in CFD simulations.

6.6. References

1. Kheradvar, A. and G. Pedrizzetti, Vortex formation in the cardiovascular system. 2012, Springer. p. 45-53.
2. Charonko, J.J., et al., Vortices formed on the mitral valve tips aid normal left ventricular filling. *Annals of biomedical engineering*, 2013. 41(5): p. 1049-1061.
3. Le, T.B. and F. Sotiropoulos, On the three-dimensional vortical structure of early diastolic flow in a patient-specific left ventricle. *European Journal of Mechanics-B/Fluids*, 2012. 35: p. 20-24.
4. Domenichini, F., G. Pedrizzetti, and B. Baccani, Three-dimensional filling flow into a model left ventricle. *Journal of fluid mechanics*, 2005. 539: p. 179-198.
5. Jiamsripong, P., et al., Impact of Acute Moderate Elevation in Left Ventricular Afterload on Diastolic Transmitral Flow Efficiency: Analysis by Vortex Formation Time. *Journal of the American Society of Echocardiography*, 2009. 22(4): p. 427-431.
6. Kheradvar, A., et al., Assessment of transmitral vortex formation in patients with diastolic dysfunction. *Journal of the American Society of Echocardiography*, 2012. 25(2): p. 220-227.
7. Töger, J., et al., Vortex ring formation in the left ventricle of the heart: analysis by 4D flow MRI and Lagrangian coherent structures. *Annals of biomedical engineering*, 2012. 40(12): p. 2652-2662.
8. Eriksson, J., et al., Semi-automatic quantification of 4D left ventricular blood flow. *J Cardiovasc Magn Reson*, 2010. 12(9): p. 12.
9. Markl, M., et al., Time-resolved three-dimensional magnetic resonance velocity mapping of aortic flow in healthy volunteers and patients after valve-sparing aortic root replacement. *The Journal of thoracic and cardiovascular surgery*, 2005. 130(2): p. 456-463.
10. Morbiducci, U., et al., In vivo quantification of helical blood flow in human aorta by time-resolved three-dimensional cine phase contrast magnetic resonance imaging. *Annals of biomedical engineering*, 2009. 37(3): p. 516-531.
11. ElBaz, M.S., et al., Quantification of diastolic vortex shape deformation in left ventricular filling from 4D flow MRI. *Journal of Cardiovascular Magnetic Resonance*, 2013. 15(Suppl 1): p. P79.
12. Jeong, J. and F. Hussain, On the identification of a vortex. *Journal of fluid mechanics*, 1995. 285: p. 69-94.
13. Reuter, M., F.-E. Wolter, and N. Peinecke, Laplace–Beltrami spectra as ‘Shape-DNA’ of surfaces and solids. *Computer-Aided Design*, 2006. 38(4): p. 342-366.
14. Haralock, R.M. and L.G. Shapiro, *Computer and robot vision*. 1991: Addison-Wesley Longman Publishing Co., Inc.

Chapter 7

Hierarchical Shape Distributions for Automatic Identification of 3D Diastolic Vortex Rings from 4D Flow MRI

This chapter was adapted from:

Elbaz, M. S., Lelieveldt, B. P., & van der Geest, R. J. (2015). **Hierarchical Shape Distributions for Automatic Identification of 3D Diastolic Vortex Rings from 4D Flow MRI**. In *Medical Image Computing and Computer-Assisted Intervention–MICCAI 2015* (pp. 467-475). Springer International Publishing.

Abstract

Vortex ring formation within the cardiac left ventricular (LV) blood flow has recently gained much interest as an efficient blood transportation mechanism and a potential early predictor of the chamber remodeling. In this work we propose a new method for automatic identification of vortex rings in the LV by means of 4D Flow MRI. The proposed method consists of three elements: 1) the 4D Flow MRI flow field is transformed into a 3D vortical scalar field using a well-established fluid dynamics-based vortex detection technique. 2) a shape signature of the cardiac vortex ring isosurface is derived from the probability distribution function of pairwise distances of randomly sampled points over the isosurface 3) a hierarchical clustering is then proposed to simultaneously identify the best isovalue that defines a vortex ring as well as the isosurface that corresponds to a vortex ring in the given vortical scalar field. The proposed method was evaluated in a datasets of 24 healthy controls as well as a dataset of 23 congenital heart disease patients. Results show great promise not only for vortex ring identification but also for allowing an objective quantification of vortex ring formation in the LV.

7.1. Introduction

A growing body of evidence [1-6] suggests a critical role of vortex ring formation within cardiac left ventricular blood flow during diastole as a significant contributor to efficient blood transportation [2] and as a potential clinical biomarker for early prediction of cardiac remodeling and diastolic dysfunction [4, 5]. A vortex is generally characterized by a swirling motion of a group of fluid elements around a common axis. Among different types of vortical flow structures, vortex rings are most abundant in nature due their stability [6]. In the LV, the asymmetrical redirection of blood flow through the LV results in the development of a vortex ring distal to the mitral valve (Figure 7.1) [1].

In fluid dynamics, different methods exist to define a vortex structure [7]. Most of these methods are based on a function of the velocity gradient tensor of the flow field. 4D Flow MRI enables non-invasive acquisition of the blood flow velocity field providing all three velocity components (in-plane and through-plane) over the three spatial dimensions and over the cardiac cycle [1]. Therefore, 4D Flow MRI provides all the flow field information needed for 3D vortex analysis [3].

A typical 3D vortex ring identification problem consists of three steps 1) convert the 3D velocity flow field into some 3D vortical scalar field in which a vortex is defined given some criteria; 2) manually (empirically) select an isovalue threshold that can define a vortex ring structure from the 3D vortical field. Given that different vortex structures may be present in the same flow field, the selected isovalue may result in multiple co-existing isosurfaces of other vortex structures in addition to the target vortex ring. 3) Manually identify the isosurface that corresponds to a vortex ring. It is obvious that manual isovalue selection and vortex ring selection can be time consuming and subjective. This may limit the applicability of a 3D vortex ring analysis in a clinical setup in which objective and reproducible analysis is crucial.

To our knowledge, there have been no studies on fully automatic identification of a vortex ring (i.e. both steps 2 and 3) from 4D Flow MRI. In our previous work [8], only the automatic identification of a vortex ring (step 3) was addressed using a spectral shape analysis [9]. However, this was based on the assumption that an isovalue was already pre-defined; therefore the problem of automatic isovalue selection has not been addressed. In addition, spectral shape analysis can be computationally intensive, hence may not be suitable for a multi-level search.

In this work, we propose a new method that simultaneously and automatically identifies the isovalue and the vortex ring isosurface. The proposed method has three ele-

ments: First, the flow field from peak inflow phase of 4D Flow MRI is converted into a 3D vortical scalar field using a well-established fluid-dynamics-based vortex identification method called the Lambda2 method [10]. Second, a reference shape signature defining the vortex ring isosurface is computed from a training set using D2 shape distributions [11]. Finally, simultaneous identification of isovalue and vortex ring is achieved using hierarchical clustering that allows for an iterative search for the best D2 shape distribution match with the reference signature. To evaluate the objectivity and generalizability of the proposed method in a clinical setup, the defined vortex ring was quantified using the method introduced in [3] in a dataset of 24 healthy controls as well as in a challenging dataset of 23 congenital heart disease patients who were previously reported to have abnormal diastolic inflow [12].

7.2. Methodology

7.2.1. 3D Vortical scalar field from 4D Flow MRI using the Lambda2 method

Among different fluid dynamics based vortex identification methods [7], the lambda2 (λ_2) method is considered the most accepted definition of a vortex [6]. The lambda2 method extracts vortex structures from the flow field by means of vortex-cores. The input for the Lambda2 method is the three velocity components of the velocity vector field and the output is a 3D scalar field in which each voxel is assigned a scalar value (λ_2). This scalar value can then be used to determine whether or not a voxel belongs to a vortex. For more formal definition, if U, V and F denote the three velocity components of the flow field acquired using 4D Flow and X, Y, Z denote the three spatial dimensions each of size $I \times J \times W$ with I as 4D Flow MRI's slice width, J as its height and W as the number of slices. Then the λ_2 method can be applied as follows. First, the velocity gradient tensor \mathbf{J} is computed. Second, the tensor \mathbf{J} is decomposed into its symmetric part, the strain deformation tensor $\mathbf{S} = \frac{\mathbf{J} + \mathbf{J}^T}{2}$ and the antisymmetric part, the spin tensor $\mathbf{\Omega} = \frac{\mathbf{J} - \mathbf{J}^T}{2}$, where T is the transpose operation. Then, eigenvalue analysis is applied only on $\mathbf{S}^2 + \mathbf{\Omega}^2$. Finally, a voxel is labeled as part of a vortex only if it has two negative eigenvalues i.e. if $\lambda_1, \lambda_2, \lambda_3$ are the eigenvalues whereas $\lambda_1 \geq \lambda_2 \geq \lambda_3$ then a voxel is labeled as vortex if its $\lambda_2 < 0$. Isosurfaces of a λ_2 isovalue threshold (T_{λ_2}) < 0 can be used to visualize different vortex structures in the flow field. A single T_{λ_2} isovalue can result in multi isosurfaces of different vortex structures among which a vortex ring may or may not be present. Different T_{λ_2} isovalues can be used to reveal different levels of details of vortices in the flow.

There are two outputs of this step. 1) A 3D volume denoted by $L_{i,j,w}$ where

$$L_{i,j,w} = \begin{cases} 0, & \text{if } \lambda_2(i,j,w) \geq 0 \\ \lambda_2(i,j,w) & \text{if } \lambda_2(i,j,w) < 0 \end{cases}, i = 1, \dots, I. j = 1, \dots, J. w = 1, \dots, W.$$

2) A 1D feature vector Q_d , $d = 1, \dots, P$ that stores all scalar values $L_{i,j,w} \neq 0$ (i.e. all possible T_{λ_2} thresholds). Q_d represents the isovalue feature vector. P represents the total number of scalar values $L_{i,j,w} \neq 0$.

Throughout the rest of the paper, the term vortex refers to a vortex core under the λ_2 definition explained above.

7.2.2. D2 Signature of Shape Distributions

The signature of shape distributions was first introduced in [11] for shape retrieval in computer vision tasks. The idea behind shape distributions' signature is to statistically encode a 3D model using a probability distribution of some parametric function that measures geometric properties of the given 3D model. This reduces the shape matching/retrieval problem into a simple distribution comparison [11]. D2 signature (Figure 7.1) is a shape distribution signature where the parametric function is defined by the Euclidean distances between randomly sampled pairs of points over the 3D surface. The D2 distribution can globally define the surface of interest (in our case, the vortex ring isosurface). Compared to other global shape signatures e.g. spectral signatures [9], the major advantage of the D2 distribution signature is its simplicity, essentially the shape matching problem is reduced to random sampling of points, histogram construction and finally histogram comparison using a dissimilarity metric.

Being a distribution, the D2-signature is invariant to rotation, translation and scaling (after normalization), therefore allowing matching of different shapes without the need for pre-registration or alignment. In addition, it is robust to small shape perturbations or deformations (e.g. due to noise) [11] which makes it sufficient for tasks that require multi shape comparisons as in our case.

In this work, the D2 signature is constructed following a similar procedure to that proposed in [11]: 1) Represent the 3D shape of interest as an isosurface. 2) Randomly sample N point pairs over the vortex-ring isosurface. $N=512^2$ pair of samples was used in this work. 3) Compute Euclidean distances between the N samples using L2-norm. 4) Construct a histogram of B bins of the pairwise distances. $B=100$ equally space bins was used in this work. 5) Normalize the resulting histogram using root mean square deviation. This step

makes the signature scale invariant. 6) Define a dissimilarity metric to be used for histogram matching with a new given 3D model. In this work we used the normalized L1-norm (normalized by L1 norm of the reference signature) as dissimilarity metric. Though similar, cardiac vortex rings differ between subjects. To account for this, we derive an average reference signature from a cohort of healthy subjects for matching purposes. Of note, increasing N and B more than the specified numbers did not yield significant improvement.

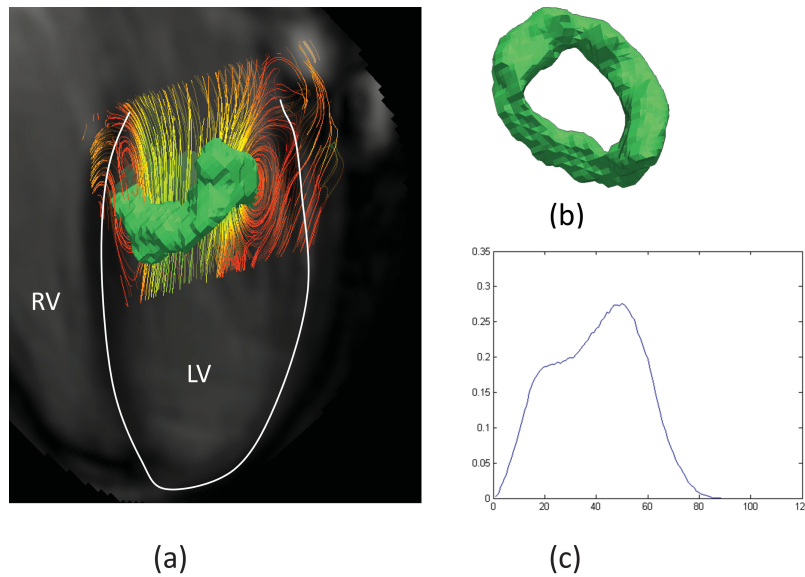


Figure 7.1. (a) A four chamber view showing the 3D vortex ring isosurface (in green) with superimposed streamlines in the LV at peak inflow phase in a sample healthy subject. (b) Separate view of the 3D vortex ring isosurface shown in (a). (c) The reference (average) D2 shape distributions' signature determined from the 24 healthy controls in this study.

7.2.3. Hierarchical shape distributions for vortex ring identification

In principle, the vortex ring isosurface may be defined by any isovalue in the Q_d feature vector. This can result in a large search space as multiple shape matching tasks are needed per each value to find the target isosurface. To reduce the search space, we propose to compress the isovalue feature vector into a subset of representative isovalues using the vector quantization technique [13]. Given a vector of features, the vector quantization process involves compression of the input set of points into a smaller set. This works by dividing the input vector into groups, each group is then defined by one value given some crite-

ria [13]. The well-known K-means clustering algorithm is a vector quantization method [13] in which a long input feature vector can be compressed into a vector of K cluster centroids that minimize the within-cluster sum of square distances.

In this work, we use an iterative hierarchical K-means scheme in which there is no need to predefine the number of centroids K. This allows avoiding the possible bias when K is predefined. The proposed scheme is as follows: Given the isovalue feature vector Q_d , initialize with $K=1$ and apply the K-means clustering algorithm (i.e. Q_d feature vector is reduced to a single candidate isovalue). Then, K is iteratively incremented by one until convergence or a predefined stopping criterion is satisfied. This results in a hierarchical multi-level vector $V^{r,k}$, in which each level $k = 1, \dots, P$ carries $r = 1, \dots, k$ candidate isovalues.

Given an isovalue level k , each isovalue $V^{r,k}$ can define $U_t^{r,k}, t = 1, \dots, E$ isosurfaces of different vortex structures from among them a vortex ring may or may not be present. Therefore, to identify the vortex ring isosurface we need to solve two problems. 1) Find the isovalue $V^{r,k}$ in which a vortex ring is one of its E resulting isosurfaces. 2) Find the isosurface $U_t^{r,k}$ that corresponds to a vortex ring.

Using the proposed hierarchical vector quantization scheme and the reference D2 shape distribution signature, we are able to simultaneously solve these two problems by minimizing the shape distribution distances as follows: for each isovalue $V^{r,k}$ at level k , extract the corresponding $U_t^{r,k}$ vortex isosurfaces. Then, for each isosurface $U_t^{r,k}$, construct the D2 shape distribution following the procedure explained above. Compute the dissimilarity distance $d_t^{r,k}$ with the reference signature using the normalized L1 norm (i.e. normalized by the L1-norm of the reference signature). Repeat this for every isovalue level until convergence ($d_t^{r,k} < \epsilon$) or stopping criteria is satisfied. We wish to identify the best surface match by finding the indices \hat{r}, \hat{k} and \hat{t} such that

$$\{\hat{r}, \hat{k}, \hat{t}\} = \underset{r,k,t}{\operatorname{argmin}} d$$

As a result, the target two problems are simultaneously solved by defining the isosurface $U_{\hat{t}}^{\hat{r},\hat{k}}$ as the target vortex ring isosurface and corresponding isovalue $V^{\hat{r},\hat{k}}$ as the target isovalue. To avoid local minima, for each iteration, the K-means algorithm was replicated T times ($T = 10$ was used in this work) using different initial centroids. Then, the centroids with minimum within-cluster sums of point-to-centroid distances were chosen. Two stop criteria were defined 1) reaching a maximum number of predefined iterations (set to 50 in

this work). In all our experiments, less than 15 iterations were enough to find $\{\hat{r}, \hat{k}, \hat{t}\}$, and 2) the dissimilarity distance was increasing for three consecutive iterations. This decreases the possibility of stopping at local minima when only a single diverging iteration is used instead.

7.2.4. Quantitative characterization of the identified vortex ring in the LV

After the identification of the vortex ring isosurface, it was quantified using the parameters proposed in [3]. These parameters are the vortex ring orientation and normalized cylindrical (Circumferential (C), Longitudinal (L) and Radial(R)) 3D position of the vortex ring center relative to the LV. L and R were normalized relative to the LV long-axis length and the radius of the LV endocardial cavity, respectively. Vortex orientation is defined as the angle between the LV long axis and the fitting plane of the vortex isosurface.

7.3. Dataset, preprocessing and validation

We evaluated the proposed method on two datasets: one dataset of 24 healthy controls (mean age: 21 ± 10 years) as previously described in [3] and a dataset of 23 patients (27 ± 11) after atrioventricular septal defect correction. All subjects underwent retrospectively-gated 4D Flow MRI at 3.0 T (Philips) with spatial resolution of 3-4 mm³ and a temporal resolution of ~ 30 ms covering all 4 chambers of the heart. This data was then linearly interpolated spatially to result in a 1mm³ spatial resolution. More details on the acquisition parameters can be found in [3].

To localize the LV ROI, the LV was manually segmented from only the peak-inflow diastolic phase in the 4D Flow volume as explained in [3]. As the vortex ring is a connected region of voxels within the LV, accurate segmentation is not required for the purpose of vortex ring identification. Only rough over-segmentation of the LV (to ensure the LV is covered) was enough to roughly define the LV ROI. In this work, an over-segmentation of about 0.5 cm around LV border was used to define LV ROI.

To generate the ground truth for the vortex ring isosurface in the two included datasets, for the healthy control dataset, we used the vortex ring isosurfaces interactively generated with low inter and intra observer variability in a previously validated workflow [3]. Same procedure in [3] was used to blindly generate the ground truth for patient dataset. To quantitatively evaluate the performance of the proposed method in the first dataset of healthy controls, leave-one-out cross-validation was used to avoid bias in the selection of the reference averaged D2 signature.

To test the generalization performance in a clinical setting, the dataset of 23 patients was evaluated using a reference signature derived only from the 24 healthy control subjects. To evaluate the identification performance relative to the ground truth, we performed two sets of evaluations. The accuracy of the identified isosurface object was assessed using the Hausdorff distance and dice coefficient for surface overlap. In addition, a paired student's t-test comparison of the automatically defined isovalues and the one used to generate the ground truth isosurfaces was performed. Second, paired student's t-test was used to statistically compare the quantitative vortex ring parameters of the automatically identified vortex-ring isosurfaces to those of the ground truth. For all statistical tests a p-value <0.05 was considered significant.

7.4. Results

In all subjects of both datasets, a vortex ring isosurface was successfully identified from the Lambda2 scalar field with qualitatively similar shape to that of the ground truth (Figure 7.2). Detailed results of the quantitative evaluation over the two datasets is given in Table 7.1 where a Hausdorff distance of 8.36 ± 7.55 mm in healthy control dataset and 11.73 ± 6.57 mm in the patients dataset were found. The surface overlap (dice coefficient) was 0.81 ± 0.09 in controls and 0.77 ± 0.14 in patients. The identified isovalues using the proposed method were highly comparable to those of the ground truth and not statistically different ($p=0.86$). Quantitative parameters of the automatically identified vortex rings were in good agreement with the ground truth.

7.5. Discussion and conclusion

This paper presents a framework for objective identification and quantification of 3D vortex ring in the LV from 4D PC MRI by means of isosurfaces. The problem of vortex ring identification from the 3D vortical scalar field was reduced to histogram comparison and hierarchical K-means vector quantization. The reported results on healthy controls as well as patients show great promise of the proposed method. The generalizability of the proposed method was evaluated with abnormal vortex rings being identified from 23 patients with a signature trained solely on normal vortex ring isosurfaces from healthy controls.

Table 7.1. Qunatitative evaluation results

Parameter	24 Controls			23 Patients		
	Ground truth	Proposed method	p-value (paired t-test)	Ground truth	Proposed method	p-value (paired t-test)
C	87±20	85±24	0.12	67±19	63±23	0.07
L	0.19±0.04	0.19±0.04	0.92	0.22±0.06	0.22±0.05	0.74
R	0.27±0.07	0.27±0.07	0.91	0.33±0.09	0.33±0.1	0.61
Vortex Orientation	70±55	65±54	0.65	57±25	57±40	0.87
Lambda2 Isovalue*	-7.2±3.43	-7.3±3.2	0.82	-7.27±11.24	-7.7±5.45	0.86
Surface Overlap (Dice Coeffecient)	0.81±0.09			0.77±0.14		
Hausdorff distance (mm)	8.36±7.55			11.73±6.57		

*The absolute lambda2 isovalue does not have direct interpretation here and was provided only to give impression on how similar were they in test cases compared to ground truth

The proposed method provided high performance and agreement with the blindly generated ground truth. It is important to emphasize that the exact size/volume of a vortex ring is generally undefined as it is isovalue dependent. Therefore, volumetric measurements like Hausdorff distance or dice overlap may not sufficiently capture the validity of the identified vortex rings. Instead, the evaluated quantitative characterization parameters (C, L, R and orientation) may provide more objective evaluation of the method and its potential clinical value. In this work, the vortex ring identification was limited to the phase of peak LV inflow which is considered the moment around full vortex development [3, 6], however vortex formation in the LV is a dynamic process over the entire diastole involving vortex evolution and dissipation with corresponding shape deformations. Future work will address the method's performance in other diastolic phases. The proposed method allows for objective quantitative characterization of the peak-inflow vortex ring formation in the LV with results comparable to those previously validated [3]. With the increasing interest in vortex ring formation as a potential biomarker for LV (dys)function [2, 4, 6], the proposed method can play an important role in providing objective 3D vortex analysis for assessment of vortex ring formation in the LV from 4D Flow MRI.

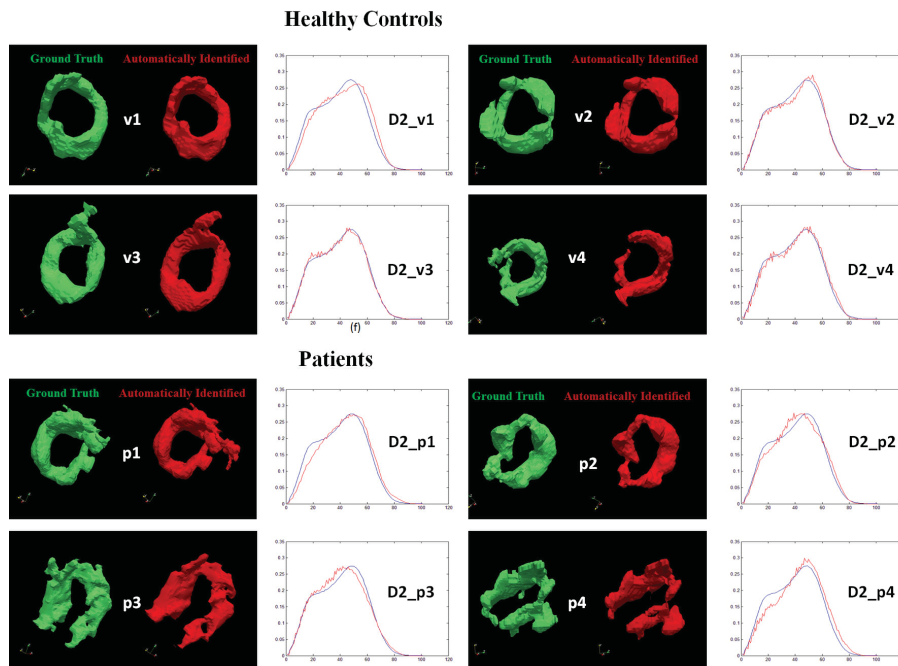


Figure 7. 2. Sample results of the proposed method on 4 healthy controls (top two rows: v1 to v4) and 4 patients (bottom two rows: p1 to p4). For every subject, the ground truth is presented on left (green) and the automatically identified peak-inflow vortex ring isosurface on right (red). D2_v1 to D2_v4 and D2_p1 to D2_p4 show the best matched D2 distributions corresponded to the automatically identified vortex ring isosurface (red curve) overlaid on the reference signature (average over healthy controls) in blue.

7.6. References

1. Kilner, P.J., et al., Asymmetric redirection of flow through the heart. *Nature*, 2000. 404(6779): p. 759-761.
2. Martinez-Legazpi, P., et al., Contribution of the Diastolic Vortex Ring to Left Ventricular Filling. *Journal of the American College of Cardiology*, 2014. 64(16): p. 1711-1721.
3. Elbaz, M.S., et al., Vortex flow during early and late left ventricular filling in normal subjects: quantitative characterization using retrospectively-gated 4D flow cardiovascular magnetic resonance and three-dimensional vortex core analysis. *Journal of Cardiovascular Magnetic Resonance*, 2014. 16(1): p. 78.
4. Pedrizzetti, G., et al., The vortex-an early predictor of cardiovascular outcome? *Nature Reviews Cardiology*, 2014. 11(9): p. 545-553.
5. Gharib, M., et al., Optimal vortex formation as an index of cardiac health. *Proceedings of the National Academy of Sciences*, 2006. 103(16): p. 6305-6308.
6. Kheradvar, A. and G. Pedrizzetti, *Vortex formation in the cardiovascular system*. 2012, Springer. p. 45-53.
7. Jiang, M., R. Machiraju, and D. Thompson, *Detection and Visualization of Vortices*. *The Visualization Handbook*, 2005: p. 295.

8. ElBaz, M.S., et al., Automatic extraction of the 3D left ventricular diastolic transmitral vortex ring from 3D whole-heart phase contrast MRI using Laplace-Beltrami signatures, in *Statistical Atlases and Computational Models of the Heart. Imaging and Modelling Challenges*. 2014, Springer. p. 204-211.
9. Reuter, M., F.-E. Wolter, and N. Peinecke, Laplace–Beltrami spectra as ‘Shape-DNA’ of surfaces and solids. *Computer-Aided Design*, 2006. 38(4): p. 342-366.
10. Jeong, J. and F. Hussain, On the identification of a vortex. *Journal of fluid mechanics*, 1995. 285: p. 69-94.
11. Osada, R., et al., Shape distributions. *ACM Transactions on Graphics (TOG)*, 2002. 21(4): p. 807-832.
12. Calkoen, E.E., et al., Characterization and improved quantification of left ventricular inflow using streamline visualization with 4DFlow MRI in healthy controls and patients after atrioventricular septal defect correction. *Journal of Magnetic Resonance Imaging*, 2014.
13. Gersho, A. and R.M. Gray, Vector quantization and signal compression. Vol. 159. 2012: Springer Science & Business Media.

Chapter 8

Summary, Discussion and Future Perspectives

8.1. Summary

The methods presented in this thesis enable quantitative characterization, evaluation and automatic identification of in-vivo 3D intra-cardiac vortex flow patterns in the human heart, specifically through utilization of in-vivo 4D Flow MRI. These methods show the feasibility and expand the potential of 4D Flow MRI towards objective in-vivo evaluation of 3D intra-cardiac vortex flow, noninvasive assessment of intra-cardiac viscous energy loss and of their association in healthy subjects and patients with altered intra-cardiac flow. Different aspects of in-vivo 3D intra-cardiac vortex flow analysis, from 4D Flow MRI, in healthy subjects and cardiac patients were addressed in this thesis.

In **Chapter 2**, a semi-automatic workflow was introduced for identification of 3D left ventricular (LV) vortex ring flow from 4D Flow MRI during diastole. This workflow is based on instantaneous Eulerian 3D vortex core identification using a fluid dynamics-based method called the Lambda2 method. The developed workflow was then used to characterize the 3D vortex ring flow and its evolution during early and late diastolic filling in twenty-four healthy human volunteers who all underwent 4D flow MRI. Reported results revealed the formation of two distinct 3D vortex rings during LV diastole: an early filling vortex ring and a late filling vortex ring. Standardized quantitative parameters were derived to quantitatively characterize vortex ring shape and location (3D position and orientation) relative to the LV geometry at the moments of peak early filling (E-vortex) and peak late filling (A-vortex). We provided quantitative normal ranges of E- and A- 3D vortex rings from the studied healthy volunteers. Both the E- and A-vortex rings were formed at the basal level, but with E-vortex ring center being significantly closer to the mitral valve annulus compared to the A-vortex ring. E- and A-vortex rings were similarly oriented relative to the LV. E-vortex ring shape was significantly more circular compared to a more elliptical A-vortex ring. A strong correlation was found between vortex ring shape and the inflow shape through the mitral annulus and leaflet tips.

In **Chapter 3**, after characterizing and revealing 3D diastolic LV vortex ring formation in healthy cases, the impact of altered inflow and abnormal mitral valve morphology on 3D LV vortex ring formation was studied in patients who are known to develop altered inflow and mitral valve morphology. The workflow and quantitative characterization developed in **Chapter 2** were applied on thirty healthy controls and thirty-two patients who previously underwent a surgical repair to correct a congenital atrioventricular septal defect. Vortex formation time (VFT) was computed in all studied

subject. Results showed altered 3D LV inflow vortex ring formation in patients compared to healthy controls. This alteration was characterized by a more frequent absence of a (well-formed) ring-shaped vortex (a complex irregular vortex flow was detected instead), more oblique vortex ring orientation and 3D position closer to the lateral wall in the patients who presented a vortex ring compared to healthy controls at moments of peak early and peak late filling. Patients with absent (well-formed) E-vortex ring showed significantly higher VFT compared to healthy controls. Three patients showed a reversed E-vortex ring orientation with the vortex's lateral side being positioned towards the apex in contrast to healthy controls in which the septal side was the apically positioned side. Detected 3D vortex rings in patients were more elliptical in shape compared to healthy controls which could be a reflection of the restricted inflow area found in patients.

In **Chapter 4**, the influence of the disturbed 3D inflow vortex ring parameters found in patients (**Chapter 3**) on LV physiology is studied by means of its association with viscous energy loss levels in the LV during diastole. Using Navier-Stokes energy equations, instantaneous 3D viscous energy loss in the LV was non-invasively evaluated from the 4D Flow MRI derived velocity field over diastole in the previously studied population of thirty volunteers and thirty-two patients (**Chapter 2 and 3**). Association between viscous energy loss levels and previously derived 3D vortex ring parameters (orientation and 3D position) was assessed during both early and late diastolic filling as well as over complete diastole. Normal ranges of viscous energy loss and 3D vortex parameters were derived from the healthy volunteers as the 95% confidence interval. Patients with vortex ring parameters beyond the normal range showed significant elevation in viscous energy loss compared to healthy volunteers. Highest viscous energy loss was found in patients with absent (well-formed) E-vortex ring, and patients with reversed E-vortex ring orientation (on average more than double the viscous energy loss levels measured in the rest of patients). As such, this was the first in-vivo study to confirm the role of normal 3D vortex ring formation on minimization of viscous energy loss using 4D Flow MRI.

In **Chapter 5**, systolic Left Atrial (LA) vortex flow is evaluated in healthy volunteers and patients with corrected congenital atrioventricular septum defect (AVSD) with both none-mild and moderate left atrioventricular valve (LAVV) regurgitation. Atrial vortex flow was identified using streamline visualization and 3D vortex core analysis (using the Lambda2-method) around the moment of LV-systole. Backward particle tracing with particles seeded from within the identified 3D vortex core was used to identify the

origin of atrial vortex flow. Accordingly, the atrial vortex flow was decomposed into four components based on origin: 1) flow originating from left pulmonary vein (LPV) 2) flow originating from right pulmonary vein (RPV) 3) residual atrial flow or 4) a regurgitant flow originating from LV. Results show that in both healthy volunteers and patients, the majority of atrial vortex flow originates from the LPV. However, patients showed a significant decrease in LPV vortex flow and significant increase in residual atrial vortex flow. Compared to a single recirculating atrial flow region detected in healthy volunteers, patients showed disturbed atrial vortex flow with multiple regions of recirculating flow structures around the regurgitation jet and with opposed circulating directions.

In **Chapter 6**, a method is proposed for automatic extraction of 3D LV vortex ring core isosurfaces (by means of Lambda2 vortex cores) of peak E- and peak A-filling phases from whole-heart 4D Flow MRI. The proposed method is based on capturing the intrinsic global shape features of the cardiac vortex ring isosurface using the Laplace-Beltrami (LB) spectral shape signature. The LB signature is defined as the diverging eigenvalues sequence of the Laplace-Beltrami differential operator. This LB sequence encodes the discriminating shape features that are intrinsic to the shape of interest. In this work, an LB reference signature of the LV vortex ring shape is derived from a training set of LV vortex ring isosurfaces of healthy volunteers. In the extraction phase, the trained reference signature is used to iteratively search for the LV vortex ring object (isosurface) among co-existing vortex objects. The target vortex ring object is defined as the isosurface that gives best LB-signature match with the trained reference signature. This method has been evaluated in a dataset of eight healthy volunteers using leave-one-out cross validation yielding a precision of 84%. However, one limitation of this work is that it expects the input to be multiple isolated isosurface objects, among them is the target vortex ring isosurface to be extracted. This requires prior definition of the isovalue that produces such a well-defined vortex ring that is isolated from other co-existing vortex objects. In this work, isovalue selection was done empirically based on manual interaction. Selection of appropriate isovalue may require experience and can be a tedious and subjective process.

In **Chapter 7**, to overcome the aforementioned limitations of the method in **Chapter 6**, a new method is proposed for automatic identification of the 3D vortex ring core isosurface from 4D Flow MRI flow field without any presumptions on the isovalue selection. In fact, the proposed method allows simultaneous automatic identification of both the best appropriate isovalue and the object corresponding to the vortex ring isosurface. First, the 4D Flow MRI velocity field is converted into a vortex core scalar field

using the fluid-dynamics-based Lambda2 method. Second, a vortex shape signature is derived from a training set of healthy subjects by means of shape distributions: probability distribution of pairwise Euclidean distances of randomly sampled points on the vortex ring isosurface. This derived shape distribution is used as a reference signature defining the shape of the vortex ring isosurface. Finally, a hierarchical vector quantization algorithm is proposed to simultaneously define the best appropriate isovalue and to identify the vortex ring isosurface among co-existing vortex isosurfaces. The method was evaluated qualitatively and quantitatively in two cohorts: a cohort of twenty-four healthy volunteers and a cohort of twenty-three congenital heart disease patients. Results of performed experiments showed excellent performance and good agreement with blindly generated ground truth as well as generalizability to challenging abnormal vortex rings in patients. As such, the proposed method is a step forward towards allowing objective automatic 3D vortex ring analysis from 4D Flow MRI in clinical practice.

8.2. Discussion and Future perspectives

The aims of this thesis as stated in chapter 1 were accomplished. Nevertheless, this thesis can serve as a ground for further work. In this thesis, we have identified and qualitatively characterized the 3D vortex ring formation and its evolution over complete diastole (**Chapter 2**). However, 3D vortex ring quantification (**Chapter 2, 3, 4**) and automatic identification (**Chapter 6, 7**) were mainly limited to only peak early and peak late filling phases which are considered the moments around full vortex ring development. Nevertheless, as shown in **Chapter 2**, 3D cardiac vortex flow is a dynamic process that involves development, propagation, interaction with chamber wall and subsequent decay. These dynamics were not fully quantified in this thesis. A potential mechanism of vortex flow in cardiac (dys)function is more likely to be evident in the vortex evolution process. Future work should be aimed at quantifying this evolution and its relation to cardiac (dys)function.

The main focus of this thesis was inflow vortex flow formation in the LV during diastole and LA during systole. In principle, the vortex identification and energy evaluation methods developed in this thesis (**Chapter 2, 4, 6, 7**) are generally applicable to analysis of other blood flow regions in the cardiovascular system from 4D Flow MRI. An example of this was shown in **Chapter 5**, where 3D atrial vortex identification was successfully performed using methods and workflow originally developed for LV vortex analysis (**Chapter 2**). In the future, we plan to employ the 3D vortex and energy methods developed

in this thesis to expand the analysis into other cardiac chambers (e.g. right ventricle, right atrium), as well as great arteries, such as aorta, and over the complete cardiac cycle. Such comprehensive analysis would provide more insights into the normal physiology of the heart and potential connection or alteration in cardiovascular patients.

Eulerian vortex core analysis using the fluid dynamics-based Lambda2 method was the main method used in this thesis for extracting and identifying instantaneous 3D vortex core regions from 4D Flow MRI. A limitation of instantaneous (Eulerian) vortex core identification methods is that, in practice, they require a threshold (isovalue) to be defined (mainly manually) to identify meaningful vortex core regions. The fact that different thresholds might result in different 3D vortex volumes makes it challenging to derive reliable volumetric measurements (e.g. vortex volume, total strength or total energy) based on such vortex core analysis. This becomes more evident when the input velocity field is typically noisy and with coarse resolution as the case with 4D Flow MRI. That is the main reason why volumetric vortex measurements were largely avoided in this thesis.

A solution to the threshold selection problem was approached in **Chapter 7**, by automatic identification of appropriate threshold (isovalue). This could be a step forward towards an objective identification of vortex core volume. Further studies are still needed to evaluate the accuracy of such method for vortex volume quantification. On the other hand, Lagrangian vortex identification methods, such as Lagrangian Coherent Structures (LCS), might allow quantification of total vortex ring volume over a period of time, but are generally not meant for instantaneous vortex flow analysis (i.e. not to quantify vortex volumes at specific time points). Therefore, they do not directly aim at analyzing the evolution of instantaneous vortex flow. In the future, different vortex identification methods; including Eulerian and Lagrangian, methods should be investigated in a manner that allows accurate and objective analysis of the evolution of instantaneous 3D vortex flow volumes.

4D Flow MRI is a state-of-the-art in-vivo flow imaging technique and the only modality that allows in-vivo acquisition of 4D flow data of all three velocity components. Nonetheless, 4D Flow MRI has some limitations. Typical long acquisition times (up to 20 minutes) may limit the clinical feasibility. However, applying recent scan acceleration techniques enable more feasible acquisition durations (~10 minutes when no respiratory gating is applied) and this is expected to further improve in the future. Given the slow MR acquisition, 4D Flow MRI requires acquisition over multiple cardiac cycles. This results in acquiring mainly the average flow field while smoothing out turbulent fluctuations or

potential higher order flow components. This has to be taken in consideration when computing and/or interpreting 4D Flow MRI measurements including vortex flow and energetics. The need to heuristically determine an appropriate velocity sensitivity encoding (VENC) prior to 4D Flow MRI acquisition to avoid potential aliasing artifact can be challenging. The acquired 4D Flow MRI flow field may present errors in the form of eddy current effects, Maxwell terms, signal noise, and/or velocity offsets. These errors should be corrected using appropriate techniques before processing/interpreting flow data. Coarse temporal ($\sim 30\text{-}50$ ms) and spatial resolutions ($\sim 3\times 3\times 3$ mm³) of 4D Flow MRI limits flow analysis to the large scale flow structures with life-span longer than the acquired temporal resolution. All these factors may limit the reliability of 4D Flow MRI-based results and subsequent interpretations.

To allow reliable and correct interpretations of 4D Flow MRI measurements, it is important to evaluate and validate such results. A limiting factor in such validation is the lack of a realistic gold standard (ground-truth) of the in-vivo human cardiovascular flow in general, and vortex flow and energetics in particular. Available phantom techniques are not able to provide such realistic gold standard. One way to tackle this issue in future studies could be to benefit from the advances in computational fluid dynamics (CFD) by building hybrid CFD-4D Flow MRI computational systems that impose realistic in-vivo flow field measurements (not only geometry) from 4D Flow MRI to guide high resolution, more controllable and robust, CFD simulations to reach a realistic high resolution model of human cardiac flow field.

While many studies have speculated on a role of vortex flow formation on optimizing cardiac function and/or a connection with cardiac abnormalities, there is a lack of studies evaluating such assumptions in-vivo using a true and complete flow field. In **Chapter 4**, using 4D Flow MRI flow fields, we have in-vivo evaluated and confirmed the previously speculated, but unverified, role of vortex flow on minimization of energy loss. More (follow-up) studies of different groups of cardiovascular patients are needed to assess the true association between vortex flow patterns and cardiac (dys)function and to determine whether vortex flow could serve as a biomarker, or whether it is only a byproduct of other factors. In fact, the normal cardiac hemodynamics are largely unexplored and therefore still mostly unknown. While currently underestimated in the community, it is critical to carry out more studies aiming at revealing, at a comprehensive level, the normal hemodynamics of the cardiovascular system before jumping into patient evaluations.

This thesis shows the potential of 3D/4D vortex flow analysis and viscous energy loss measurements from 4D Flow MRI in revealing and evaluating in-vivo intra-cardiac hemodynamics. It is critical to ensure reliability and reproducibility of such measurements and analysis to allow sound clinical interpretations. A sophisticated vortex flow analysis needs to be accessible for clinical personnel with minimal needs of technical background. An important mechanism to achieve this would be to continue working on building automatic reliable systems for identification and quantification of cardiac hemodynamics in general and vortex flow and energetics in particular from 4D Flow MRI.

Samenvatting en conclusies

8.1. Samenvatting

Met de methodieken die in dit proefschrift worden beschreven, kunnen in-vivo 3D vortex (wervel) flowpatronen in het menselijk hart kwantitatief worden gekarakteriseerd, geëvalueerd en automatisch worden geïdentificeerd, met name door gebruik van in-vivo 4D Flow MRI. Deze methodieken tonen de uitvoerbaarheid van 4D Flow MRI aan en verbreden de potentie ervan in de richting van een objectieve in-vivo evaluatie van 3D intra-cardiale vortexstroming, non-invasieve bepaling van intra-cardiaal viskeus energieverlies en de onderlinge associatie hiervan in gezonde personen en patiënten met een veranderd intra-cardiale bloedstroming. In dit proefschrift worden verschillende aspecten van in-vivo 3D intra-cardiale vortex flow analyse, middels 4D Flow MRI, in gezonde personen en cardiale patiënten behandeld.

In **Hoofdstuk 2** werd een half-automatische methode geïntroduceerd waarmee 3D vortexringstructuren met 4D Flow MRI kunnen worden geïdentificeerd in de bloedstromingspatronen in het linker ventrikel (LV) tijdens diastole. Deze methode is gebaseerd op de instantane Euleriaanse 3D vortexkernidentificatie waarbij een methode uit de stromingsleer wordt toegepast, de zogenaamde Lambda2 methode. De ontwikkelde methode werd vervolgens toegepast om 3D vortexringstructuren en de ontwikkeling ervan te karakteriseren tijdens vroege en late diastolische vulling in vierentwintig gezonde vrijwilligers die allen 4D Flow MRI ondergingen. De resultaten lieten zien dat er twee 3D vortexringstructuren ontstaan en onderscheiden kunnen worden tijdens LV diastole: een vortexring tijdens de vroege diastolische vullingsfase en een tijdens late vulling. Gestandaardiseerde kwantitatieve parameters werden bepaald om de vortexringstructuur kwantitatief te karakteriseren en de locatie (3D positie en oriëntatie) ervan ten opzichte van de geometrie van het LV op de momenten van piek-vroege vulling (E-vortex) en piek-late vulling (A-vortex). We verschaften het kwantitatieve bereik van normaalwaarden voor 3D E- en A-vortexringstructuren, bepaald middels de onderzochte gezonde vrijwilligers. Beide E- en A-vortexringen ontstonden op het basale niveau, maar met het centrum van de E-vortexring significant dichterbij de annulus van de mitralisklep dan dat van de A-vortexring. E- en A-vortexring waren overeenkomstig in oriëntatie ten opzichte van het LV. De E-vortexring was significant meer circulair ten opzichte van de meer ellipsvormige A-vortexring. Een sterke correlatie werd gevonden tussen de vorm van de vortexring en de vorm van de instroming door de annulus van de mitralisklep en de uiteinden van de klepbladen.

Na het karakteriseren en het onthullen van 3D diastolische LV vortexringformatie in gezonde vrijwilligers wordt in **Hoofdstuk 3** de impact die de gewijzigde instroming van bloed en een abnormale mitralisklepmorfologie heeft op de vorming van een 3D LV vortexring onderzocht bij patiënten van wie bekend is dat de instroming en mitralisklepmorfologie afwijkend ontwikkelen. De methode en de kwantitatieve karakterisering die in **Hoofdstuk 2** is ontwikkeld, werden toegepast op dertig gezonde controlepersonen en tweeëndertig patiënten die eerder een chirurgische correctie van een aangeboren atrioventriculair septum defect ondergingen. Vortexformatietijd (VFT) werd berekend in alle onderzochte personen. De resultaten toonden een veranderde 3D LV vortexringvorming bij patiënten aan vergeleken met gezonde controlepersonen. Deze verandering werd gekenmerkt door een vaak ontbrekende (goed ontwikkelde) ringvormige vortex (in plaats daarvan werd een complex onregelmatige vortexstroming gedetecteerd), en bij die patiënten waarbij een vortexring kon worden gedetecteerd, een schuinere oriëntatie van de vortexring en een 3D positie die dicht bij de laterale wand was in vergelijking met gezonde controlepersonen op de momenten van piek vroege en late vulling. Patiënten waarbij een goed-ontwikkelde E-vortexring ontbrak, hadden een significant hogere VFT in vergelijking met gezonde controlepersonen. Drie patiënten vertoonden een omgekeerde oriëntatie van de E-vortexring waarbij de laterale zijde van de vortex naar de apex gepositioneerd was in tegenstelling tot de oriëntatie bij de gezonde controlepersonen waarbij de septale zijde van de vortex het meest apicaal georiënteerd was. Bij patiënten waren de 3D vortexringen meer elliptisch van vorm in vergelijking met gezonde controlepersonen, hetgeen een afspiegeling is van het beperkte instroomgebied bij patiënten.

In **Hoofdstuk 4** wordt de invloed van de afwijkende 3D instroomvortexring parameters die bij patiënten werd gevonden (**Hoofdstuk 3**) op de fysiologie van het LV bestudeerd via de associatie met verschillende niveaus van viskeus energieverlies in het LV tijdens diastole. De Navier-Stokes energievergelijkingen worden gebruikt om het instantane 3D viskeuze energieverlies in het LV non-invasief te bestuderen middels het snelheidsveld dat uit 4D Flow MRI is afgeleid gedurende de diastole in de reeds bestudeerde populatie van dertig vrijwilligers en tweeëndertig patiënten (**Hoofdstuk 2 en 3**). De associatie tussen niveaus van viskeus energieverlies en de eerder afgeleide 3D vortexringparameters (de oriëntatie en 3D-positie) werd bestudeerd tijdens zowel de vroege en late diastolische vulling, evenals voor de gehele diastole. Normaalwaarden van viskeus energieverlies en 3D vortexparameters werden verkregen uit het 95% betrouwbaarheidsinterval dat bij de

gezonde vrijwilligers werd bepaald. Patiënten met vortexringparameters die buiten het normale bereik lagen, lieten een aanzienlijke verhoging van het viskeuze energieverlies zien in vergelijking met gezonde vrijwilligers. Het hoogste viskeuze energieverlies werd gevonden bij patiënten waarbij de (goed ontwikkelde) E-vortex ring afwezig was, en bij patiënten met een omgekeerde oriëntatie van de E-vortexring (bij deze patiënten werd gemiddeld meer dan het dubbele viskeuze energieverlies gemeten dan in de rest van de patiënten). Als zodanig was dit de eerste in-vivo studie op basis van 4D Flow MRI waarin bevestigd werd dat de normale 3D vortexringvorming een rol speelt in de minimalisering van viskeus energieverlies.

In **Hoofdstuk 5** wordt de systolische vortexstroming in het linker atrium (LA) onderzocht bij gezonde vrijwilligers en patiënten met een gecorrigeerde aangeboren atrioventriculair septum defect (AVSD) en met ontbrekende tot milde en matige regurgitatie van de linker atrioventriculaire klep (LAVV). Atriale vortexstroming werd geïdentificeerd met behulp stroomlijnvisualisatie en 3D vortexkernanalyse (met behulp van de Lambda2-methode) rond het moment van LV-systole. Achterwaartse *particle tracing* met deeltjes die ontspringen vanuit de geïdentificeerde 3D vortexkern werd gebruikt om de oorsprong van atriale vortexstroming te identificeren. Vervolgens werd de atriale vortexstroming onderverdeeld in vier componenten op basis van herkomst van de deeltjes: 1) stroming afkomstig van linker longader (LPV) 2) stroming afkomstig van rechts longader (RPV) 3) residuele atriale stroming of 4) een regurgiterende stroming afkomstig uit het LV. De resultaten tonen aan dat bij zowel gezonde vrijwilligers als patiënten de atriale vortexstroming overwegend afkomstig is van de LPV. Echter, patiënten vertoonden een significante afname van LPV vortexstroming en een aanzienlijke toename van residuele atriale vortexstroming. In vergelijking met een enkele atriaal recirculerend stromingsgebied zoals aangetroffen bij gezonde vrijwilligers vertoonden patiënten verstoorde atriale vortexstromingen met meerdere gebieden van recirculerende stromingsstructuren rond de regurgitatie jet en met tegengestelde circulatierichtingen.

In **Hoofdstuk 6** wordt een methode voorgesteld om een automatische extractie van iso-oppervlakten van 3D LV vortexringkernen (door middel van Lambda2 vortexkernen) te bewerkstelligen tijdens de piek E- en peak-A vullingsfasen uit 4D Flow MRI van het gehele hart. De voorgestelde methode is gebaseerd op het vastleggen van de intrinsieke globale vormkenmerken van de cardiale vortexring iso-oppervlakte door gebruik te maken van de Laplace-Beltrami (LB) spectrale vormsignatuur. De LB signatuur wordt gedefinieerd als de divergerende eigenwaarden sequentie van de Laplace-Beltrami

differentiaaloperator. Deze LB sequentie codeert de onderscheidende vormkenmerken die inherent zijn aan de vorm van interesse. In dit werk wordt een LB referentie signatuur van de LV vortexring iso-oppervlakte afgeleid van een trainingset van LV vortexring iso-oppervlakten van gezonde vrijwilligers. In de extractiefase wordt de getrainde referentiesignatuur gebruikt om onder coëxisterende vortexobjecten iteratief te zoeken naar het LV vortexring object (iso-oppervlakte). Het vortexring doelobject wordt gedefinieerd als de iso-oppervlakte die de beste LB-signatuur overeenkomst heeft met de getrainde referentiesignatuur. Deze methode is geëvalueerd in een dataset verkregen uit acht gezonde vrijwilligers waarbij de *leave-one-out* kruisvalidatie is gebruikt en waarbij een nauwkeurigheid van 84% is verkregen. Echter, een beperking van dit werk is dat verwacht wordt dat de invoer bestaat uit meerdere geïsoleerde iso-oppervlakte objecten, waaronder het te verkrijgen vortexring iso-oppervlakte doelobject. Dit vereist een voorafgaande definitie van de iso-waarde die een dergelijke goedgedefinieerde vortexring voortbrengt die geïsoleerd is van de andere aanwezige vortexobjecten. In dit werk werd de selectie van de iso-waarde empirisch bepaald door middel van handmatige interactie. Voor de bepaling van de geschikte iso-waarde is ervaring nodig en kan een langdurig en subjectief proces zijn.

Om de in **Hoofdstuk 6** genoemde beperkingen van de methode te overwinnen, wordt in **Hoofdstuk 7** een nieuwe methode voorgesteld om de automatische identificatie van de 3D vortexringkern iso-oppervlakte uit 4D Flow MRI stromingsveld zonder enige aannames over de iso-waardebepaling te bewerkstelligen. In feite stelt de voorgestelde werkwijze de gebruiker in staat om een gelijktijdige automatische identificatie te verkrijgen van zowel de best passende iso-waarde en het object dat overeenkomt met de vortexring iso-oppervlakte. Eerst wordt het 4D Flow MRI snelheidsveld omgezet in een vortexkern scalair veld door gebruik te maken van de uit de stromingsleer bekende Lambda2 methode. Ten tweede wordt een vortexvormsignatuur afgeleid uit een trainingset van gezonde proefpersonen door middel van vormdistributies: de waarschijnlijkheidsverdeling van paarsgewijze Euclidische afstanden rondom willekeurig bemonsterde punten op de vortexring iso-oppervlakte. Deze afgeleide vormverdeling wordt gebruikt als een referentiesignatuur die de vorm van de vortexring iso-oppervlakte definieert. Tenslotte wordt een hiërarchisch vectorkwantisatiealgoritme voorgesteld dat tegelijkertijd de best passende iso-waarde definieert en de iso-oppervlakte identificeert van de vortexring tussen de bestaande vortex iso-oppervlakten. De methode werd kwalitatief en kwantitatief in twee cohorten geëvalueerd: een cohort van vierentwintig gezonde vrijwilligers en een cohort van drieëntwintig patiënten met aangeboren hartziekte. De resultaten van de uitgevoerde

experimenten toonden een uitstekende prestatie aan en een goede overeenkomst met geblindeerd gegenereerde grondwaarheid evenals een generaliseerbaarheid van de methode wanneer deze toegepast wordt bij uitdagende abnormale vortexringen bij patiënten. Als zodanig is de voorgestelde methode een stap voorwaarts in de richting van een objectieve automatische 3D vortexringanalyse uit 4D Flow MRI in de klinische praktijk.

8.2. Discussie en Toekomstperspectief

De doelstellingen van dit proefschrift die opgesteld zijn in **Hoofdstuk 1**, zijn behaald. Toch kan dit proefschrift als basis dienen voor toekomstig werk. In dit proefschrift hebben we 3D vortexringvorming en de evolutie ervan tijdens de gehele diastole geïdentificeerd en kwalitatief gekarakteriseerd (**Hoofdstuk 2**). Echter, 3D vortexringkwantificatie (**Hoofdstuk 2, 3, 4**) en automatische identificatie (**Hoofdstuk 6, 7**) zijn hoofdzakelijk beperkt tot piek vroege en piek late vullingsfasen, welke worden beschouwd als de momenten rondom de volledige ontwikkeling van de vortexring. Zoals echter getoond in **Hoofdstuk 2**, 3D cardiale vortexstroming is een dynamisch proces dat de ontwikkeling, propagatie, interactie met kamerwand en het daaropvolgende verval bevat. Deze dynamiek werd niet volledig gekwantificeerd in dit proefschrift. Een mogelijk mechanisme van vortexstroming in cardiale (dys-)functie zal eerder duidelijk zijn in het vortex evolutieproces. Toekomstig werk zou gericht moeten zijn op het kwantificeren van deze evolutie en haar relatie tot de cardiale (dys-)functie.

De belangrijkste focus van dit proefschrift was de instromende vortexstromingen in het LV tijdens diastole en het LA tijdens systole. In principe zijn de vortexidentificatie- en energie evaluatiemethoden die in dit proefschrift zijn ontwikkeld (**Hoofdstuk 2, 4, 6, 7**) algemeen toepasbaar op de analyse met 4D Flow MRI van andere bloedstromingsgebieden in het cardiovasculaire systeem. Een voorbeeld hiervan is weergegeven in **Hoofdstuk 5**, waarbij 3D atriale vortexidentificatie succesvol werd uitgevoerd na toepassing van methodes en werkwijze die oorspronkelijk ontwikkeld waren voor LV vortexanalyse (**Hoofdstuk 2**). We zijn van plan om in de toekomst de 3D vortex- en energiemethodes die in dit proefschrift zijn ontwikkeld, te gebruiken om de analyse naar andere hartkamers uit te breiden (rechter ventrikel, rechter atrium), evenals naar de grote slagaders, zoals de aorta, en over de volledige hartcyclus. Een dergelijke uitgebreide analyse zou meer inzichten kunnen geven in de normale fysiologie van het hart en de mogelijke aansluiting of verandering bij cardiovasculaire patiënten.

Euleriaanse vortexkernanalyse met behulp van de Lambda2 methode uit de stromingsleer was de belangrijkste methode die in dit proefschrift werd gebruikt voor het extraheren en het identificeren van instantane 3D vortexkerngebieden uit 4D Flow MRI. Een beperking van instantane (Euleriaanse) vortexkernidentificatie methodes is dat in de praktijk een drempelwaarde (iso-waarde) moet worden bepaald (voornamelijk handmatig) om zinvolle vortexkerngebieden te kunnen identificeren. Het feit dat verschillende drempelwaarden kunnen resulteren in verschillende 3D vortexvolumes maakt het uitdagend om betrouwbare volumetrische metingen (bijvoorbeeld vortexvolume, totale sterkte of totale energie) af te kunnen leiden op basis van dergelijke vortexkernanalyse. Dit wordt meer duidelijk wanneer het invoer snelheidsveld kenmerkend ruisig is en een lage resolutie heeft zoals het geval is met 4D Flow MRI. Dit is de belangrijkste reden waarom volumetrische vortexmetingen grotendeels vermeden zijn in dit proefschrift.

Een oplossing voor het probleem van de drempelwaardeselectie werd benaderd in **Hoofdstuk 7**, door de automatische identificatie van een passende drempel (iso-waarde). Dit zou een stap voorwaarts kunnen zijn in de richting van een objectieve identificatie van vortexkernvolume. Er zijn nog steeds studies nodig om de nauwkeurigheid van een dergelijke methode voor vortexvolumekwantificatie te evalueren. Aan de andere kant kunnen Lagrangiaanse vortex identificatiemethoden, zoals *Lagrangian Coherent Structures* (LCS) de kwantificatie van het totale vortexringvolume gedurende een tijdsperiode mogelijk maken, maar deze zijn over het algemeen niet bedoeld voor instantane vortexstromingsanalyse (dus kunnen er geen vortexvolumes worden gekwantificeerd op specifieke tijdstippen). Daarom zijn deze niet direct gericht op het analyseren van de evolutie van de instantane vortexstroming. In de toekomst moeten verschillende vortexidentificatiemethoden, waaronder Euleriaanse en Lagrangiaanse, worden onderzocht op een manier die nauwkeurige en objectieve analyse van de evolutie van de instantane 3D vortexstromingsvolumes mogelijk maakt.

4D Flow MRI is een *state-of-the-art* beeldvormende techniek voor in-vivo stroming en het is de enige modaliteit die toestaat om in-vivo 4D Flow data van alle drie de snelheidscomponenten te verkrijgen. Niettemin, 4D Flow MRI heeft een aantal beperkingen. Typerend zijn de lange opnametijden (tot 20 minuten) welke de klinische haalbaarheid beperken. Echter, de toepassing van recente versnellingstechnieken stelt de gebruiker in staat om een meer haalbare opnameduur te verkrijgen (~ 10 minuten als er geen respiratoire gating wordt toegepast) en dit zal naar verwachting in de toekomst nog verder verbeteren. Gezien de langzame MR opname is het voor 4D Flow MRI vereist om

over meerdere hartcycli data op te nemen. Dit resulteert in het voornamelijk verkrijgen van een gemiddeld stromingsveld, waarbij turbulente fluctuaties of in potentie hogere orde stromingscomponenten zijn gladgestreken. Dit moet in overweging worden genomen bij de berekening en / of interpretatie van 4D Flow MRI metingen met inbegrip van vortexstroming en energetica. De noodzaak om een passende gevoeligheid van de snelheids codering (VENC) voorafgaand aan de 4D Flow MRI opname heuristisch te bepalen om zo mogelijke omvouwingartefacten te vermijden, kan uitdagend zijn. Het verkregen 4D Flow MRI stromingsveld kunnen fouten bevatten in de vorm van inductiestromingseffecten in de spoelen, Maxwelltermen, signaalruis en / of offsetsnelheden. Deze fouten moeten worden gecorrigeerd met behulp van geschikte technieken voorafgaand aan de verwerking / interpretatie van stromingsdata. Lage temporele ($\sim 30\text{-}50$ ms) en spatiële resoluties ($\sim 3 \times 3 \times 3$ mm³) van 4D Flow MRI begrenzen stromingsanalyse tot de grootschalige stromingsstructuren met een levensduur die langer is dan de verworven temporele resolutie. Al deze factoren kunnen de betrouwbaarheid van 4D Flow MRI-gebaseerde resultaten en daaropvolgende interpretaties beperken.

Om een betrouwbare en correcte interpretatie van 4D Flow MRI metingen mogelijk te maken, is het belangrijk om deze resultaten te evalueren en valideren. Een beperkende factor in dergelijke validatie is het ontbreken van een realistische gouden standaard (grondwaarheid) van de in-vivo humane cardiovasculaire stroming in het algemeen, en vortexstroming en energetica in het bijzonder. Beschikbare fantoomtechnieken zijn niet in staat om een dergelijke realistische gouden standaard te leveren. Een manier om dit probleem in toekomstige studies aan te pakken zou kunnen zijn om te profiteren van de vooruitgang in *computational fluid dynamics* (CFD), door hybride CFD-4D Flow MRI computationele systemen te bouwen die realistische in-vivo stromingsveldmetingen (niet enkel de geometrie) opleggen uit 4D Flow MRI, om een hoge resolutie, beter controleerbare en robuuste CFD simulaties te begeleiden naar een realistisch hoge resolutie model van het menselijk cardiaal stromingsgebied.

Hoewel veel studies hebben gespeculeerd over een rol die vortexstromingsformatie speelt in de optimalisatie van de hartfunctie en / of de verbinding die het heeft met hartafwijkingen, ontbreekt het aan studies waarin dergelijke aannames in-vivo worden geëvalueerd in een juist en volledig stromingsveld. Met behulp van 4D Flow MRI stromingsvelden hebben we in **Hoofdstuk 4** de eerder gespeculeerde maar niet-geverifieerde rol van vortexstroming op de minimalisatie van energieverlies in-vivo

geëvalueerd en bevestigd. Meer (vervolg-)studies van verschillende groepen hartpatiënten zijn er nodig om het verband tussen vortexstromingspatronen en cardiale (dys-)functie te verkrijgen en om te bepalen of vortexstroming als biomarker kan dienen of dat het slechts een bijproduct is van andere factoren. In feite is de normale cardiale hemodynamica grotendeels onontdekt en daarom nog grotendeels onbekend. Terwijl momenteel onderschat in de gemeenschap, is het essentieel om meer studies uit te voeren die gericht zijn op het onthullen, op een alomvattend niveau, van de normale hemodynamica van het cardiovasculaire systeem voordat evaluaties in patiënten kunnen worden gestart.

Dit proefschrift toont de mogelijkheden aan van 3D/4D vortexstromingsanalyse en viskeuze energieverliesmetingen uit 4D Flow MRI in het onthullen en evalueren van in-vivo intra-cardiale hemodynamiek. Het is cruciaal om de betrouwbaarheid en reproduceerbaarheid van zulke metingen en analyses te garanderen om zo duidelijke klinische interpretaties mogelijk te maken. Een hoogwaardige vortexstromingsanalyse moet toegankelijk zijn voor klinisch personeel met minimale noodzaak voor technische achtergrond. Een belangrijk mechanisme om dit te bereiken zou zijn het blijven ontwikkelen van automatische betrouwbare systemen voor de identificatie en kwantificatie van cardiale hemodynamica in het algemeen en vortexstroming en energetica in het bijzonder uit 4D Flow MRI.

List of publications

Peer-reviewed Journal papers

1. **Mohammed SM Elbaz**, Rob J van der Geest, Emmeline E Calkoen, Albert de Roos, Boudewijn PF Lelieveldt, Arno AW Roest, Jos JM Westenberg: Assessment of viscous energy loss and the association with 3D vortex ring formation in left ventricular inflow: in vivo evaluation using 4DFlow. *Journal of Magnetic Resonance in Medicine* 2016. In press.
2. Calkoen, E. E.*, **Elbaz, M. S.***, Westenberg, J. J., Kroft, L. J., Hazekamp, M. G., Roest, A. A., & van der Geest, R. J. (2015). Altered Left Ventricular Vortex Ring Formation by 4DFlow MRI after repair of Atrioventricular Septal Defects. *The Journal of Thoracic and Cardiovascular Surgery*. (*Joint first-author)
3. **Mohammed SM Elbaz**, Emmeline E Calkoen, Jos JM Westenberg, Boudewijn PF Lelieveldt, Arno AW Roest, Rob J van der Geest: Vortex flow during early and late left ventricular filling in normal subjects: quantitative characterization using retrospectively-gated 4d flow cardiovascular magnetic resonance and 3 dimensional vortex core analysis. *Journal of Cardiovascular Magnetic Resonance* 2014 16:78.
4. Calkoen, Emmeline; **Elbaz, Mohammed**; de Koning, Patrick; Jongbloed, Monique; Kroft, Lucia; van der Geest, Rob; Blom, Nico; de Roos, Albert; Roest, Arno; Westenberg, Jos: Abnormal left atrial flow patterns in patients after atrioventricular septal defect correction and regurgitation: evaluation with 4DFlow Magnetic Resonance Imaging and particle tracing. *Submitted*.

Peer-reviewed full-papers in conference proceedings

5. **Elbaz, M. S.**, Lelieveldt, B. P., & van der Geest, R. J. (2015). Hierarchical Shape Distributions for Automatic Identification of 3D Diastolic Vortex Rings from 4D Flow MRI. In *Medical Image Computing and Computer-Assisted Intervention–MICCAI 2015* (pp. 467-475). Springer International Publishing.
6. **ElBaz, M. S.**, Lelieveldt, B. P., Westenberg, J. J., & van der Geest, R. J. (2014). Automatic extraction of the 3D left ventricular diastolic transmitral vortex ring from 3D whole-heart phase contrast MRI using Laplace-Beltrami signatures. In *MICCAI-Statistical Atlases and Computational Models of the Heart Imaging and Modelling Challenges* (pp. 204-211). Springer Berlin Heidelberg.
7. **ElBaz, M. S.**, & Fahmy, A. S. (2012). Active shape model with inter-profile modeling paradigm for cardiac right ventricle segmentation. In *Medical Image Computing and Computer-Assisted Intervention–MICCAI 2012* (pp. 691-698). Springer Berlin Heidelberg.

Peer-reviewed abstracts/presentations in CMR conferences

8. Vivian P Kamphuis, Arno AW Roest, Lucia JM Kroft, Rob J van der Geest, Albert de Roos, Nico A Blom, Jos JM Westenberg, **Mohammed SM Elbaz**: Noninvasive assessment of intracardiac viscous energy loss in Fontan patients from 4D Flow CMR, Annual meeting of European Cardiovascular MR (EuroCMR) society, 12-14 May 2016, Florence, Italy (*Poster Presentation*)
9. Vivian P Kamphuis, **Mohammed SM Elbaz**, Lucia JM Kroft, Rob J van der Geest, Albert de Roos, Nico A Blom, Jos JM Westenberg, Arno AW Roest: Three-dimensional vortex formation in patients with a Fontan circulation, Annual meeting of European Cardiovascular MR (EuroCMR) society, 12-14 May 2016, Florence, Italy (*Oral Presentation*)
10. **ElBaz, M. S.M.**, Töger J., Heiberg E., Westenberg J.J.: In-vitro comparison of segmented-gradient-echo versus non-segmented echo planar imaging 4D Flow CMR: validation of flow volume and 3D vortex ring assessment, Annual meeting of European Cardiovascular MR (EuroCMR) society, 12-14 May 2016, Florence, Italy (*Poster Presentation*)
11. **ElBaz, M. S.M.**, Arno A.W. Roest, Emmeline E. Calkoen, Boudewijn P.F. Lelieveldt1, P. J.H. de Koning , Rob J. van der Geest, Jos J.M. Westenberg: Apical inflow is associated with increased energy loss during left ventricular diastole in patients with a repaired atrioventricular septal defect: A 4D flow MRI study. *Journal of Cardiovascular Magnetic Resonance*, 18 (Suppl 1). (*Poster presentation at the conference of the society of cardiovascular MR (SCMR) 2016, Los Angeles, CA, USA*)
12. **ElBaz, M. S.M.**, de Koning, P. J.H, Westenberg, J. J., Calkoen, E., Lelieveldt, B. P., Roest, A., & van der Geest, R. J. (2015) Contribution of early and late filling vortex rings to normal left ventricular flow: Quantitative 4D Flow MRI analysis using 3D vortex cores combined with particle tracing. *International Society for Magnetic Resonance in Medicine (ISMRM)*, Toronto, Ontario, Canada (*Magna Cum Laude Merit Award: Oral presentation*)
13. **ElBaz, M. S.**, Calkoen, E., Westenberg, J. J., Roest, A., & van der Geest, R. J. (2015). Elevated energy loss in diastolic left ventricular inflow corresponds to an increase in kinetic energy in patients with a repaired atrioventricular septal defect: Quantification from 4D Flow MRI. *Journal of Cardiovascular Magnetic Resonance*, 17(Suppl 1), O6. (*Oral presentation at the conference of the society of cardiovascular MR (SCMR) 2015, Nice, France*)
14. **ElBaz, M. S.**, Calkoen, E., Roest, A., Westenberg, J. J., & van der Geest, R. J. (2015). Disturbed diastolic left ventricular inflow vortex ring formation in patients with corrected atrioventricular septal defect: quantitative three-dimensional vortex core analysis from 4DFlow MRI. *Journal of Cardiovascular Magnetic Resonance*, 17(Suppl 1), O4. (*Oral presentation at the conference of the society of cardiovascular MR (SCMR) 2015, Nice, France*)

15. **EIBaz, M. S.**, Calkoen, E., Westenberg, J. J., Roest, A., & van der Geest, R. J. (2015). Impact of disturbed diastolic vortex formation on viscous energy loss in the left ventricle: Quantitative 4D Flow MRI analysis of healthy controls and repaired atrioventricular septal defect patients. *Journal of Cardiovascular Magnetic Resonance*, 17 (Suppl 1), P24. (*Poster presentation at the conference of the society of cardiovascular MR (SCMR) 2015, Nice, France*)
16. **M.S. EIBaz**, E. E. Calkoen, J.J.M. Westenberg, B.P.F. Lelieveldt , A. Roest and R.J. van der Geest. "Three dimensional right ventricular diastolic vortex rings: characterization and comparison with left ventricular diastolic vortex rings from 4D flow MRI." *Journal of Cardiovascular Magnetic Resonance* 16.Suppl 1 (2014): P42. (*Poster presentation at the conference of the society of cardiovascular MR (SCMR) 2014, New Orleans, LA, USA*)
17. **M.S. EIBaz**, J.J.M. Westenberg, P.J. vanden Boogaard, B.P.F. Lelieveldt and R.J. van der Geest. "Quantification of Diastolic Vortex Shape Deformation in Left Ventricular Filling Pattern from 4D Flow MRI", *Journal of Cardiovascular Magnetic Resonance* 15.Suppl 1 (2013): P79. (*Poster presentation at the conference of the society of cardiovascular MR (SCMR) 2013, San Francisco, CA, USA*)

Invited Lectures

- European Cardiovascular Magnetic Resonance (EuroCMR) 14th conference, Florence, Italy from May 12- 14, 2016: *Intracardiac blood flow with 4D flow CMR*.
- Oxford's 3rd 4D Flow MRI workshop, Oxford University, Oxford, UK- June 28-29, 2015: *3D Vortex ring formation in left ventricular blood flow - Is it associated with minimization of energy loss?*
- Ageing, Brain and Circulation Meeting, Geriatrics and Radiology Department, Leiden University Medical Center, Netherlands- 8th April 2016: *Four-dimensional (4D) cardiac hemodynamic characterization from 4D Flow MRI and potential connection to brain*
- Pediatric Cardiology Department, Leiden University Medical Center, Netherlands- 6th November 2014: *Vortex Formation Inside The Heart: 3D Characterization from 4D Flow MRI*

Acknowledgements

The success of a Ph.D. journey cannot be realized without the help and support of many surrounding caring people. I want to take this opportunity to thank those who contributed, helped and supported me throughout my journey.

First, I would like to thank my promoter Boudewijn Leilieveldt and co-promoter Rob van der Geest for their vision and for giving me the opportunity to be part of such an exciting Ph.D. project. I am grateful for Boudewijn for his support throughout my four-year Ph.D. project and for giving me the opportunity to attend multiple interesting international conferences. Rob, I consider myself lucky having had you as my daily Ph.D. supervisor. I thank you for sharing with me your rich expertise in cardiac MR image analysis, for your open door policy on discussions, for your active role and willingness to always adapt and reprogram MASS to add functionalities to help me answer my posed research questions, and for the freedom you gave me in developing new ideas and for your continued encouragement. I cannot thank Jos Westenberg enough for all his significant 4D Flow MRI developments, insightful discussions, Dutch summary and for believing in me and in my ideas even when it meant flying to Sweden in a very short notice to get a phantom and to have to scan it several times for all night long. Jos, thank you for being a role model in how we should never tolerate scientific ethics or integrity for whatever gain. Jos, it has been an honor and a pleasure working with you.

Many chapters of this thesis have been the result of a fruitful collaboration with the Pediatric Cardiology department in LUMC. I would like to thank Emmeline Calkoen for all her efforts in scanning patients, analyzing data and for her help in applying my technical work in a real clinical setup. Arno Roest, your passion for new technology has been always a motivation for me and a source of hope that our technical work will one day be utilized in clinical practice. Arno, thank you for all your interesting and exciting discussions and for driving our collaboration into success.

Of course, I cannot forget Patrick de Koning; all his developments in particle tracing visualization, his valuable discussions, and support that facilitated the development of many ideas. Patrick thank you for being always there to help with LAVA-Flow developments and integration of vortex assessment methods into it, for building the wood boxes over the weekend for our phantom shipment from Sweden and for accepting to be my paranymph.

Pieter van den Boogaard, to me you have been a great example of a true science passionate. I can never forget your help in MR acquisition and vortex phantom experiments that you were

always excited about, and passionately volunteering to help with, despite having to scan all night long until next morning. Pieter, thank you for all of your amazing support.

A great quality of the Division of Image Processing (LKEB) is the diversity in background of its members and in the conducted image analysis research applications. Whatever question you have about image analysis or programming you will find a knowledgeable colleague around willing to help. Ronald Van't Klooster, thank you for your assistance with MASS Dicom libraries and for helping me to integrate during my early days at LKEB. Thank you Artem Khmelinskii for providing me with the thesis' layouts and for our nice discussions. Shan Gao and Rahil Shahzad it was great having you as office mates over the past years. Rahil thank you for accepting to be my paranymph and for your help in designing the cover of this thesis. I would like to extend my gratitude to LKEB colleagues who were always there to help and discuss: Qian Tao, Oleh Dzyubachyk, Marius Staring, Vikas Gupta, Michèle Huijberts, Leo Wolf and all LKEB members.

In 2015, I had the opportunity of spending two months in Fotis Sotiropoulos' Saint Anthony Falls lab at the University of Minnesota in Minneapolis. Fotis, thank you for the great opportunity and for your amazing friendly and motivational attitude. During my stay, I met and interacted with some fantastic people. Thank you Trung Bao Le for your welcoming attitude throughout my stay and for all the exciting discussion we had on a daily basis on integrating fluid mechanics and intra-cardiac 4D Flow MRI. I would also like to thank Ali Khosronejad for all nice discussions and great lunch times. Thank you Dionysios Angelidis for the accompany during long working days and for introducing me to the multi-scale mesh refinement. I would like to thank Erik Kaaya for his tremendous kindness in helping me arranging my daily necessities in Minneapolis despite the fact that I was just a stranger who he just met for the very first time while waiting for the bus. Erik, it was really great getting to know you afterward and I really enjoyed our chats together.

There are no words that can express my gratitude to my parents who made me who I am today. Any success or good ethics that I have are no doubtfully the results of their teaching, caring, devotion and unmatched love over all the years of my life. Thank you for helping me to develop my love to science since my early childhood. My life would not be complete without the love of my sister Lamis and my brothers Ahmed and Mahmoud.

Finally, If there is a person that shared the stress, anxiety and hard times of my Ph.D., it is my beloved wife Simin. I cannot express how grateful I am for all your support, love and for bearing my usual long working hours and my stressful attitude. Simin, you are an amazingly smart, caring, understanding and supportive wife. I am so lucky to have you in my life.

Mohammed S.M. Elbaz Leiden, July 2016

Curriculum vitae

Mohammed S.M. Elbaz was born on 25th of August 1985 in Dakahliya, Egypt. In 2006, he received his BSc. Degree with excellence in Computer Science at Helwan University, Egypt, ranking 1st among 260 students in the final Bachelor's year and among top 5% cumulatively. His BSc. graduation project which entitled "Kidney Early rejection detection after Renal Transplantation (KERD) " won the 3rd place in the Global Idea to Product (I2P) competition which held at Texas university at Austin, USA by winning over Stanford university who ended in 4th place. From 2006 till 2011, he was working at the R&D department of Healthy-IT Company, Egypt as a senior medical image processing and visualization R&D engineer. In 2010, he received a two-year Fellowship from Nile University, Egypt to complete his MSc. Studies. Meanwhile, he joined the Medical Imaging and Image Processing (MIIP) lab of Nile University, Egypt as a research assistant in cardiac MR image analysis. In 2011, he received his MSc. degree from the School of Communication and Information Technology, Nile University, Egypt with a master thesis entitled "Right Ventricle Segmentation using Active Shape Model with Inter-Profile Modeling". In 2011, he worked for Diagnosoft Inc. (now Myocardial Solutions Inc.) as a senior 3D medical visualization developer. From January 2012 to December 2015, he worked on this thesis at the MRI section of the Division of Image Processing (LKEB), Department of Radiology at Leiden University Medical Center, Leiden, The Netherlands as a scientific researcher and a PhD candidate. During his PhD period, Mohammed spent two-month (July-September 2015) as a visiting researcher at the Saint Anthony Falls Laboratory (SAFL) of Minnesota University, USA under the direction of prof. Sotiropoulos where he worked with Sotiropoulos' team on integrating 4D Flow MRI and CFD simulations and concepts to allow better realistic intra-cardiac CFD simulations and derive hemodynamic-based biomarkers of cardiac function.

Since January 2016, Mohammed is a postdoctoral researcher on cardiovascular 4D Flow MRI image and hemodynamic analysis at the Division of Image Processing, Department of Radiology, Leiden University Medical Center, Leiden, The Netherlands.

ISBN 978-94-6332-052-8